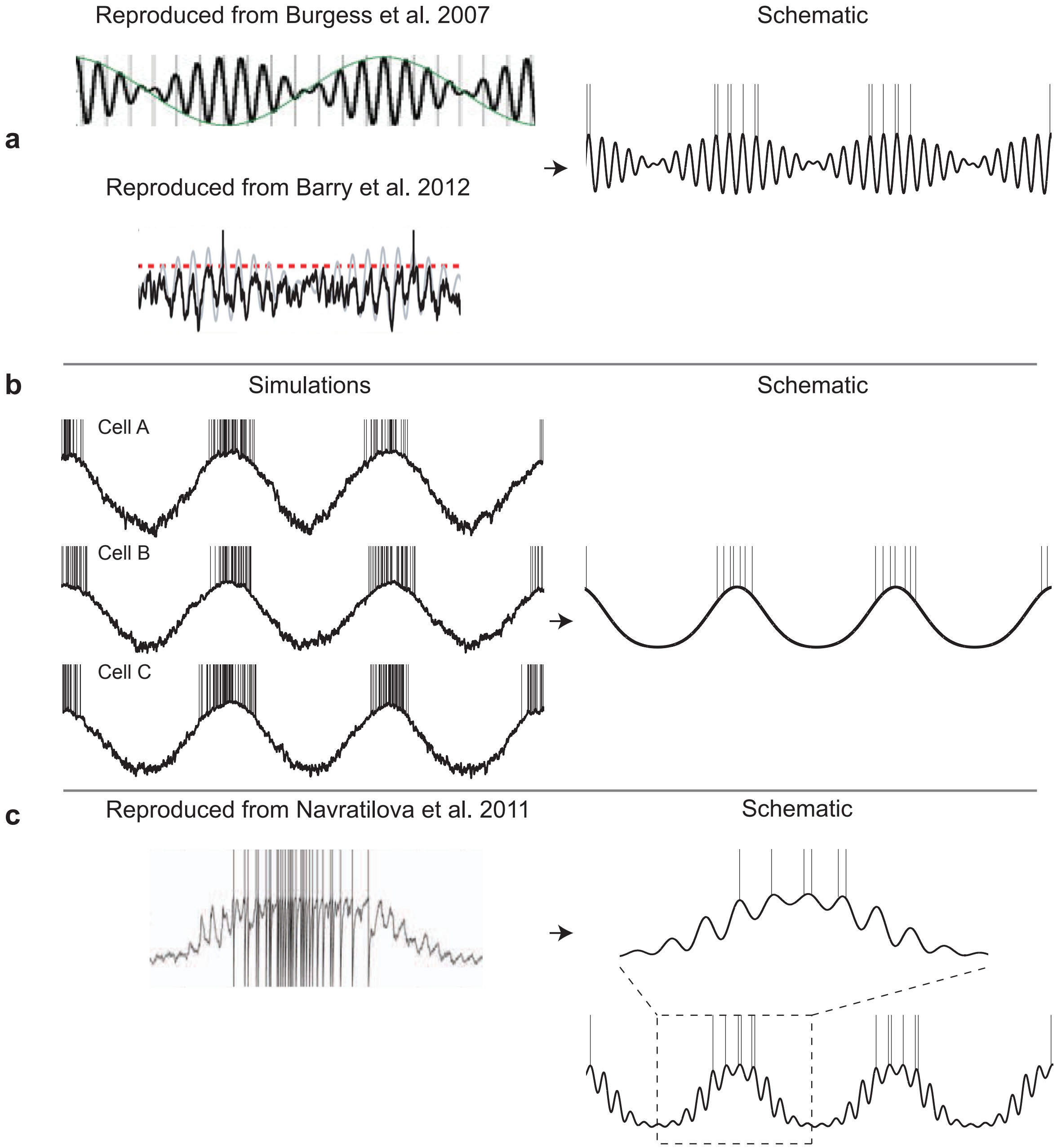

**Supplementary Figure 1 | Reference figures and simulations used to create predicted membrane potential schematics. a,** Left - top: figure reproduced from Burgess et al. 2007 (their Figure 1). Left - bottom: figure reproduced from Barry et al. 2012. Right: schematic. **b,** Left: simulations of the membrane potential and spikes of grid cells in a spiking attractor network model. Right: schematic of the attractor network model, with noise ommitted. **c,** Left: figure reproduced from Navratilova et. al. 2011 (their Figure 3F) illustrating the membrane potential of a grid cell during a field traversal. Right: schematic used to illustrate the representative features of this model, including ramps of depolarization and an increase in theta amplitude in grid fields.

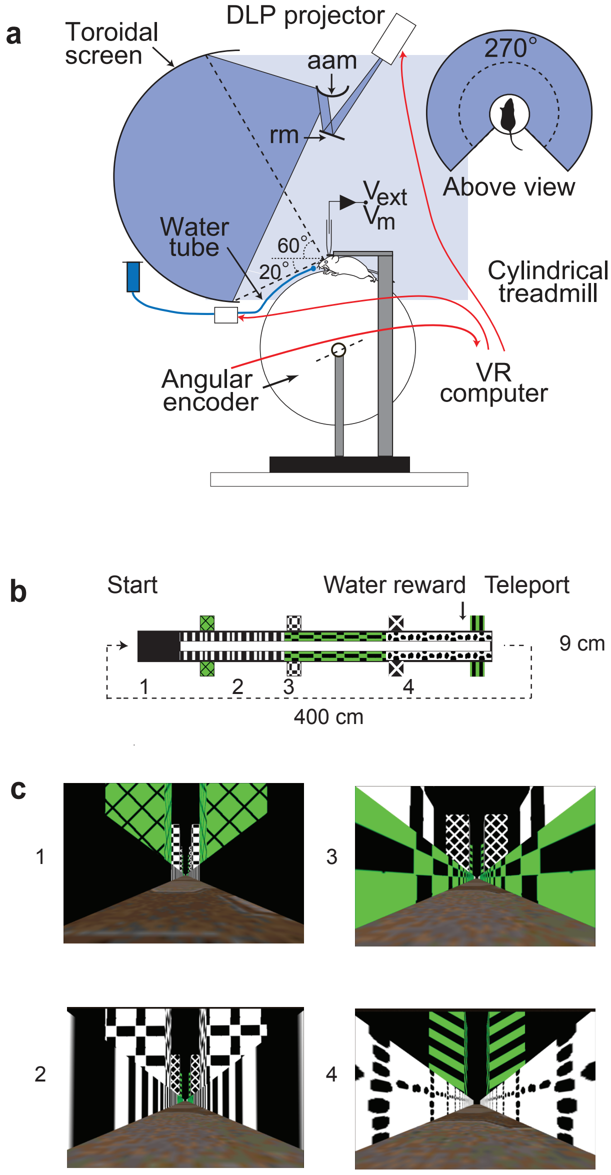

**Supplementary Figure 2 | Schematic of virtual reality setup and linear track design. a,** Schematic of the virtual reality setup. This setup differs from the spherical treadmill-based virtual reality system (Harvey et al. 2009) by using a cylindrical treadmill that allows movement only in one direction, without turning. The mouse runs forward on the treadmill, traversing a virtual linear track. **b,** Schematic of the 400 cm linear track used for whole cell recordings. All whole cell recordings were performed on this track, except for two, which were obtained on a similar but longer, 600 cm linear track (not shown here). The virtual environment was visually similar to one used previously for whole cell recordings from place cells (Harvey et al. 2009), and consisted of proximal and distal walls and columns. Both walls and columns had textures including black, white and green stripes and dots. In addition a low contrast floor texture was used. At the end of the track, the mouse approaches the black environment beyond the end of the track, then teleports back to the beginning; to increase visual continuity during the teleport, the walls at the beginning of the track are also black (position 1). To a human observer, this configuration of walls creates the appearance of a finite track that is traversed repeatedly, with a very short transition period between traversals where the environment is dark (rather than an infinite track with repeating wall textures). **c,** Screenshots (linear perspective) at four positions (1-4) along the virtual linear track. The four positions are indicated in (b).

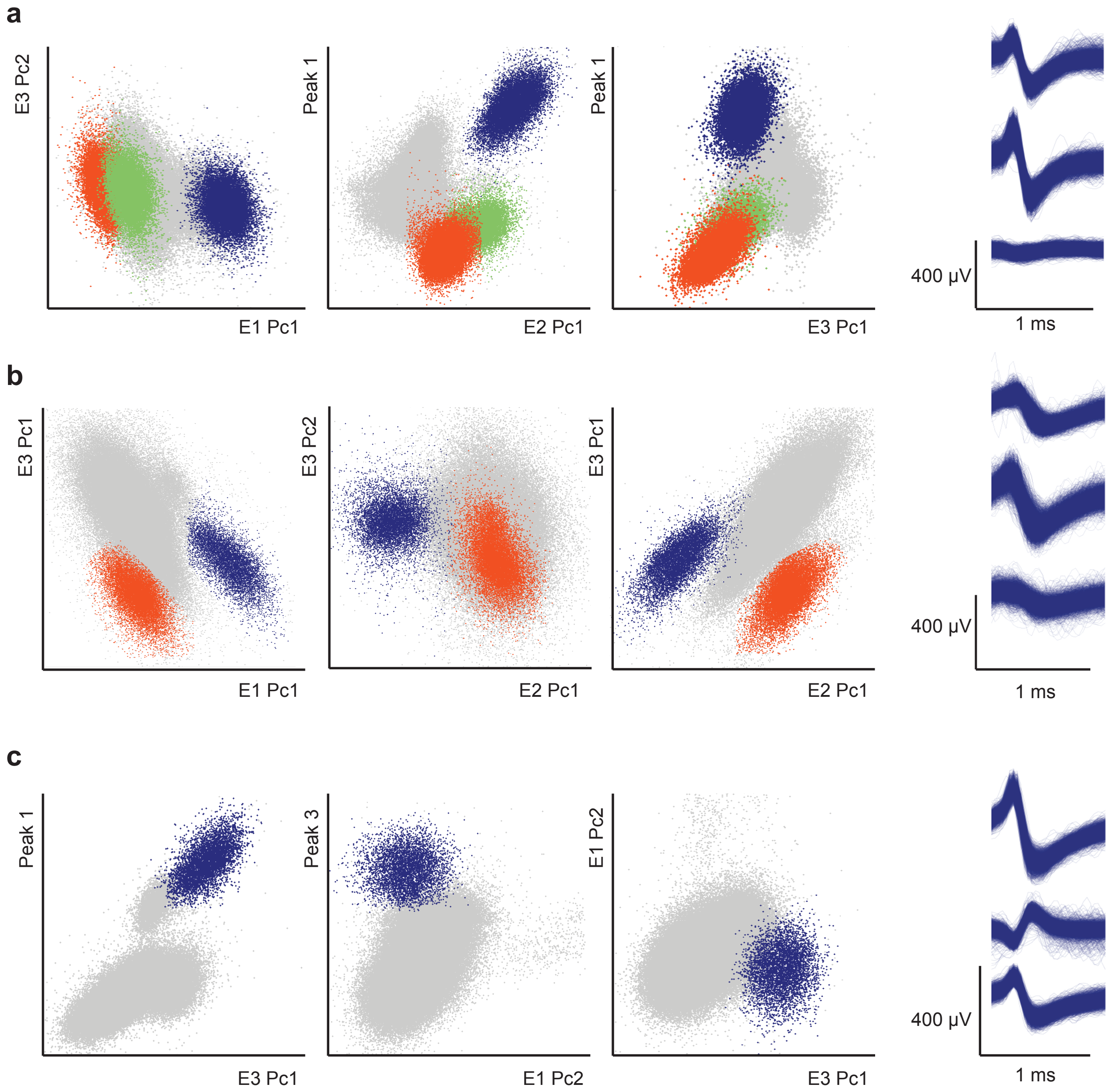

**Supplementary Figure 3 | Examples of spike sorting in mouse MEC. a-c**, Three example tetrodes. Clusters were cut manually using two-dimensional projections of the nine-dimensional space consisting of principal components 1 and 2 on each of 3 electrodes as well as the peak spike amplitude on each of 3 electrodes. The fourth electrode on each tetrode was used as a reference. Left: scatterplots showing the relationship between principal components of the spike waveform or between peak amplitudes on different electrodes. Axes are labeled either with electrode and principal component numbers (e.g. E1 Pc1 indicates the first principal component on electrode 1) or with electrode and peak numbers (e.g. Peak 1 indicates the peak on electrode 1). Each dot corresponds to a single threshold-crossing event. Right: all waveforms of each of the three clusters shown in dark blue in a-c; waveforms on three electrodes are shown for each cluster. Each cluster is likely to correspond to a single unit. Cluster separation was estimated by calculating the isolation distance, a standard distance measure in Mahalanobis space that represents how well separated a cluster is from noise spikes outside the cluster (Schmitzer-Torbert, N. et al. Quantitative measures of cluster quality for use in extracellular recordings. Neurosci. 131, 1-11 (2005)). The median Mahalanobis distance was 21.2; the interquartile range was 14.2-29.6. These values are highly similar to isolation distances reported for MEC recordings in bats (Yartsev et al. 2011) and rats (Langston et al. 2010). All cells shown were grid cells.

# Tetrode recordings - identifying grid cells based on 2D firing

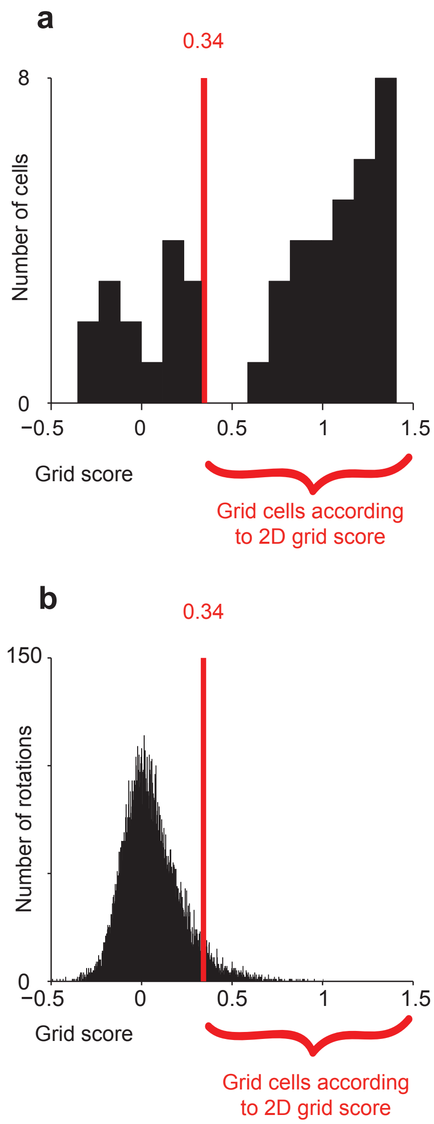

**Supplementary Figure 4 | Defining grid cells based on the 2D grid score**. **a,** Distribution of grid scores of 46 cells recorded with tetrodes. **b,** Baseline distribution of grid scores resulting from randomly rotating the spikes from the same cells shown in (a) with respect to the position signal (400 rotations from 46 cells, for a total of 18400 rotations). Red lines indicate the 95th percentile of the shuffled distribution of grid scores from (b), which defines the grid threshold (Gth = 0.34). All cells with grid scores greater than or equal to Gth are considered grid cells.

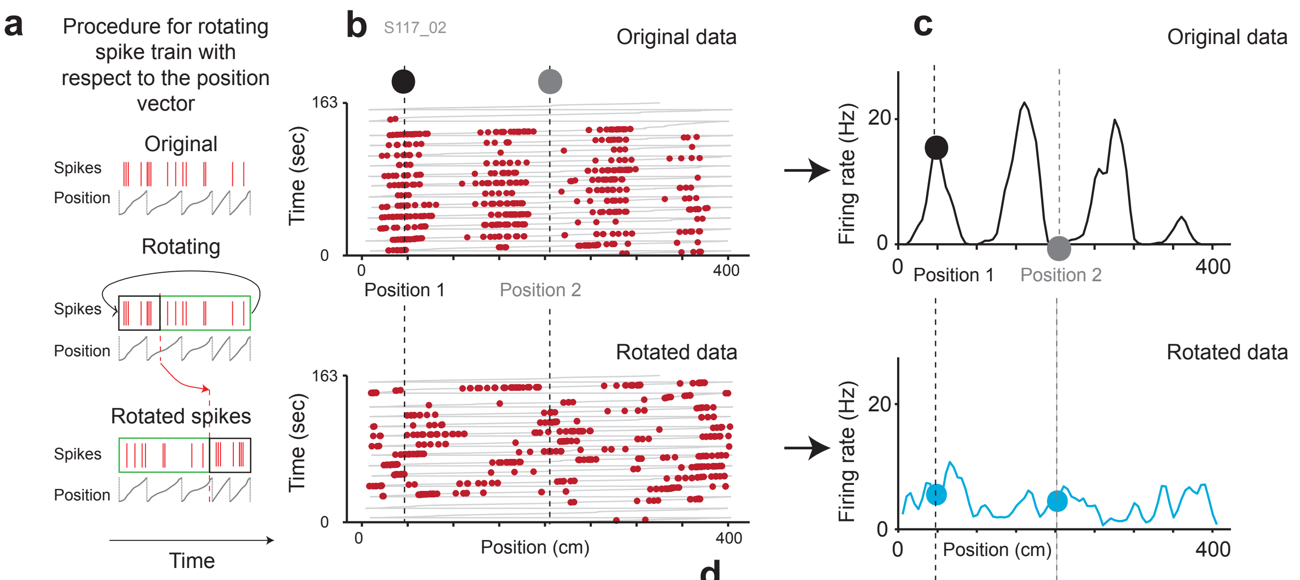

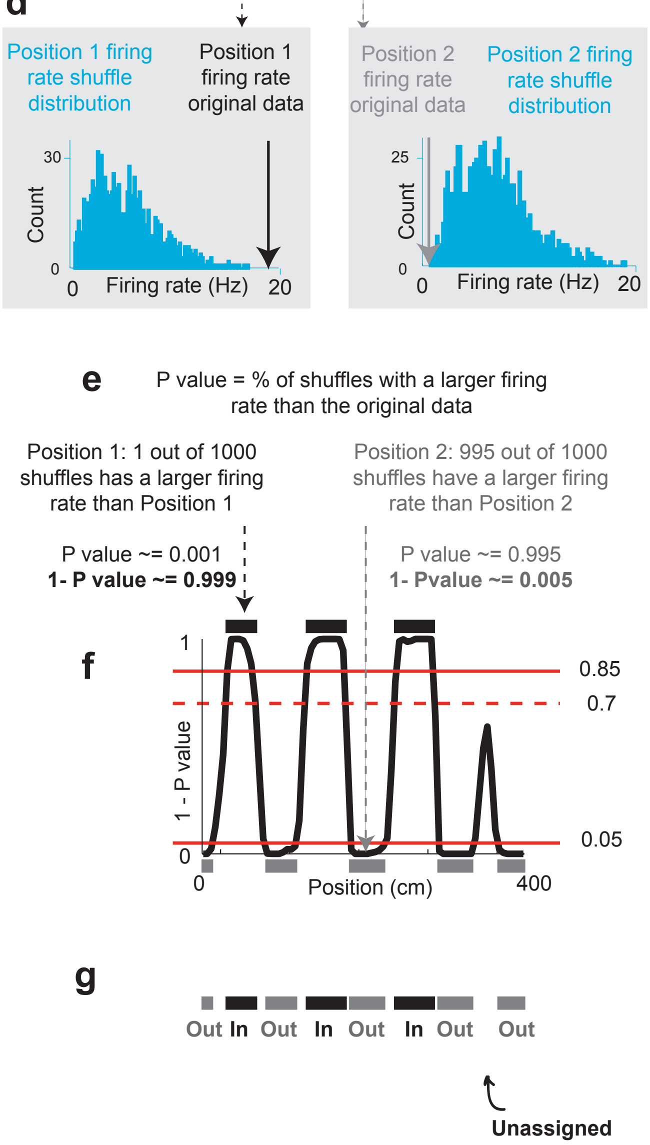

**Supplementary Figure 5 | Procedure for defining fields and out-of-field regions for one cell. a**, Schematic of spike rotation with respect to the position vector. **b**, Mouse position and spikes (grey lines and red dots) for the original data (top) and one example of rotated data (bottom). **c,** Firing rate along the linear track for the original data (top, black) and the rotated example from b (bottom, blue) measured in 5 cm bins along the linear track. Note that the firing rate at position 1 (black) is high, and no spikes are fired at position 2 (grey) in the original data (top), whereas the firing rates at these two positions for the rotated data from (b) are more similar (blue dots). **d**, (left) Baseline distribution of firing rates at Position 1 obtained from 1000 rotations (blue histogram). The black arrow points to the firing rate of the original data at Position 1. Note that almost all the rotated firing rates were lower than that of the original data at Position 1 because this position corresponds with a peak in the firing rate shown in (c). (right) Same plots for Position 2. Note that, for position 2, almost all the rotated firing rates were higher than that of the original data because the cell did not spike at position 2 (b). **e**, The P value associated with each position is calculated; the procedure is described for both positions 1 and 2. **f**, 1-P value function for every position in this cell. Note the resemblance between this function and the firing rate (c, top). In-field periods (black) and out-of-field periods (grey) are defined based on the 1-P value for each position. The three red lines indicate three thresholds used in this definition (Methods). Briefly, candidate fields were identified as regions where the 1-P value function was above the top, solid red line (>= 0.85) and extended by no more than one bin in either direction so long as the 1-P value remained above the dashed red line (>= 0.7). Out-of-field periods were defined as three or more contiguous bins below the lower red line (1-P value <= 0.05). Note that Position 1 has a very high 1-P value and is inside a field, while Position 2 has a very low 1-P value and is in an out-of-field period. **g**, Same in-field ('In') and out-of-field ('Out') periods from (f). Note that a subset of positions with intermediate P values remain unassigned.

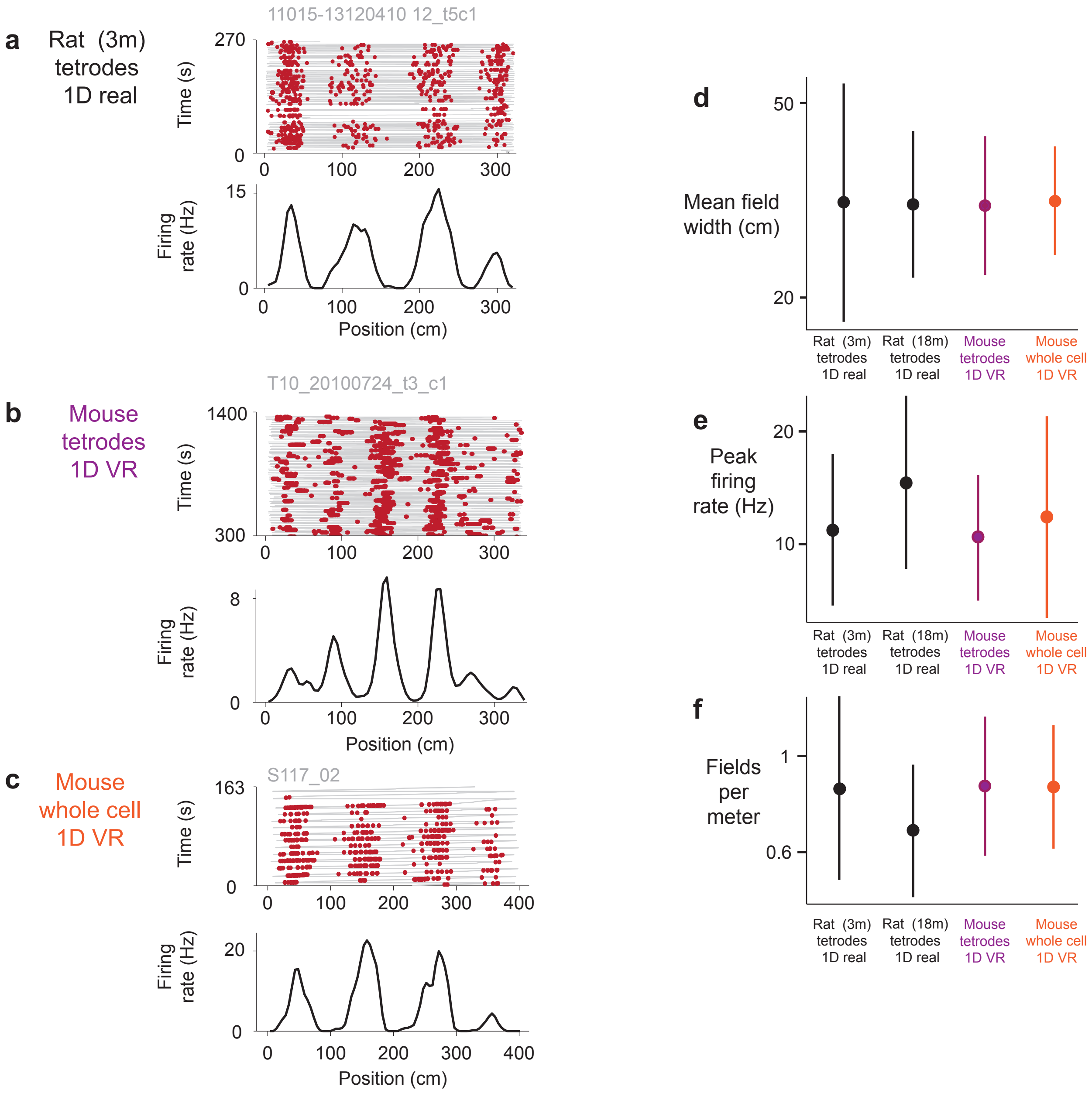

**Supplementary Figure 6 | Mouse grid cells in virtual linear tracks and rat grid cells in real linear tracks have quantitatively similar properties**. **a,** Grid cell (identified from tetrode recordings in a 2D arena) recorded with tetrodes in a rat running along a real linear track (data obtained from Hafting et al. 2008). Top: trajectory (grey lines) and spikes (red dots) on stacked successive runs along the linear track. Bottom: firing rate at each position along the linear track. **b,** Grid cell (identified from tetrode recordings in a 2D arena) recorded with tetrodes in a mouse running along a linear track in virtual reality. **c,** Grid cell (identified by the 1D classifier) recorded in the whole cell configuration in a mouse running along a linear track in virtual reality. Note the resemblance between the spatial firing properties of grid cells in these three configurations. **d-f**, Comparisons of mean field width, peak firing rate, and fields per meter for grid cells recorded with tetrodes in rats running along a 3 m linear track (Hafting et. al. 2008, black - left, n = 33, forward and backward runs considered separately), rats running along an 18 m linear track (Brun et al. 2008, black - right, n = 197, forward and backward runs considered separately), mice running along a virtual linear track (purple, n = 31), and cells recorded in the whole cell configuration in mice running along a virtual linear track (orange, n = 27). Dots represent the mean, lines represent ± std.

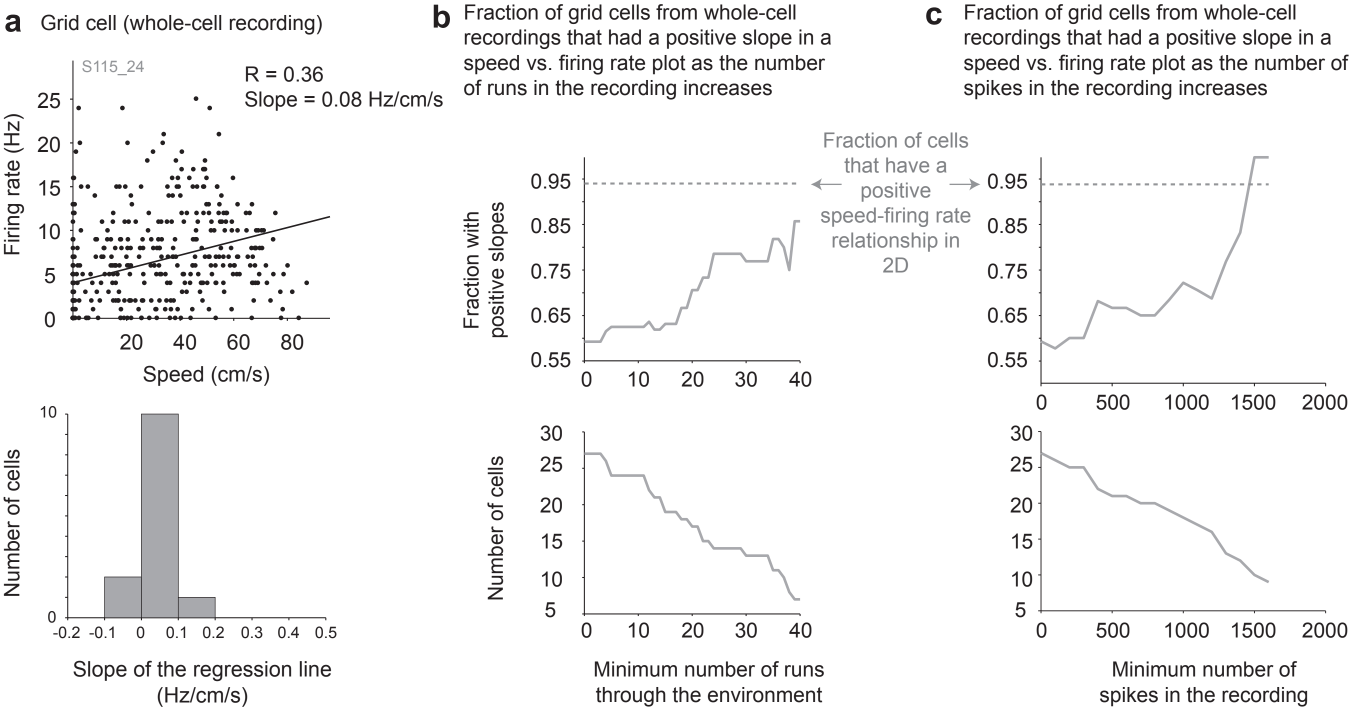

**d**

| 2D or 1D | Fraction of cells that had a positive speed-firing rate relation | Cell count | Real or VR | Source of data | Selection method |
|---|---|---|---|---|---|
| 2D | 94% | 141/150 | Real | Sargolini et al. 2006 | All grid cells |
| | 94% | 93/99 | Real | Fyhn et al. 2008 | All cells |
| 1D | 79% | 44/56 | Real | Brun et al. 2008 | Grid cells with more spikes than the median obtained with whole-cell recordings |
| | 83% | 10/12 | Real | Hafting et al. 2008 | |
| | 87% | 26/30 | VR | Tetrode recordings | |
| | 85% | 11/13 | VR | Whole-cell recordings | |
| | 78% | 76/98 | Real | Brun et al. 2008 | All grid cells |
| | 88% | 14/16 | Real | Hafting et al. 2008 | |
| | 87% | 27/31 | VR | Tetrode recordings | |
| | 67% | 18/27 | VR | Whole-cell recordings | |

**Supplementary Figure 7 | On linear tracks, the majority of grid cells have a positive relation between running speed and firing rate. a,** Top, example relation between running speed and firing rate (Methods) in a representative grid cell recorded in the whole-cell configuration. Bottom, frequency distribution of the slope of the regression line between firing rate and running speed for grid cells recorded whole-cell where the recording included an above-median number of spikes. **b,** The fraction of grid cells (whole-cell) that have a positive speed-rate relation increases as the minimum number of runs through the environment required for inclusion in the analysis increases. Approximately 80% of cells for which thirty or more runs were recorded have a positive speed-rate relation. **c,** The fraction of grid cells (whole-cell) that have a positive speed-rate relation increases as the minimum number of spikes required for inclusion in the analysis increases. Because of this dependence on number of runs or number of spikes, and because tetrode datasets generally contained more spikes than whole-cell recordings, to compare the fraction of cells with positive speed - firing rate relations between the datasets we only considered recordings containing more spikes than the median number of spikes in the whole-cell data set (Methods). **d,** Table comparing the fraction of cells that have a positive speed-rate relation in 2D (as previously reported) and in 1D, analyzed here. The fraction of cells that have a positive speed-firing rate relation was ~94% in real 2D environments. In 1D environments, when averaged across datasets, ~83% of grid cells had a positive speed-firing rate relation (~79% in Brun et al. 2008, ~83% in Hafting et al. 2008, 87% in VR tetrode recordings and 85% in VR whole-cell recordings). When all cells were considered regardless of the number of runs or number of spikes, these values remained unchanged for the tetrode datasets but decreased to 67% for whole-cell recordings. This difference was likely due to the fact that most whole-cell recordings with below-median numbers of spikes had many fewer spikes than the tetrode recordings with below-median numbers of spikes.

**Supplementary Figure 8 | The 1D classifier identifies grid cells with a high success rate and a low false positive rate.** Grid scores of all cells recorded with tetrodes in both real 2D arenas and a virtual 1D track that were identified as grid cells by the 1D classifier (grey ticks); the grey distribution is shown as a visualization of the grid scores, and was obtained by placing a gaussian kernel centered on each cell's grid score (one gaussian kernel per tick) and summing them - this is a kernel based estimate of the distribution of grid scores; the red line indicates Gth, the cutoff used for classifying cells as grid or non-grid cells based on their 2D firing, as shown in Fig. S4. Cells to the right of the red line ('True positives', 87%) are grid cells according to the 2D classifier and were correctly identified by the 1D classifier. Note that the majority of cells labeled as grid cells by the 1D classifier fall to the right of the red line. Cells to the left of the red line ('False positives', 13%) are incorrectly identified as grid cells by the 1D classifier.

**True positives, part 1 (grid cells according to the 2D gridness score that were correctly identified by the 1D classifier):**

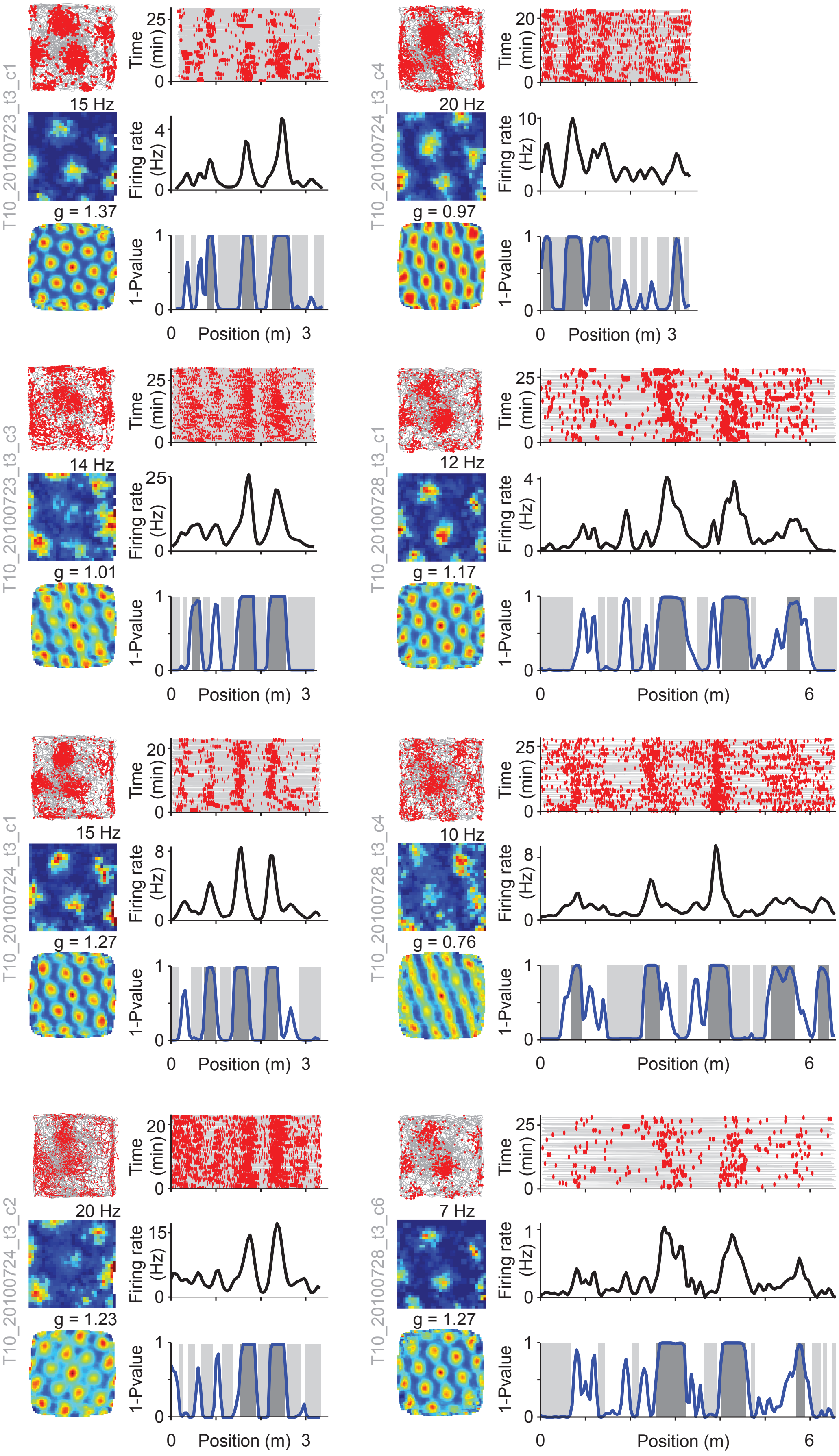

**Supplementary Figure 9 - part 1 | All tetrode recordings in 2D and 1D**

**True positives, part 2 :**

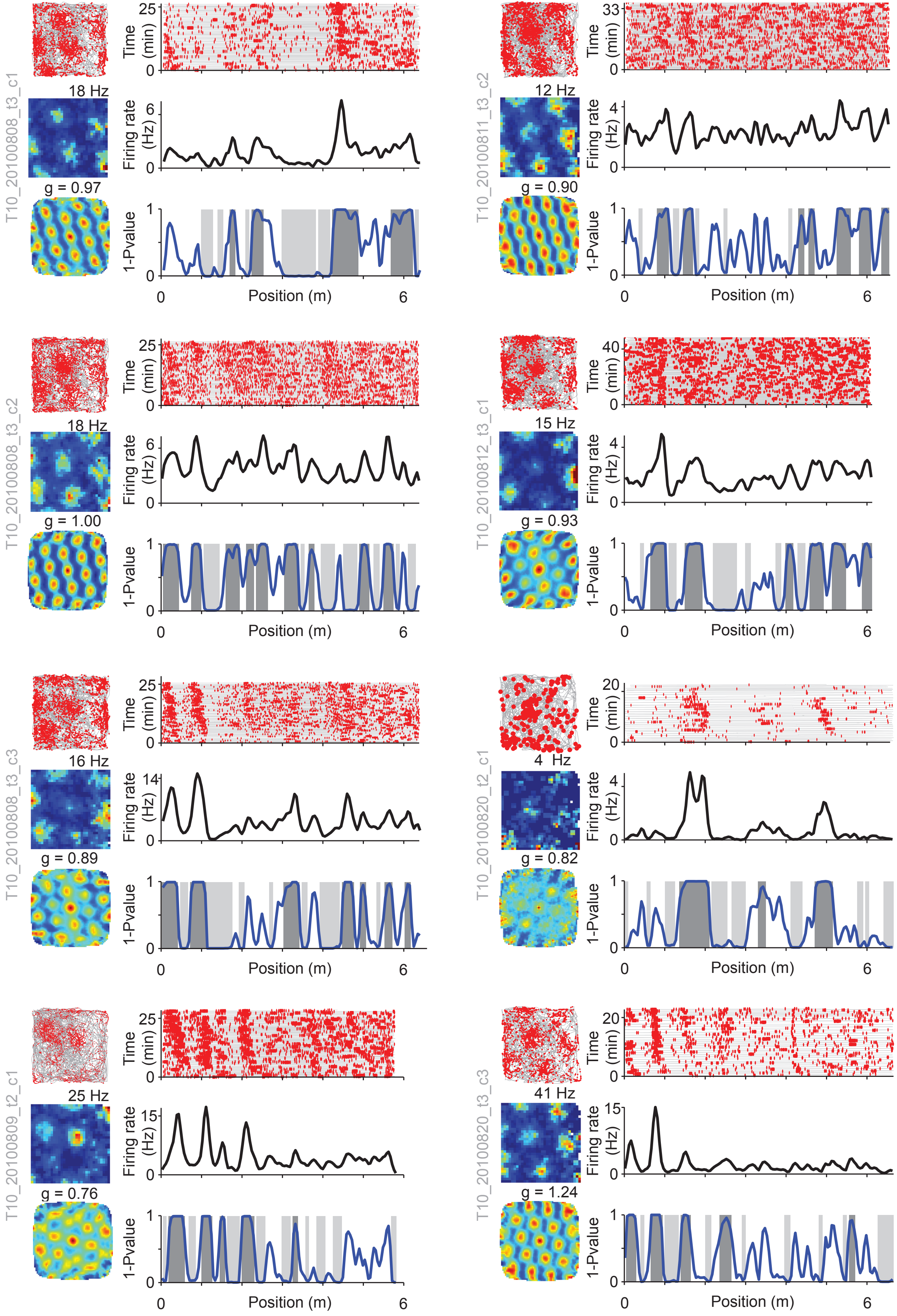

**Supplementary Figure 9 - part 2 | All tetrode recordings in 2D and 1D**

**True positives, part 3 :**

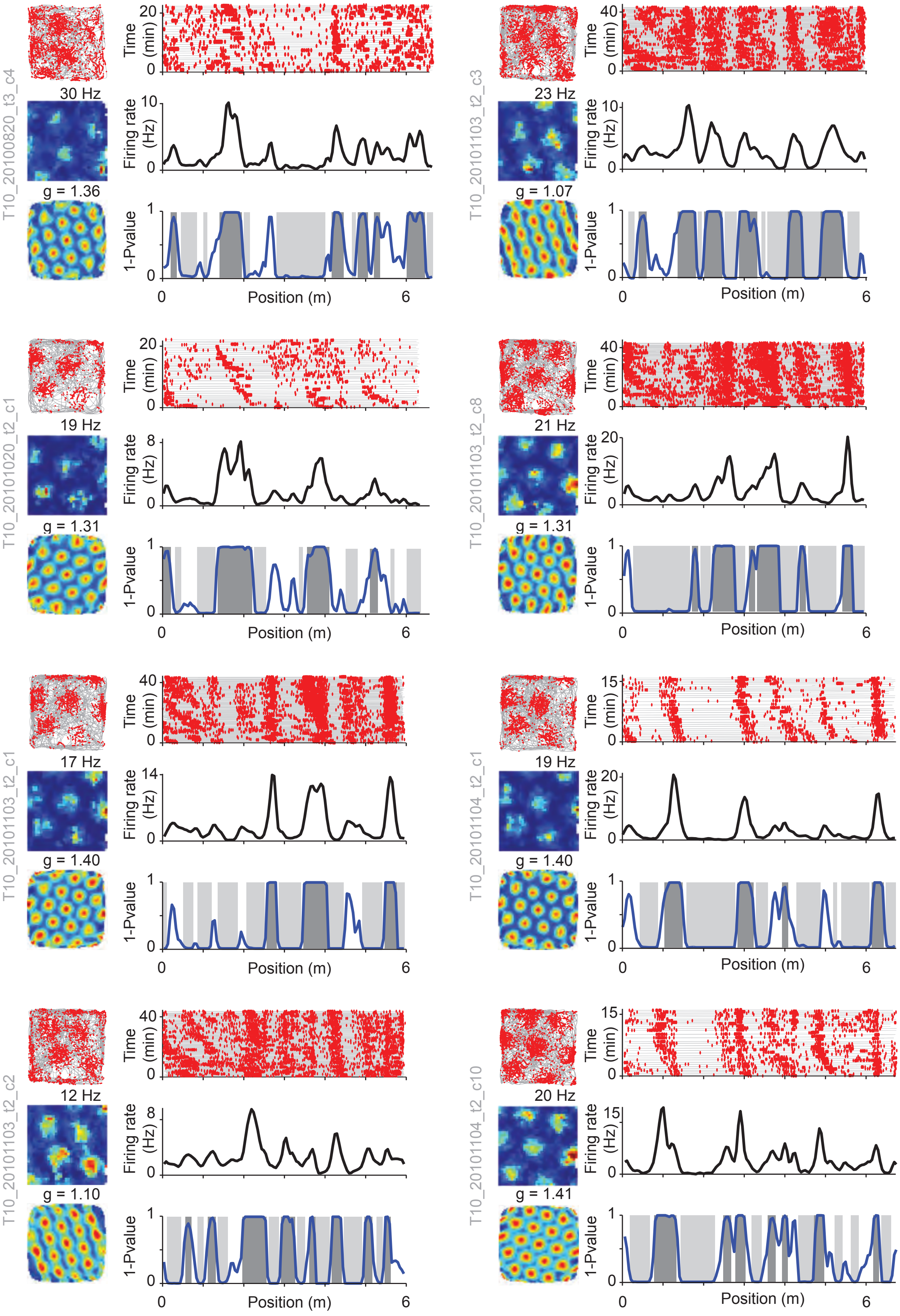

**Supplementary Figure 9 - part 3 | All tetrode recordings in 2D and 1D**

**True positives, part 4 :**

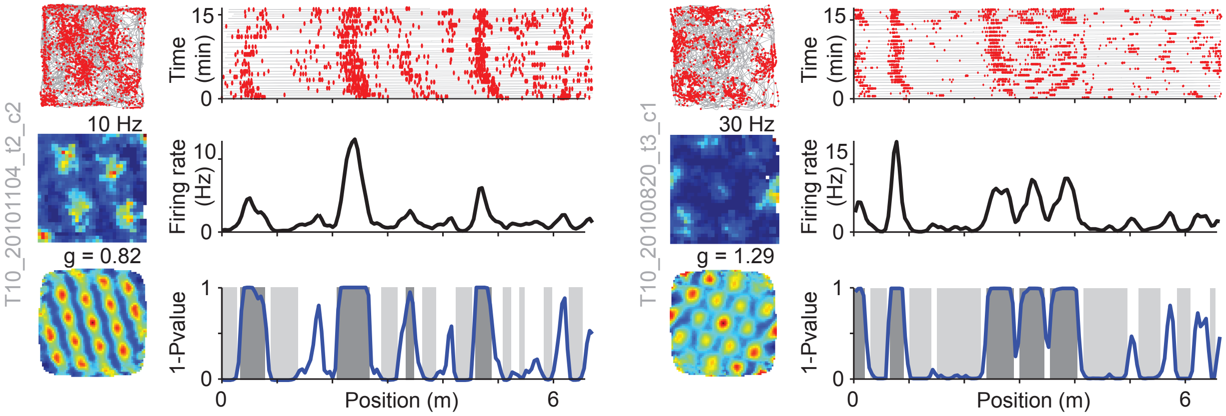

**Above: the 26 grid cells correctly identified by the 1D classifier.** For each cell: Left, top, spikes (red dots) and trajectory (grey trace) in a 0.5 x 0.5 m real environment; middle, firing rate in the 2D environment (peak firing rate above); bottom, autocorrelation of the firing rate (grid score above). Right, top, spikes (red dots) and trajectory (grey trace) during multiple runs through the virtual 1D environment (shown stacked); middle, firing rate along the linear track; bottom, 1-Pvalue function (dark blue) along the track (firing fields are indicated with dark grey boxes and out-of-field periods with light grey boxes; a fraction of the track is not assigned to either an in-field or an out-of-field period). The virtual linear tracks used varied in length from ~3 to ~8m.

**False positives:**

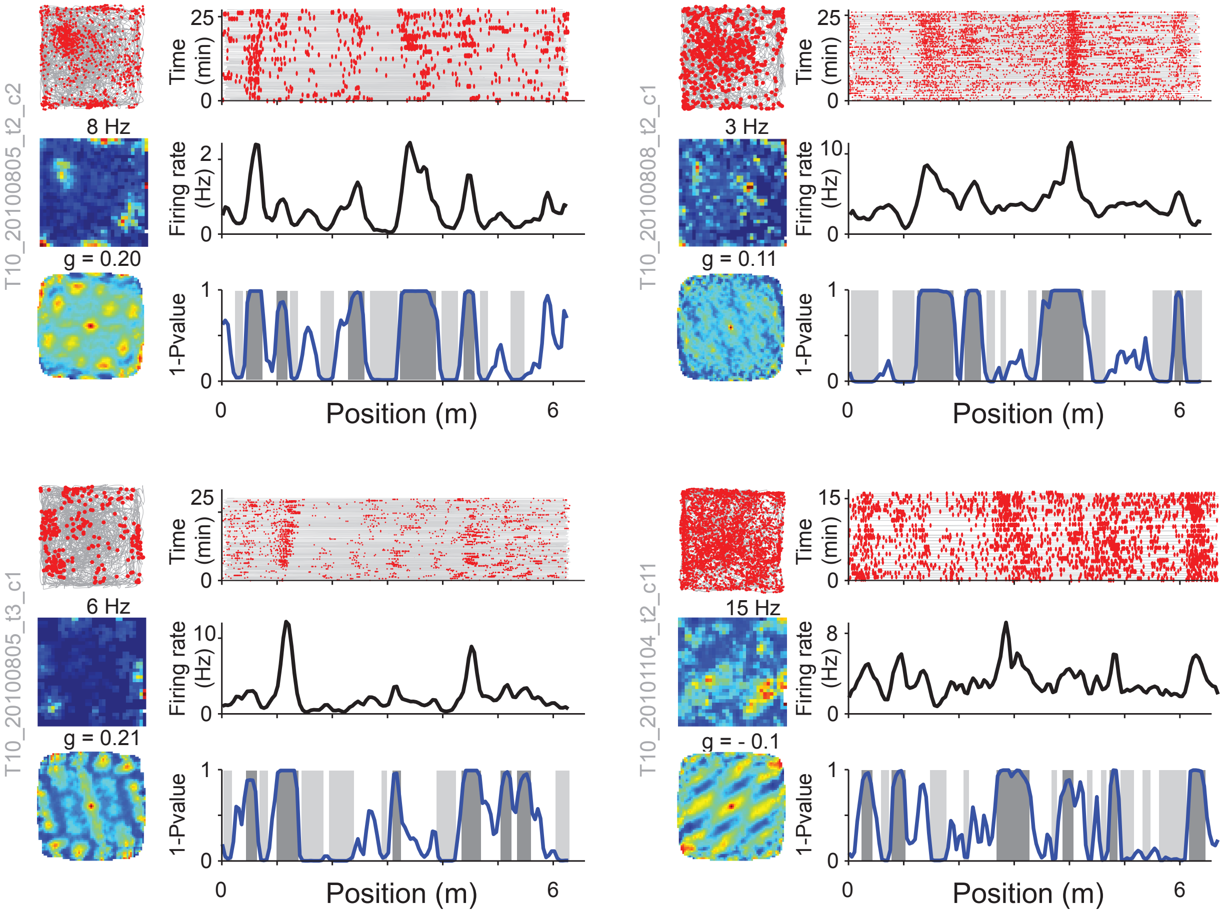

**Above: the 4 false positives.** False positives occur when a cell is classified as a grid cell based on its 1D firing pattern but it is not classified as a grid cell by the 2D gridness score.

**Supplementary Figure 9 - part 4 | All tetrode recordings in 2D and 1D**

**True negatives, part 1:**

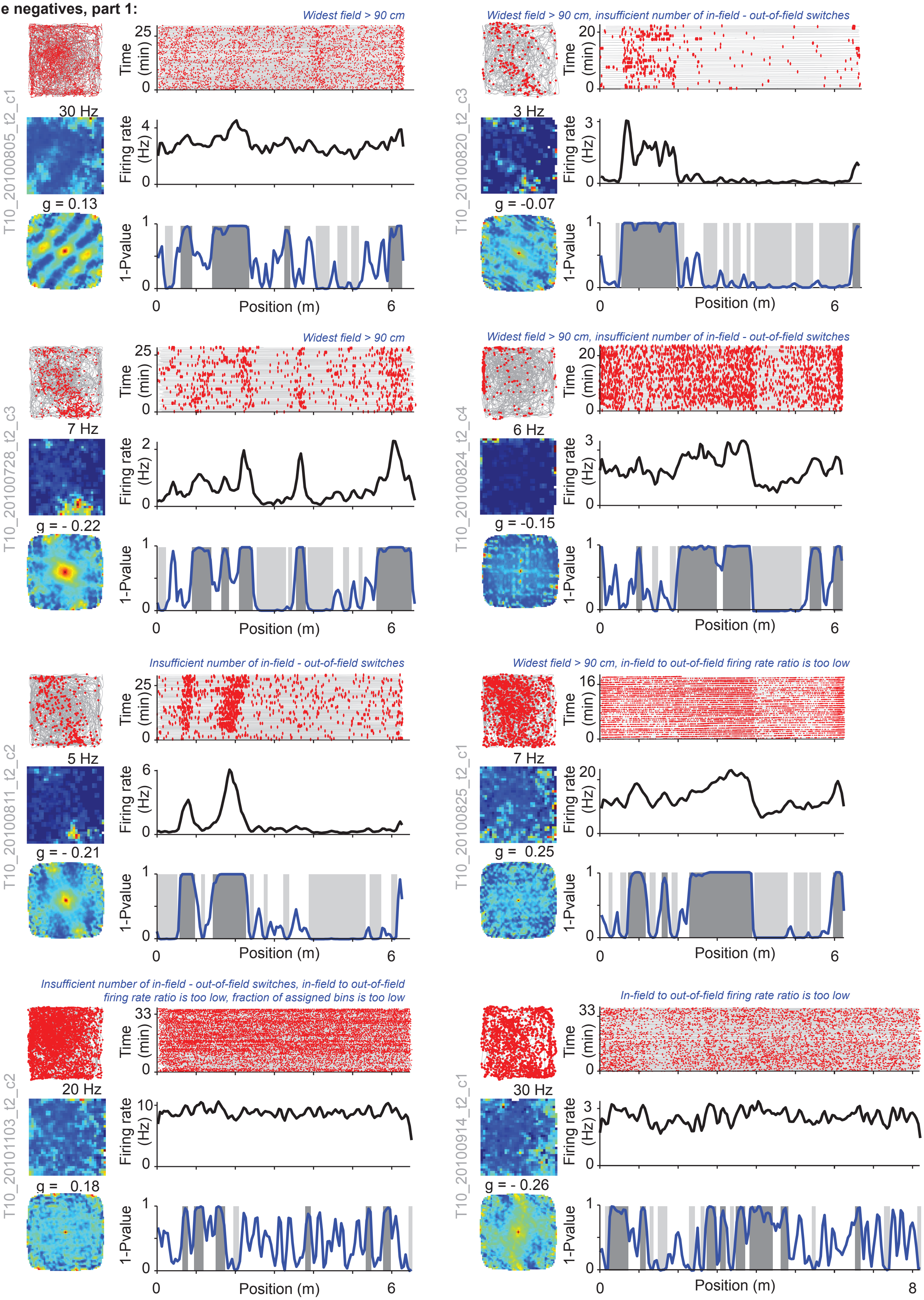

**Supplementary Figure 9 - part 5 | All tetrode recordings in 2D and 1D**

**True negatives, part 2:**

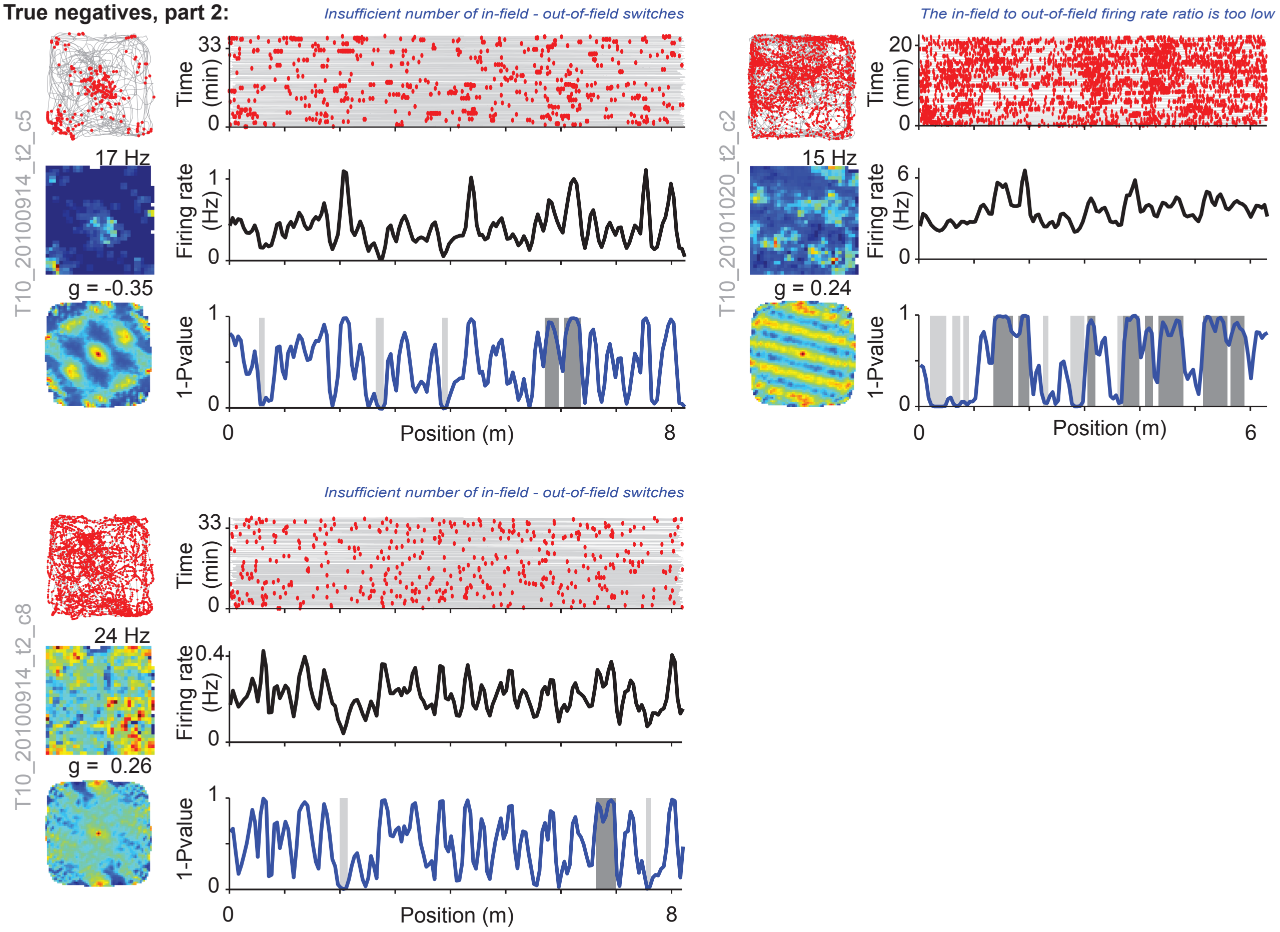

**Above: the 11 cells that were labeled as non-grid cells by both the 2D gridness score and the 1D classifier (true negatives).** Plots for each cell are as described for true positives. In addition, the reason(s) for which the classifier did not label each respective cell a grid cell is indicated in blue above the cell's 1D spike and trajectory plot (upper right). Many non - grid cells have spatially modulated firing in both 2D and 1D. We note that the criterion chosen for field width, while suitable for this data set, may not be suitable for recordings in larger 2D environments; a cell that is called a non-grid cell by both the 2D gridness score and the 1D classifier can still be a grid cell in a larger environment.

**False negatives, part 1 (grid cells according to the 2D gridness score that were *not* called grid cells by the 1D classifier):**

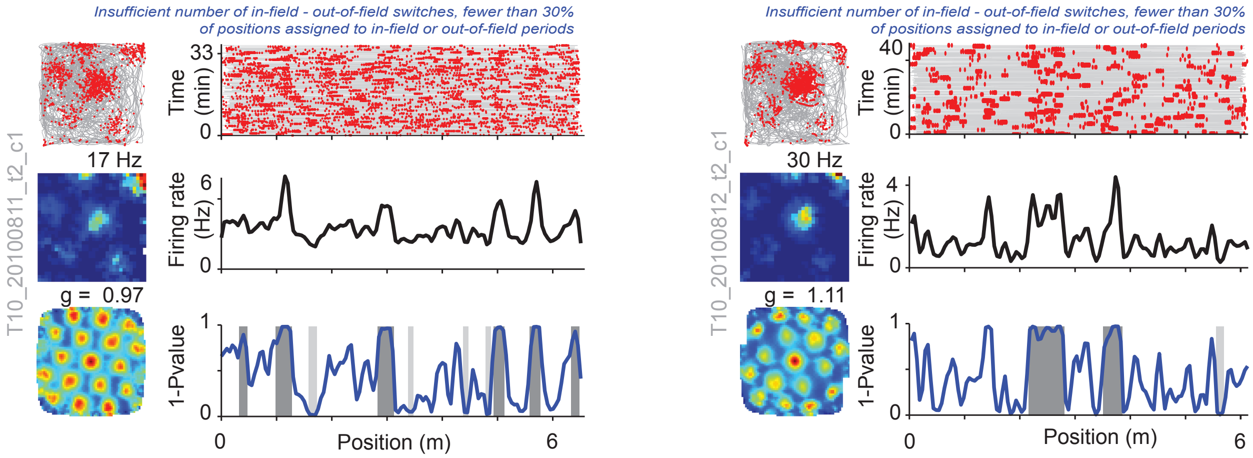

**Supplementary Figure 9 - part 6 | All tetrode recordings in 2D and 1D**

**False negatives, part 2:**

*Insufficient number of in-field - out-of-field switches, fewer than 30% of positions assigned to in-field or out-of-field periods*

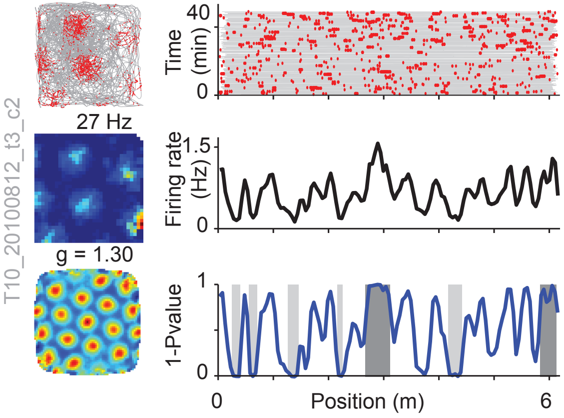

*Insufficient number of in-field - out-of-field switches, widest field is > 90 cm wide*

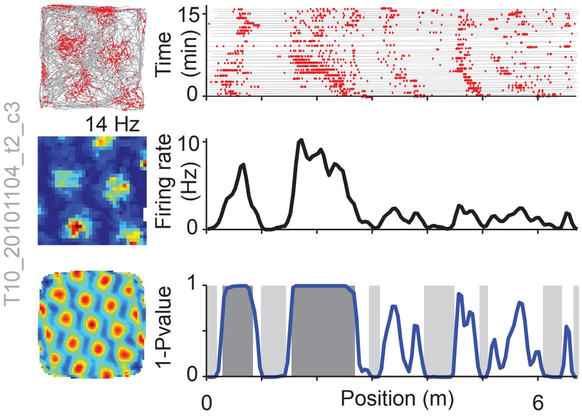

*The in-field to out-of-field firing rate ratio was too low*

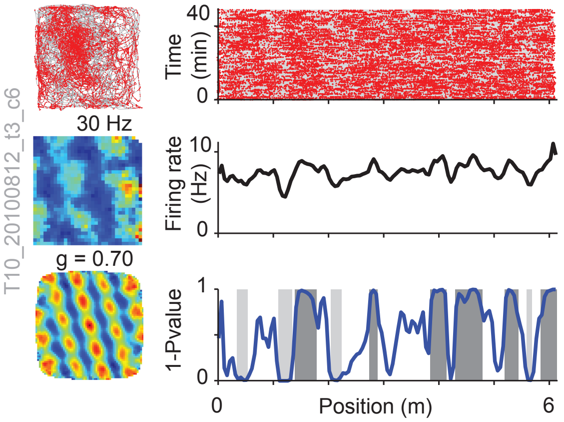

**Above: the 5 false negatives.** Plots for each cell are as described for true positives. In addition, the reason(s) for which the classifier did not label each respective cell a grid cell is indicated in blue above the cell's 1D spike and trajectory plot (upper right).

A subset of cells in 1D exhibit firing fields that drift during early portions of a recording (e.g. the top right example above). Drift can also be observed in recordings from real 1D tracks (e.g. Hafting et al. 2008), indicating that this is not a virtual reality effect. Whether such drift is also present in 2D data has not been examined. Because of the presence of this early drift, we note that the last 10 or 20 minutes of the respective recording sessions were used to generate the 1D plots used in Figure 2, rather than the entire ~15-~40 minute recording session. Drift during the initial portion of the 1D recordings here could be caused by the change in context between the 2D real recording session and the 1D virtual recording session.

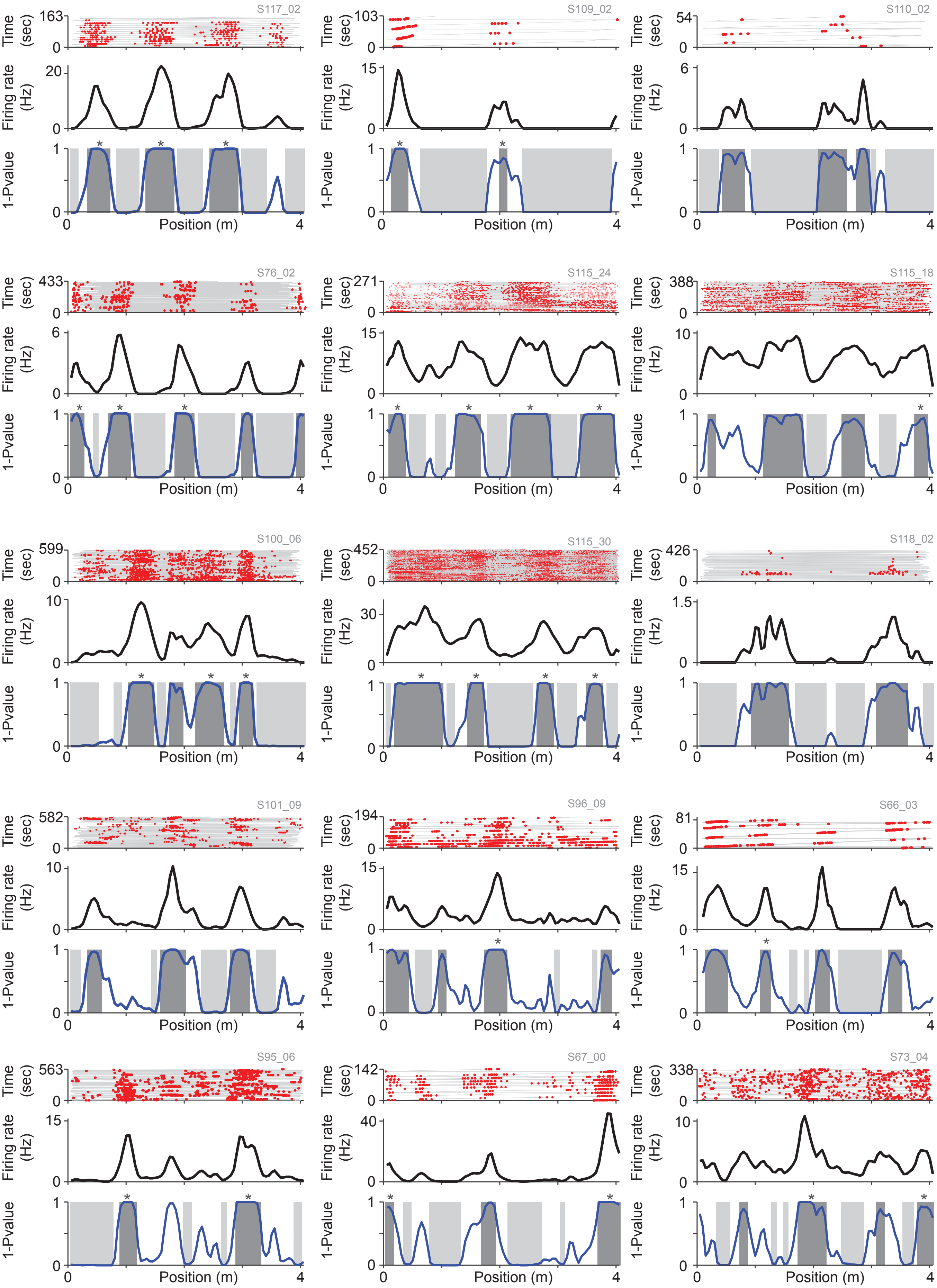

**Supplementary Figure 10 - part 1 | All whole-cell recordings from grid cells.**

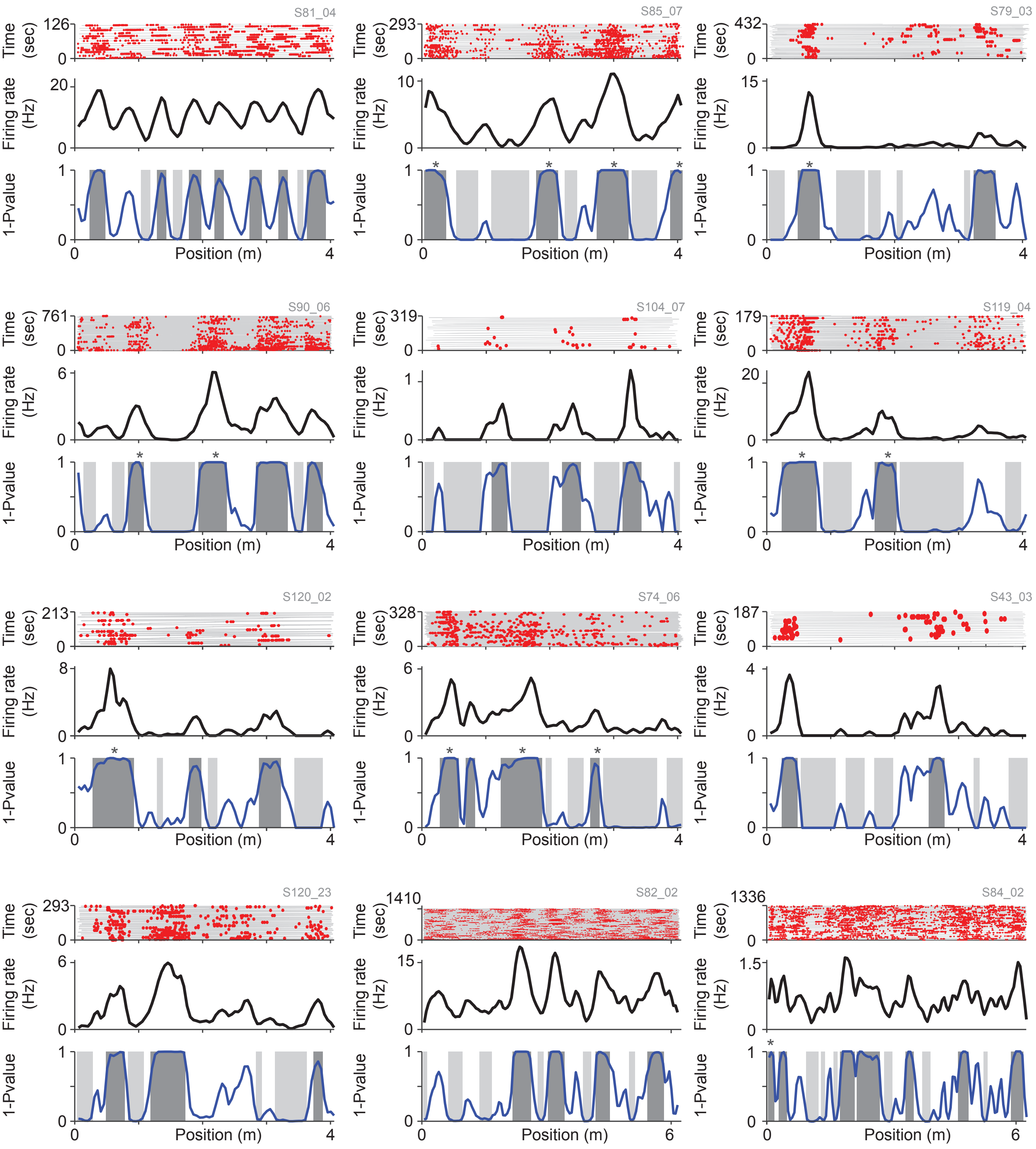

**Supplementary Figure 10 - part 2 | All whole-cell recordings from grid cells.** For each cell, top, spikes (red dots) and trajectory (grey trace) during multiple runs through the virtual 1D environment (shown stacked); middle, firing rate along the linear track; bottom, 1-Pvalue function (dark blue) along the track (firing fields are indicated with dark grey boxes and out-of-field periods with light grey boxes; a fraction of the track is not assigned to either an in-field or an out-of-field period). The virtual linear tracks used were typically 4m. The '*' above individual firing fields in the 1-Pvalue plots denote those that were considered highly stable (Methods). Only moving portions are shown, such that the original recording durations were always longer than the maximum time shown in these figures.

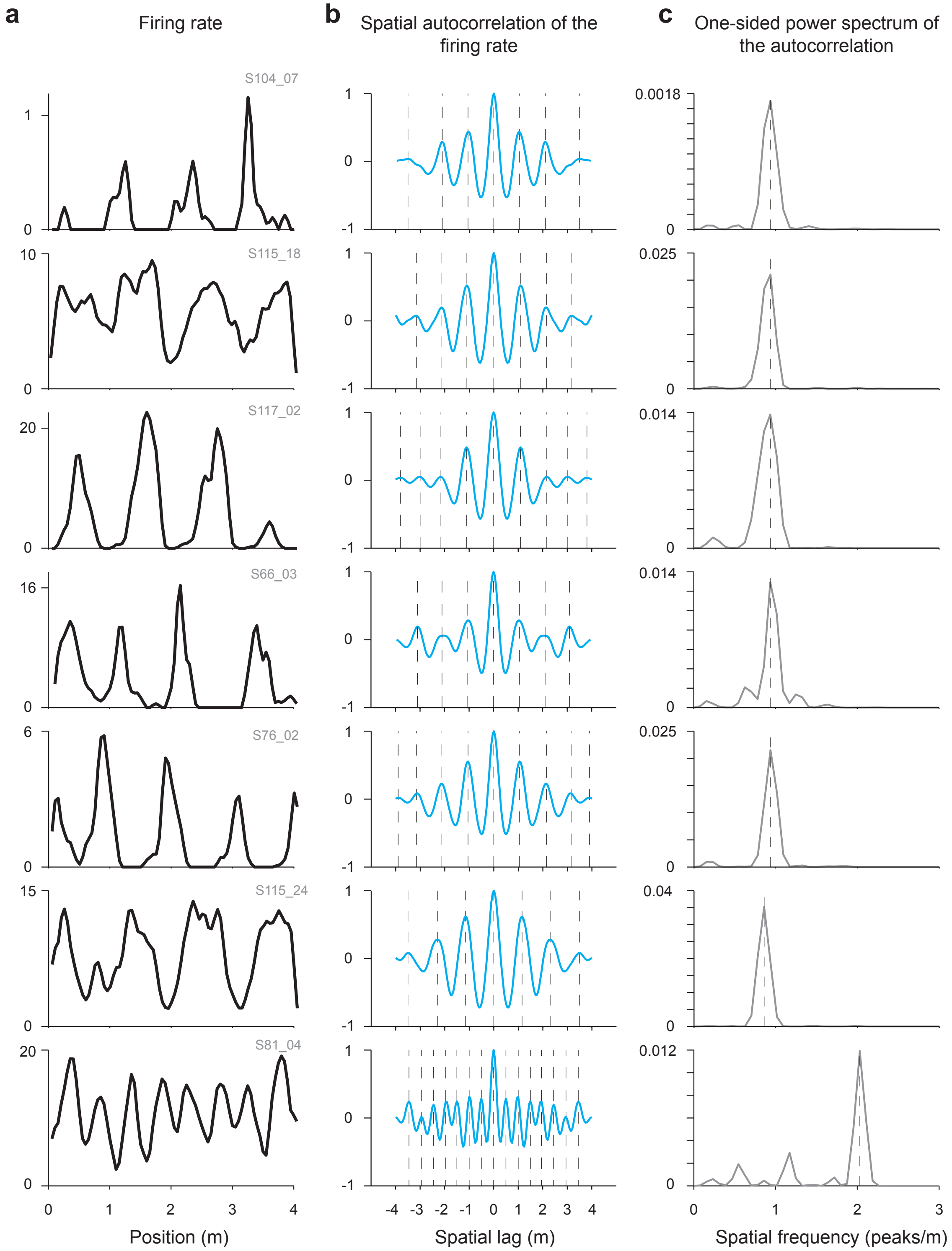

**Supplementary Figure 11 - part 1 | A subset of grid cells have highly regular firing fields. a,** Firing rates along the track of seven grid cells recorded in the whole-cell configuration that had highly regular firing fields (Methods). **b,** Spatial autocorrelation of the firing rate for each cell. The periodicity of the firing rate is reflected by the periodicity of the autocorrelation function. Note the relatively even spacing of the autocorrelation peaks (dashed lines), corresponding to evenly spaced peaks in the firing rate. **c,** One-sided power spectrum of the Fourier transform of the autocorrelation for each cell. Note the single peak at a spatial frequency corresponding with the spacing of the peaks in the firing rates shown in (a).

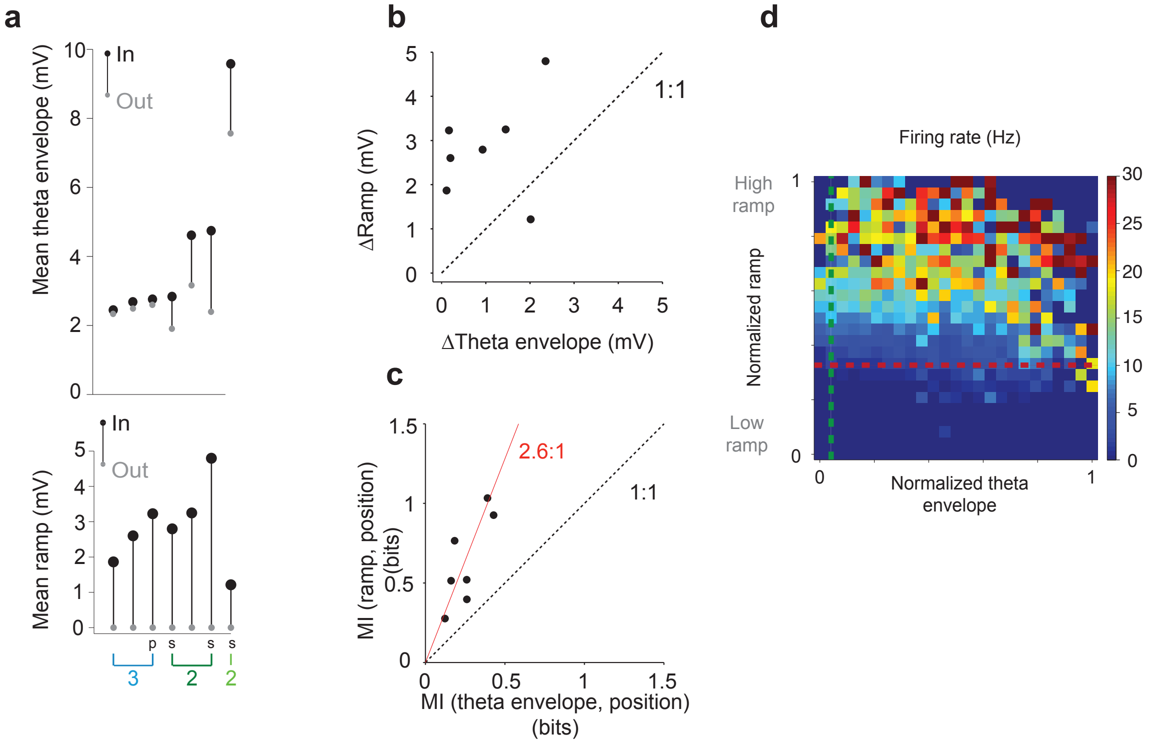

**Supplementary Figure 11 - part 2 | Highly periodic grid cells have the same properties as the rest of the recorded population.** To determine whether the relative importance of ramps and theta oscillations to field formation was also preserved in the subset of grid cells with highly regular firing fields, we repeated all analyses for the subset of highly periodic grid cells (Methods, firing rates shown in part 1). All analyses produced the same results for the highly periodic grid cells as for the whole population, indicating that the importance of ramps to grid cell firing, as seen in the population of 27 grid cells, was similar in the 7 grid cells with most regular firing fields. All the following statistical tests were from two-tailed Student's t-tests unless otherwise stated. **a,** Mean theta envelope (top) and mean ramp (bottom) during in-field (black dots) and out-of-field (grey dots) periods for all highly periodic grid cells ($n = 7$), sorted by mean out-of-field theta envelope. The layer (2 or 3) and morphology ('s', stellate and 'p', pyramidal) are indicated underneath; for layer 2, light green indicates large theta cells and dark green indicates small theta cells. As was true for the whole population, highly periodic grid cells had in-field increases in ramps and theta envelope. **b,** ΔRamp vs. ΔTheta envelope for highly periodic grid cells ($n = 7$). Dashed line indicates a 1:1 ratio. Highly periodic grid cells did not have a significantly different correlation between the average ramp or theta envelope and the average firing rate compared with the rest of the population (ramp: $t(25) = 0.13$, $p > 0.8$; theta: $t(25) = 0.26$, $p > 0.7$). As was true for the whole population, in highly periodic grid cells the average pairwise correlation between runs for ramp ($r = 0.34$) was significantly larger than for theta envelope ($r = 0.11$; $t(6) = 2.9$, $p < 0.05$, one-tailed *t*-test) and the highly periodic grid cells did not differ significantly from the rest of the population in average pairwise ramp or theta correlations (ramp: $t(25) = 0.45$, $p > 0.6$; theta: $t(25) = 1.16$, $p > 0.2$). **c,** As was true for the whole population, highly periodic grid cells demonstrated more information about position along the track in ramps than in theta envelope, with a mean ratio of 2.6 between the two quantities; highly periodic grid cells did not differ significantly from the rest of the population in terms of the information ratio ($t(25) = 0.25$, $p > 0.8$). **d,** Average firing rate for 7 highly periodic grid cells plotted in normalized ramp and theta amplitude coordinates. Cells spike for nearly all theta amplitudes (to the right of the green dashed line), but require the ramp amplitude to exceed a threshold (above the red dashed line). As was true for the whole population, spiking was present only in the upper ~62% of the range of the ramp but was present for nearly the whole range of theta values (~96%). The percentiles of the ramp and theta ranges where spiking began were not significantly different between highly periodic grid cells and the rest of the population (ramp: $t(25) = 1.18$, $p > 0.2$; theta: $t(25) = 0.6$, $p > 0.5$). Moreover, similarly to the whole population, the theta envelope decreased in ~20% of field traversals when compared with the out-of-field average while the ramp reliably increased in 96.1% of field traversals; the fractions of field traversals where theta and ramps decreased were not significantly different between highly periodic grid cells and the rest of the population (ramp: $t(25) = 0.01$, $p > 0.9$; theta: $t(25) = 0.6$, $p > 0.5$).

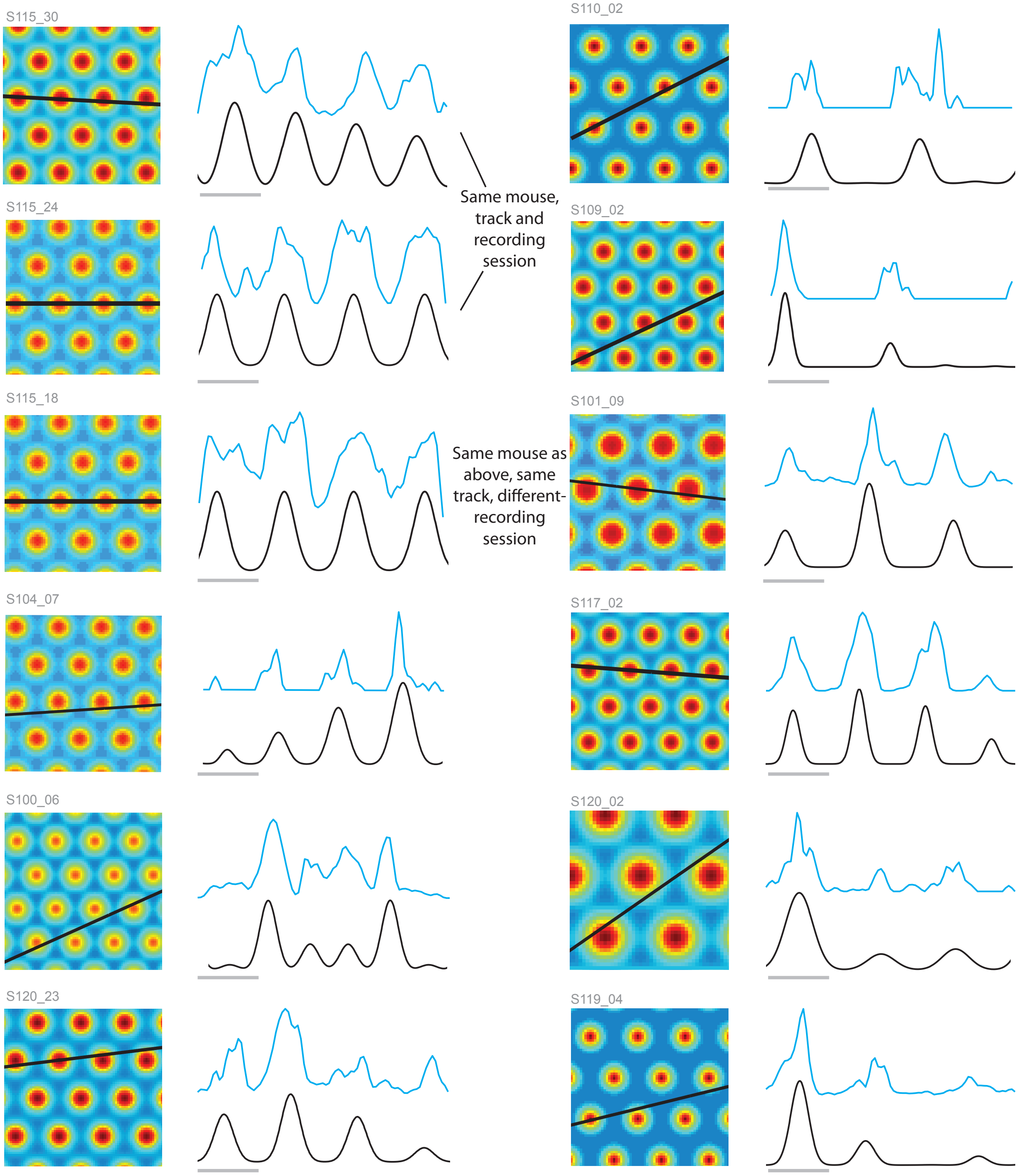

**Supplementary Figure 12 - part 1 | Grid cells recorded intracellularly along 1D tracks have firing rates that can be closely approximated by slices (1D cross-sections) through 2D grid fields.** Twelve cells are shown; right, blue - firing rates of grid cells recorded intracellularly along the virtual linear track (grey scale bars indicate 1m); right, black - firing rate along the black slice through each 2D grid field on the left. All slices of 2D grid fields were chosen manually to approximate the real cell's 1D firing rate; 2D colormaps were adjusted separately to best highlight the grid fields. All 2D fields used for slicing were created using a two-dimensional gaussian to approximate each field; all fields had the same peak amplitude, even though the peak firing rates of real grid cells can vary widely between different individual fields. Elliptical (rather than circularly symmetric) 2D fields were not explored, and 2D lattices used had 60 degree rotational symmetry. The spacing of the majority of 2D lattices used was ~1.1m between the two nearest fields, which is larger than the expected grid spacing of cells from this region of MEC. These plots indicate that it is at least in principle possible to obtain firing rates similar to those we observe in 1D by traversing an idealized 2D grid lattice along a straight line.

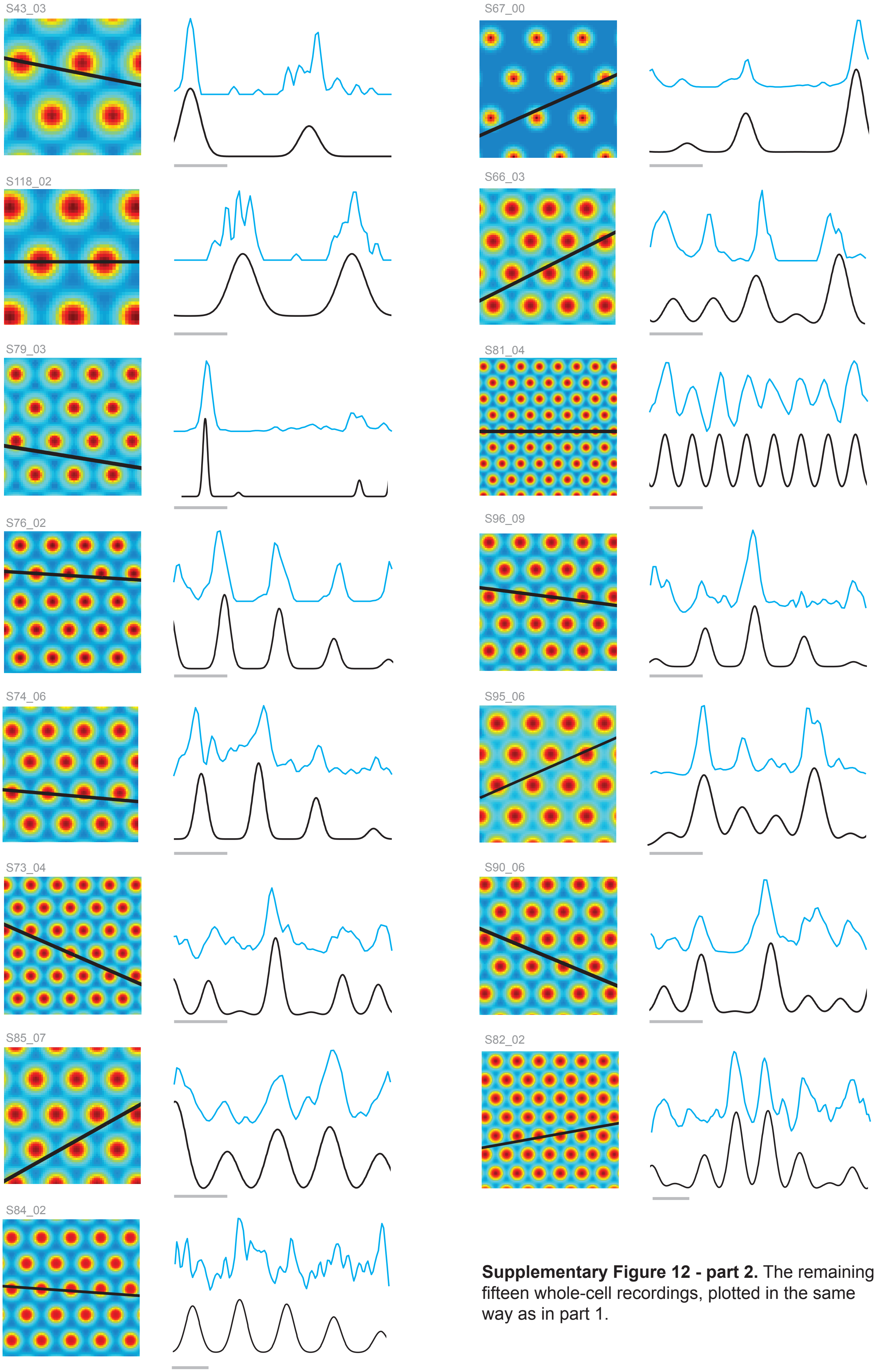

**Supplementary Figure 12 - part 2.** The remaining fifteen whole-cell recordings, plotted in the same way as in part 1.

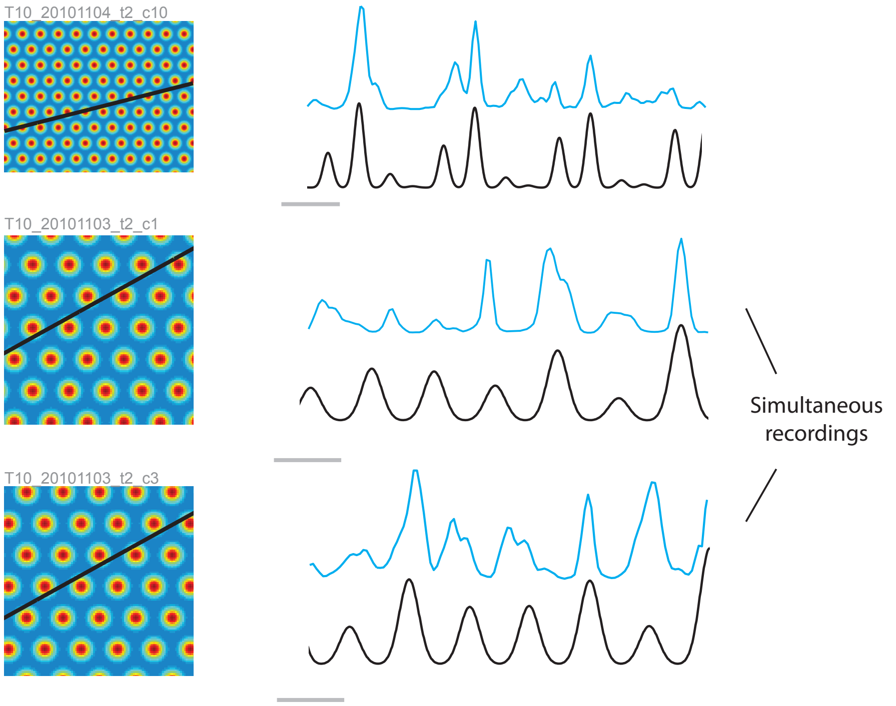

**Supplementary Figure 12 - part 3 | Slices through a 2D grid field that approximate the firing patterns of the three cells recorded with tetrodes from Figure 2**. Right, blue - firing rates of the three cells along the virtual linear track (grey scale bars are 1m); right, black - firing rate along the black slice through each 2D grid field on the left. All slices of 2D grid fields were chosen manually to approximate the real cell’s 1D firing rate; 2D colormaps were adjusted separately to best highlight the grid fields. The lower two cells were recorded simultaneously and had the same grid spacing in the 2D real environment (Fig. 2), suggesting that they might be part of the same grid ‘module’ (Stensola et al. 2012). The two cells were also recorded simultaneously in the 1D virtual track. This suggests that if their 1D track firing rates consist of slices through a 2D grid lattice, the slices should come from the same grid lattice and should be parallel. In this example, the two parallel slices of the same 2D grid lattice were used to match the recorded firing rates of both cells.

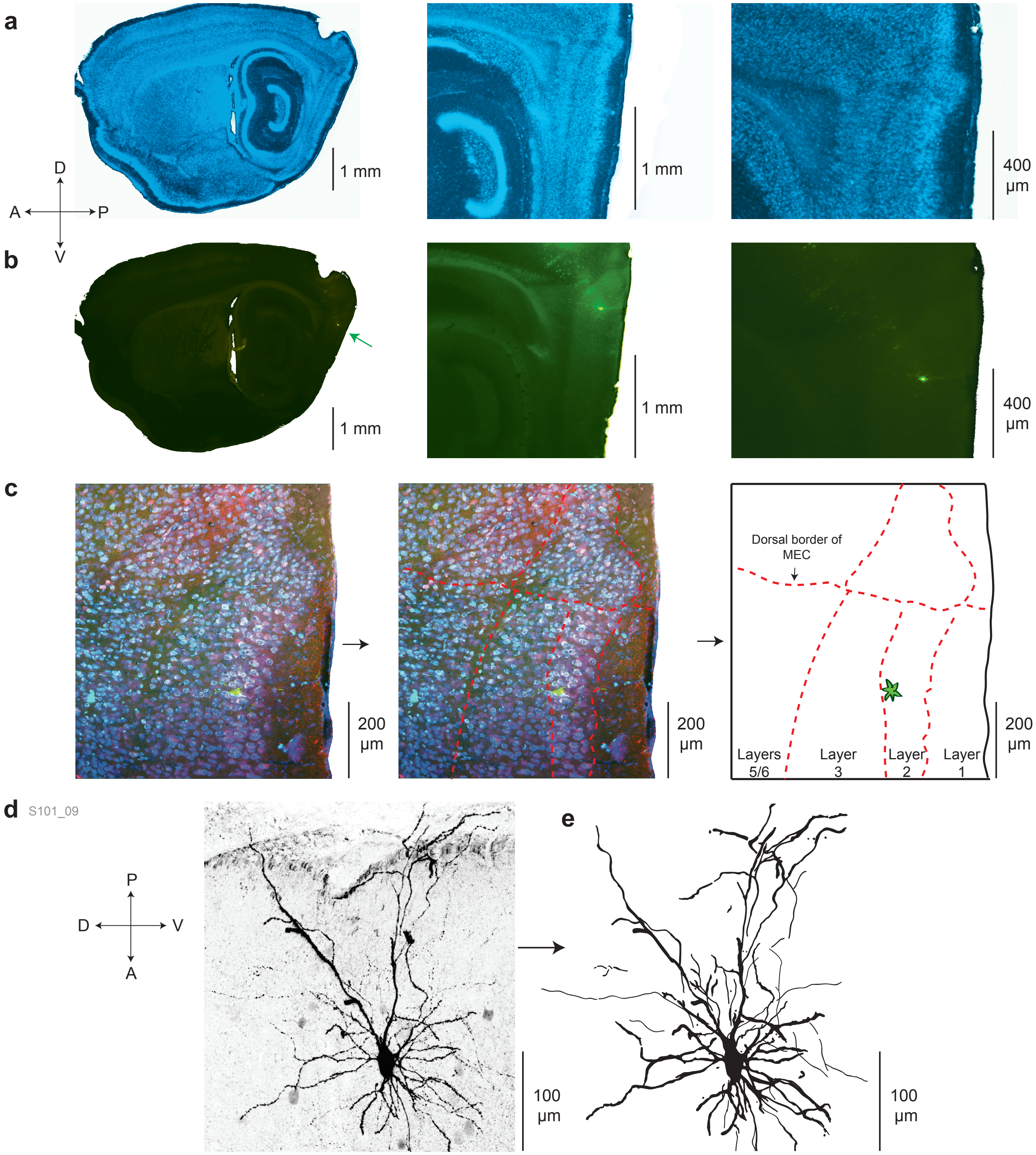

**Supplementary Figure 13 | Identification of the layer and morphology of a grid cell. a,** Blue fluorescent Nissl stain of the slice containing the cell body at three zoom levels. **b,** Green fluorescent Alexa 488-tagged streptavidin used to detect the biocytin delivered to the neuron during a whole-cell recording. **c,** Overlay of blue fluorescent Nissl stain revealing cell bodies; red fluorescence from Alexa 647-tagged anti-calbindin antibody used to reveal the dorsal border between MEC and large dorsal patches (these stain lightly for calbindin); green fluorescence from Alexa 488-tagged streptavidin as in (b). Together these labels can be used to distinguish layers 1, 2, and 3 of MEC and identify the dorsal border, such that cell bodies can be localized to one of the layers; The cell shown here was in layer 2. **d,** Maximum intensity projection obtained from a confocal stack of the cell revealing stellate morphology and **e,** tracing the cell's morphology.

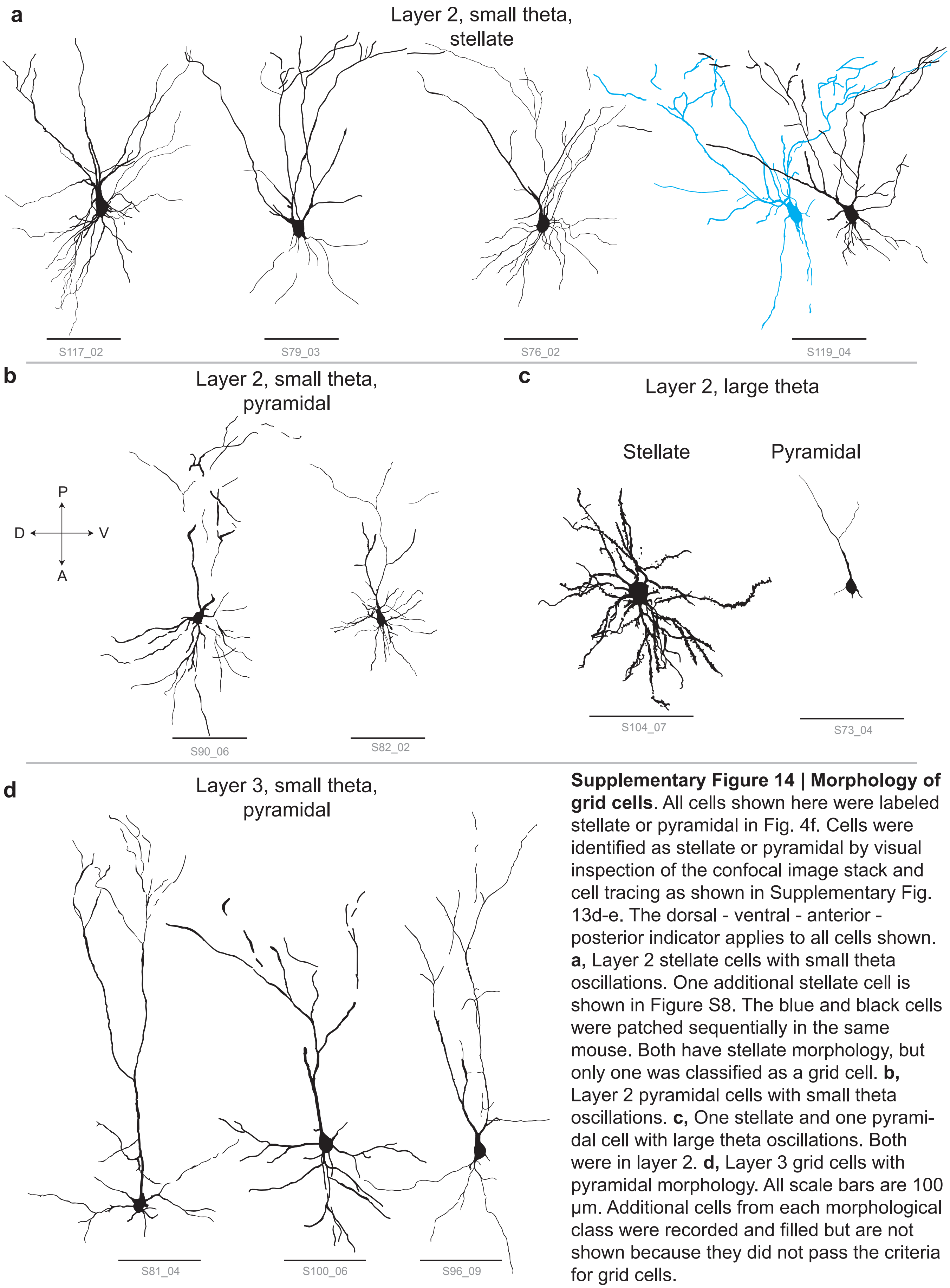

**Supplementary Figure 14 | Morphology of grid cells**. All cells shown here were labeled stellate or pyramidal in Fig. 4f. Cells were identified as stellate or pyramidal by visual inspection of the confocal image stack and cell tracing as shown in Supplementary Fig. 13d-e. The dorsal - ventral - anterior - posterior indicator applies to all cells shown. **a,** Layer 2 stellate cells with small theta oscillations. One additional stellate cell is shown in Figure S8. The blue and black cells were patched sequentially in the same mouse. Both have stellate morphology, but only one was classified as a grid cell. **b,** Layer 2 pyramidal cells with small theta oscillations. **c,** One stellate and one pyramidal cell with large theta oscillations. Both were in layer 2. **d,** Layer 3 grid cells with pyramidal morphology. All scale bars are 100 µm. Additional cells from each morphological class were recorded and filled but are not shown because they did not pass the criteria for grid cells.

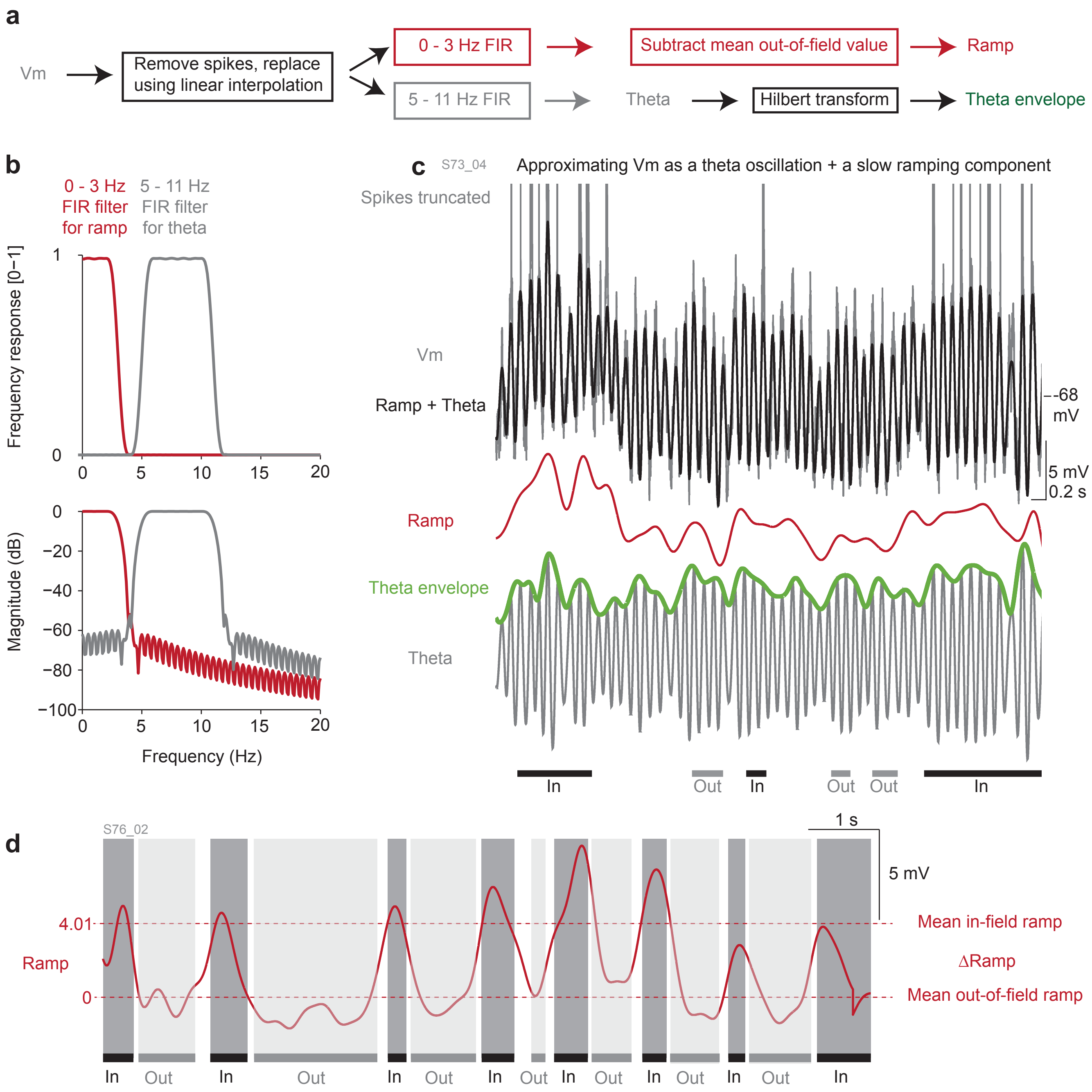

**Supplementary Figure 15 | The spike-free membrane potential can be decomposed into a ramp and a theta component. a,** Processing flow used to obtain the value of the ramp, theta, and theta envelope. **b,** The two filters used to extract the ramp and theta overlap minimally and have good attenuation (nearly 60 dB) at the point of overlap. **c,** Example decomposition of the membrane potential (upper grey trace; spikes are truncated) into a ramp (red trace) and a theta component (lower grey trace). The theta envelope (green trace) is always positive. The sum of the ramp and theta components (black trace overlaid on the membrane potential) closely approximates Vm without the spikes. This example is from a large theta cell. **d,** After the ramp filter is applied to the spike-free membrane potential, the mean out-of-field value - which is approximately equal to the baseline membrane potential - is subtracted from the result to obtain the ramp. As a result, the mean out-of-field ramp is set to 0. ΔRamp is defined as the mean in-field ramp (marked by dark grey boxes) minus the mean out-of-field ramp (marked by light grey boxes). The value of ΔRamp is not influenced by the baseline subtraction. Only one value for ΔRamp is obtained from the whole recording. ΔTheta envelope is defined as the mean in-field theta envelope minus the mean out-of-field theta envelope.

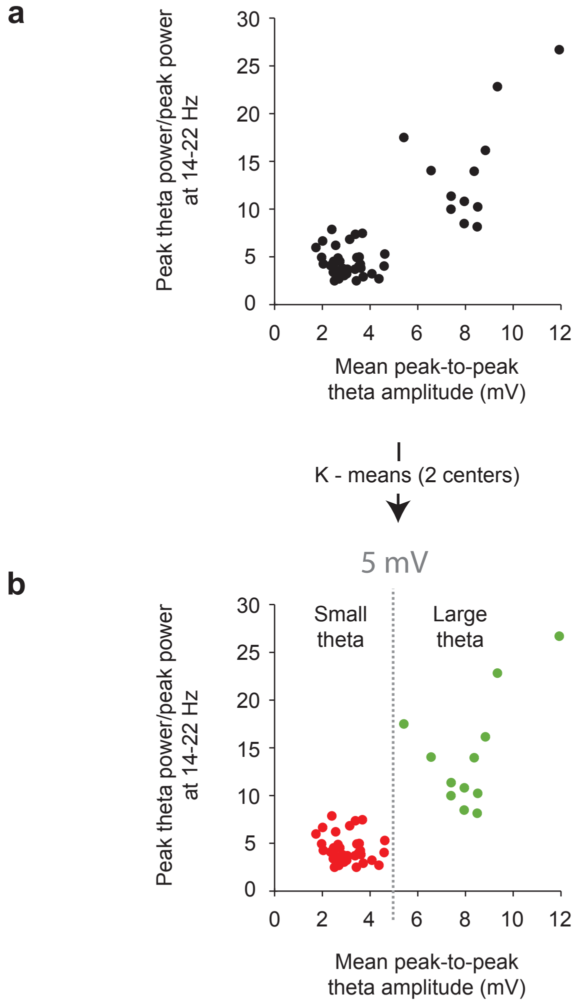

**Supplementary Figure 16 | Discriminating large and small theta cells.** Large theta cells have large peak-to-peak theta oscillations as well as a large ratio between the peak power in the theta band and the peak power in the 14 - 22 Hz band. The combination of these two features can be used to discriminate large and small theta cells. **a,** Plotting the relationship between the peak theta to 14 - 22 Hz power ratio and the mean peak-to-peak theta amplitude for all recorded neurons (including non-grid cells) reveals two distinct clusters. **b,** K-means successfully identifies these clusters. In this data set, a single threshold on the peak-to-peak theta amplitude (at 5 mV, dashed line) was sufficient to discriminate between these two clusters. This threshold was therefore used to classify cells as large and small theta cells.

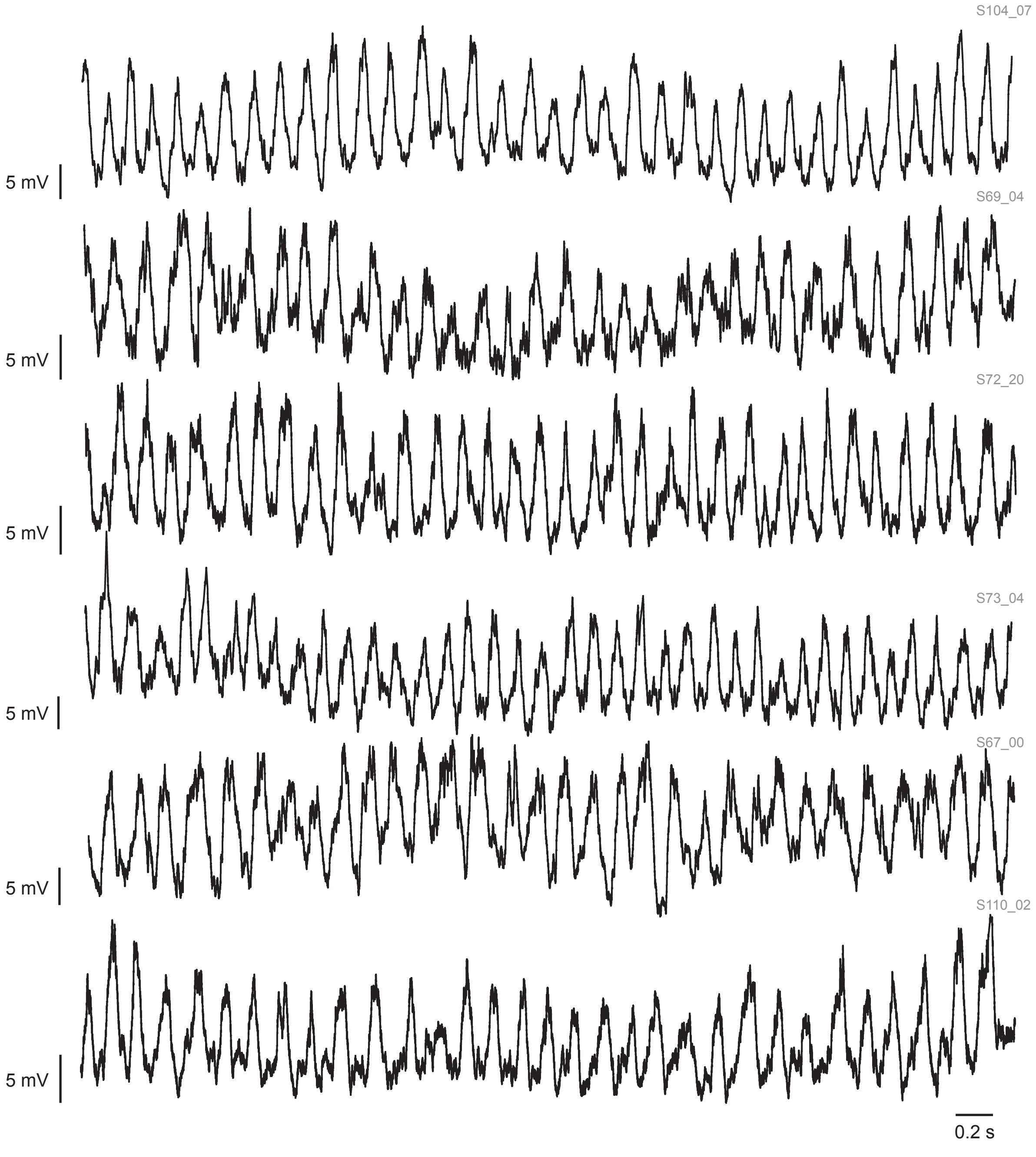

**Supplementary Figure 17 | Oscillations in large theta cells.** Six examples of the membrane potential (with spikes removed) showing large subthreshold oscillations from six different large theta cells (5 seconds long).

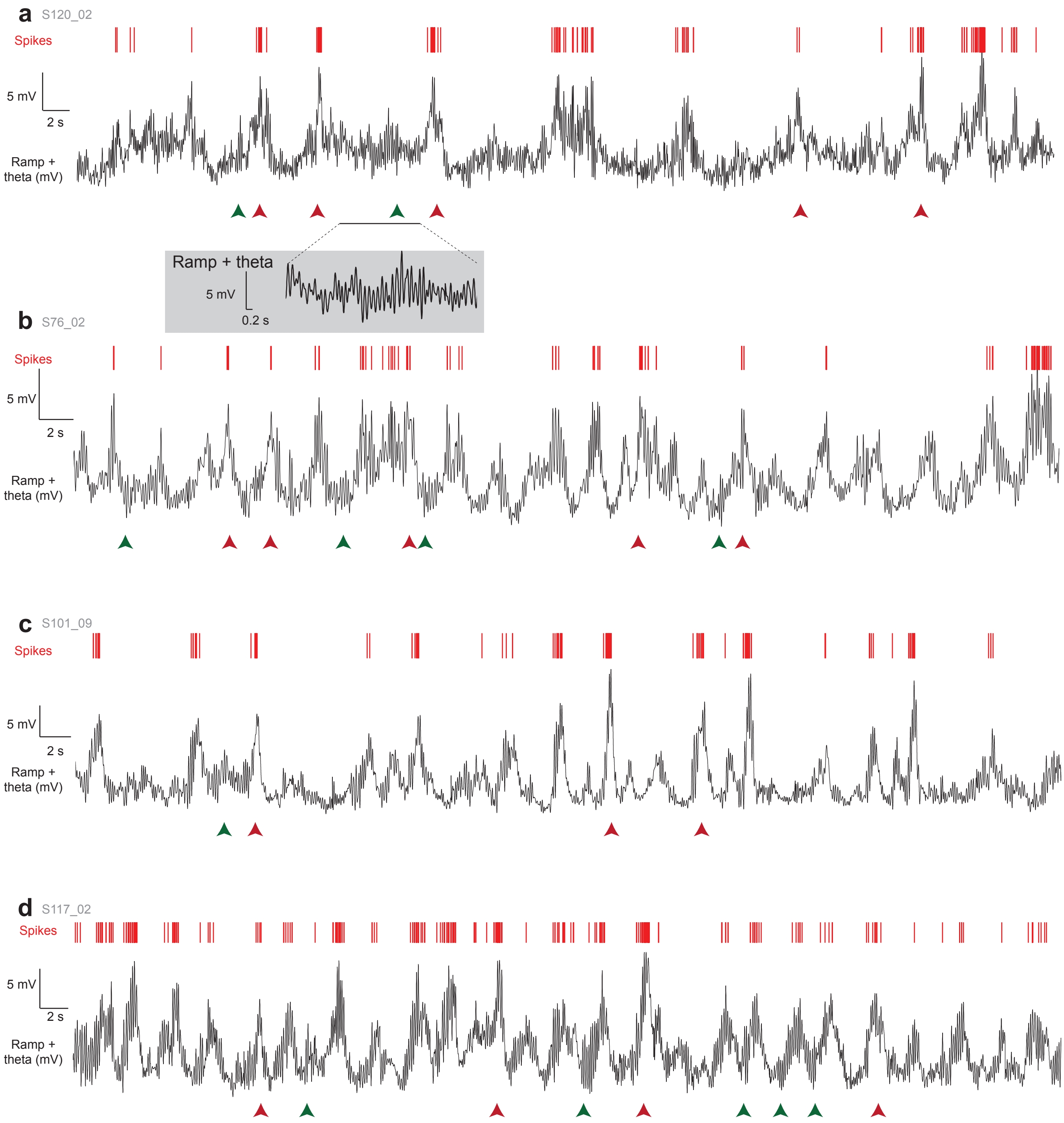

**Supplementary Figure 18 | Part 1 - Layer 2 small theta cells have robust ramps underlying firing fields.** **a,b,c,d,** Four example layer 2 small theta grid cells with spikes (red lines) shown above the value of the ramp + theta (black traces). Note the presence of clear ramps of depolarization during periods when the cell spikes. At this temporal resolution, individual theta cycles are not easily discerned; the changing theta amplitude is reflected in the changing thickness of the black ramp + theta traces, as illustrated by the zoomed portion of (a). Compare ramp, theta amplitudes and spiking at red vs. green arrowheads of a cell. Red arrowheads point to firing field traversals where the cell spikes successfully even though the theta amplitude is either low or comparable to the theta amplitue during nearby periods where the cell does not spike. Conversely, green arrowheads point to out-of-field periods where theta is large between two ramps, but the cell does not spike, illustrating that an increase in theta amplitude (within the shown range) is not sufficient to drive spiking.

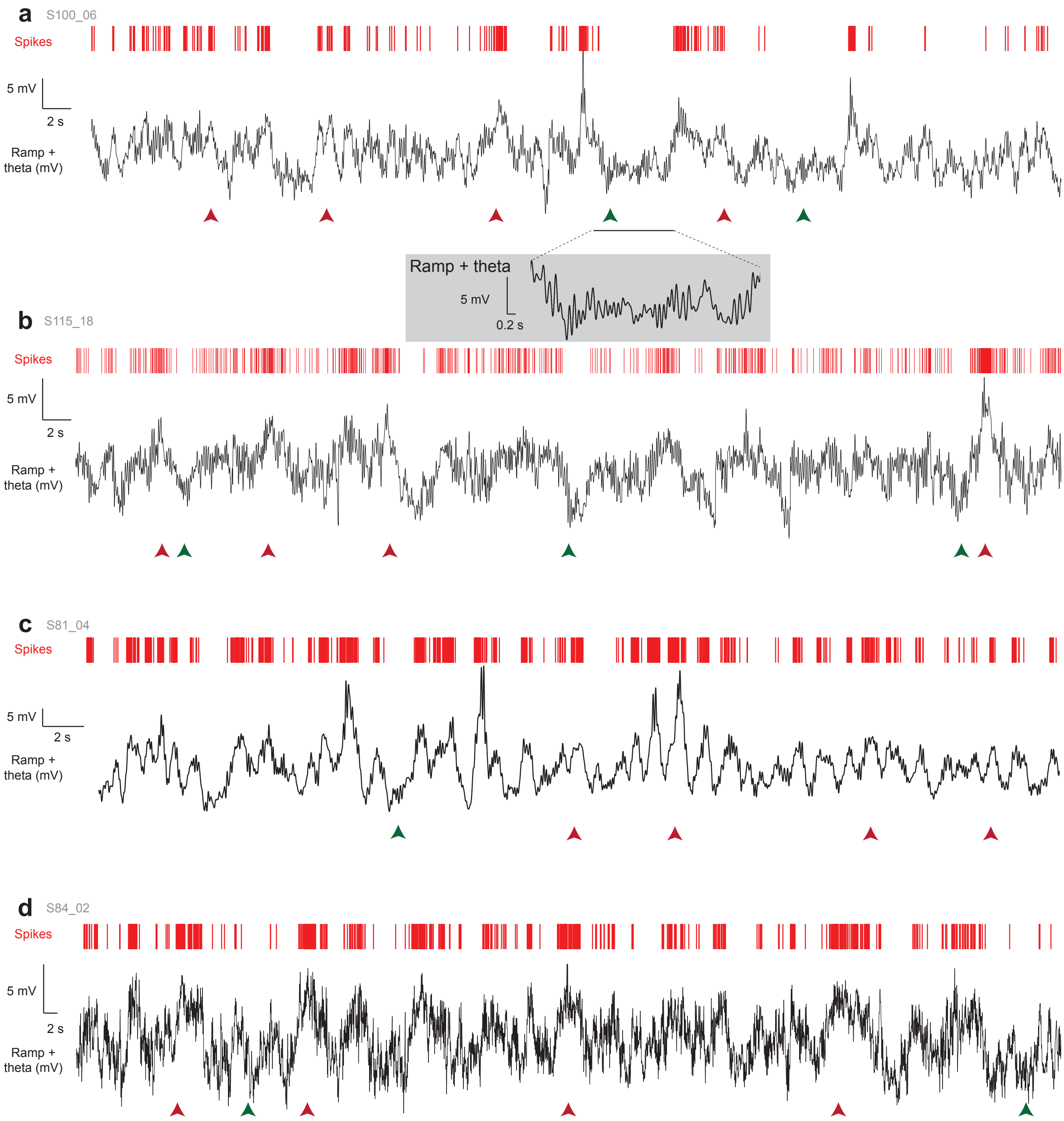

**Supplementary Figure 18 | Part 2 - Layer 3 cells have robust ramps underlying firing fields. a,b,c,d,** Four example layer 3 grid cells with spikes (red lines) shown above the value of the ramp + theta (black traces). Note the presence of clear ramps of depolarization during periods when the cell spikes. At this temporal resolution, individual theta cycles are not easily discerned; the changing theta amplitude is reflected in the changing thickness of the black ramp + theta traces, as illustrated by the zoomed portion of (a). Compare ramp, theta amplitudes and spiking at red vs. green arrowheads of a cell. Red arrowheads point to firing field traversals where the cell spikes successfully even though the theta amplitude is either low or comparable to the theta amplitue during nearby periods where the cell does not spike. Conversely, green arrowheads point to out-of-field periods where theta is large between two ramps, but the cell does not spike, illustrating that an increase in theta amplitude (within the shown range) is not sufficient to drive spiking.

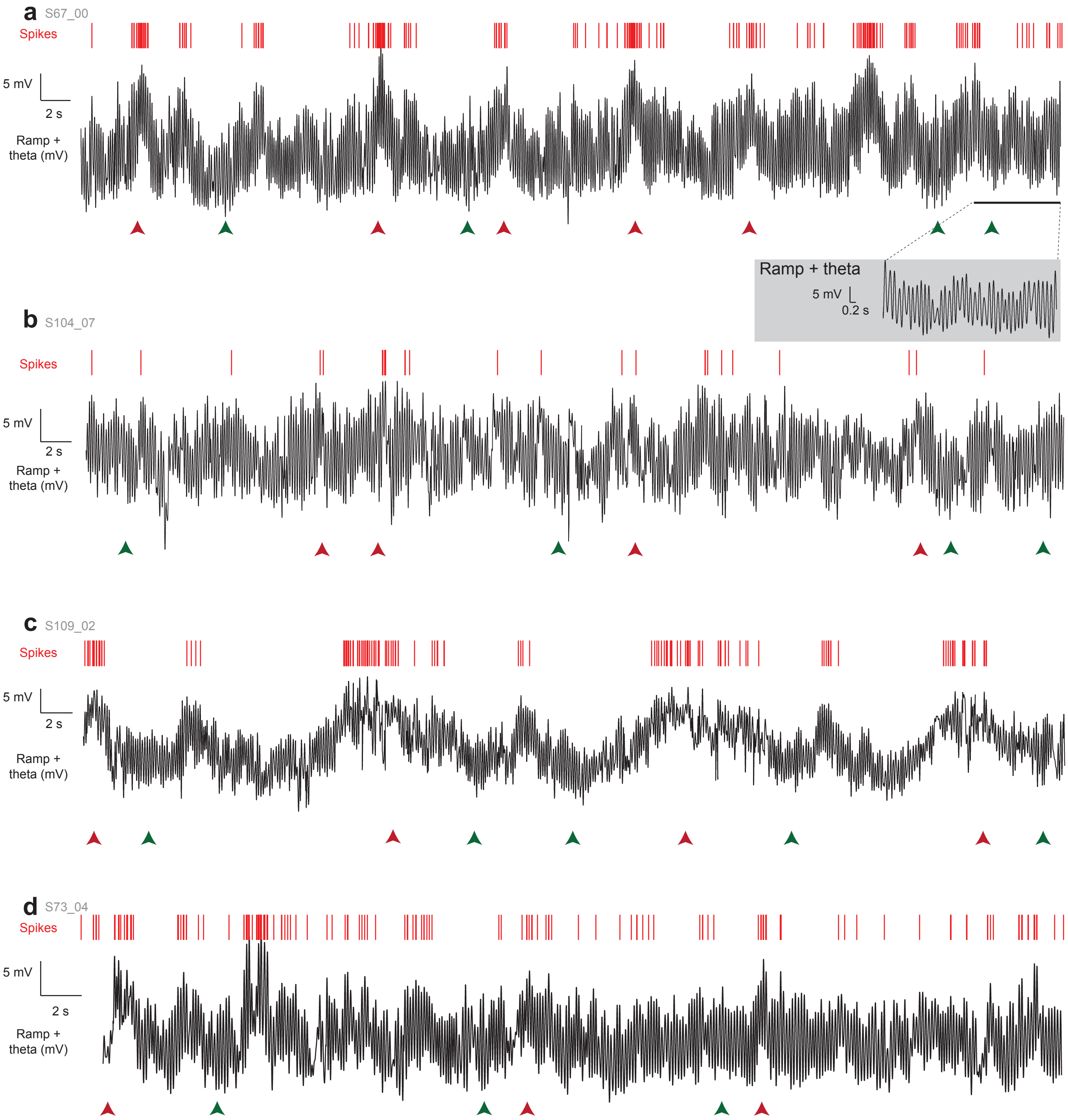

**Supplementary Figure 18 | Part 3 - Large theta cells have robust ramps underlying firing fields. a,b,c,d,** Four example large theta grid cells with spikes (red lines) shown above the value of the ramp + theta (black traces). Note the presence of clear ramps of depolarization during periods when the cell spikes. At this temporal resolution, individual theta cycles are not easily discerned; the changing theta amplitude is reflected in the changing thickness of the black ramp + theta traces, as illustrated by the zoomed portion of (a). Compare ramp, theta amplitudes and spiking at red vs. green arrowheads of a cell. Red arrowheads point to firing field traversals where the cell spikes successfully even though the theta amplitude is either low or comparable to the theta amplitue during nearby periods where the cell does not spike. Conversely, green arrowheads point to out-of-field periods where theta is large between two ramps, but the cell does not spike, illustrating that an increase in theta amplitude (within the shown range) is not sufficient to drive spiking.

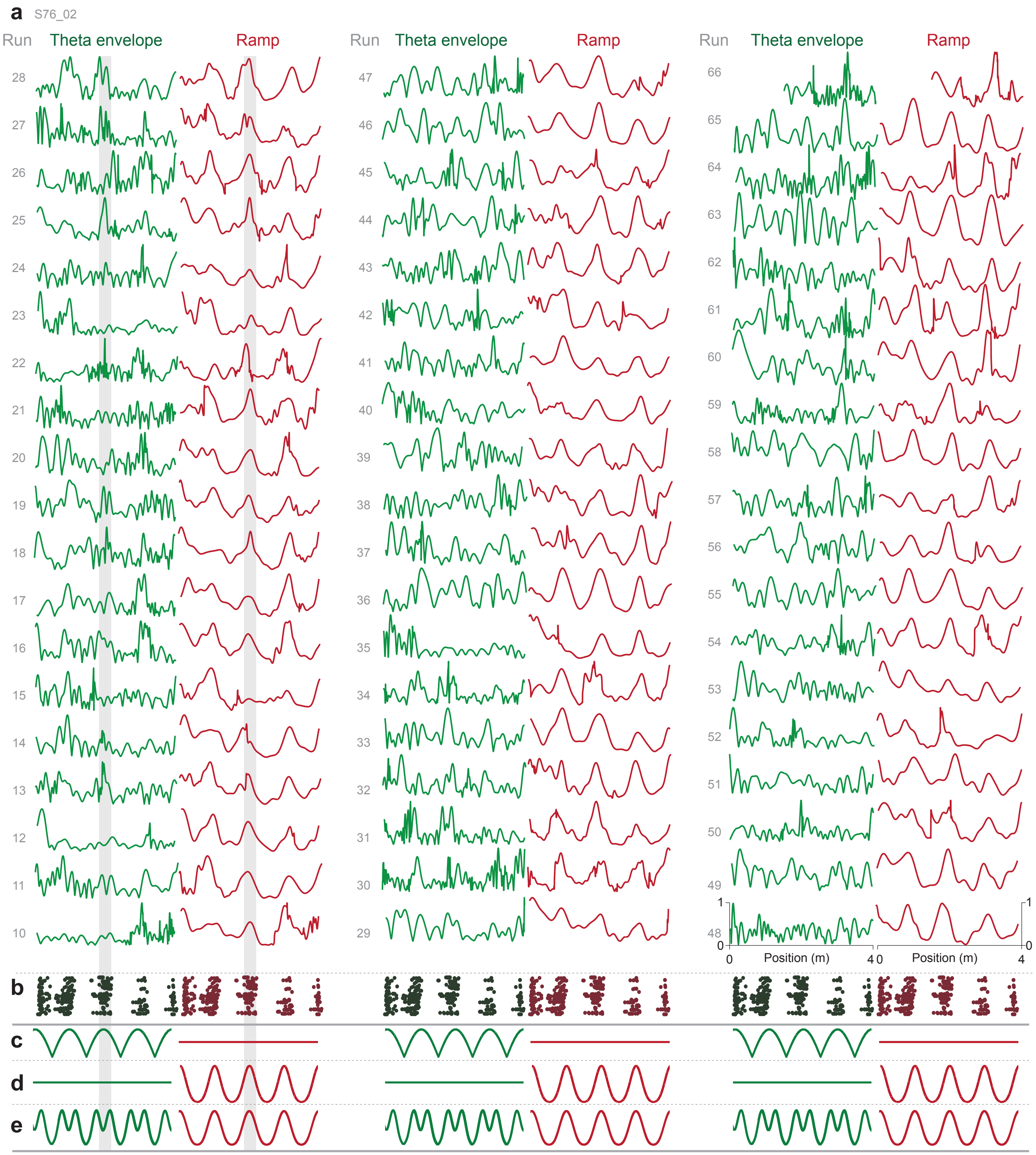

**Supplementary Figure 19 | Part 1 - layer 2 small theta cell. Ramps increase in-field reliably on nearly every run, while theta is much more variable**. **a,** Theta envelope (green traces) and ramp (red traces) plotted separately for individual runs along the linear track for one layer 2 small theta grid cell (from Figure 3). The amplitude of ramps and theta envelope is normalized to 0 - 1 on every run to facilitate comparison (axes are indicated on run 48, bottom right, but omitted from other runs for clarity). **b,** Stacked runs of the cell with spike locations, repeated six times in alternating green and red. The third field (left) is indicated by a grey box. The ramp increases reliably in this field on nearly all runs and there are the same number of peaks in the ramp trace as there are firing fields. In contrast, the theta envelope does not increase reliably in this field on every run (e.g. runs 10, 12, 20, 21, 23); Moreover, there are often more peaks in the theta amplitude than there are fields (e.g. runs 49, 63). **c,d,e,** Same procedure applied to the predicted ramp and theta envelope for interference (c), attractor (d), and attractor with added theta (e) models (normalized from Figure 1). Compare the real run by run ramp and theta envelope with model predictions.

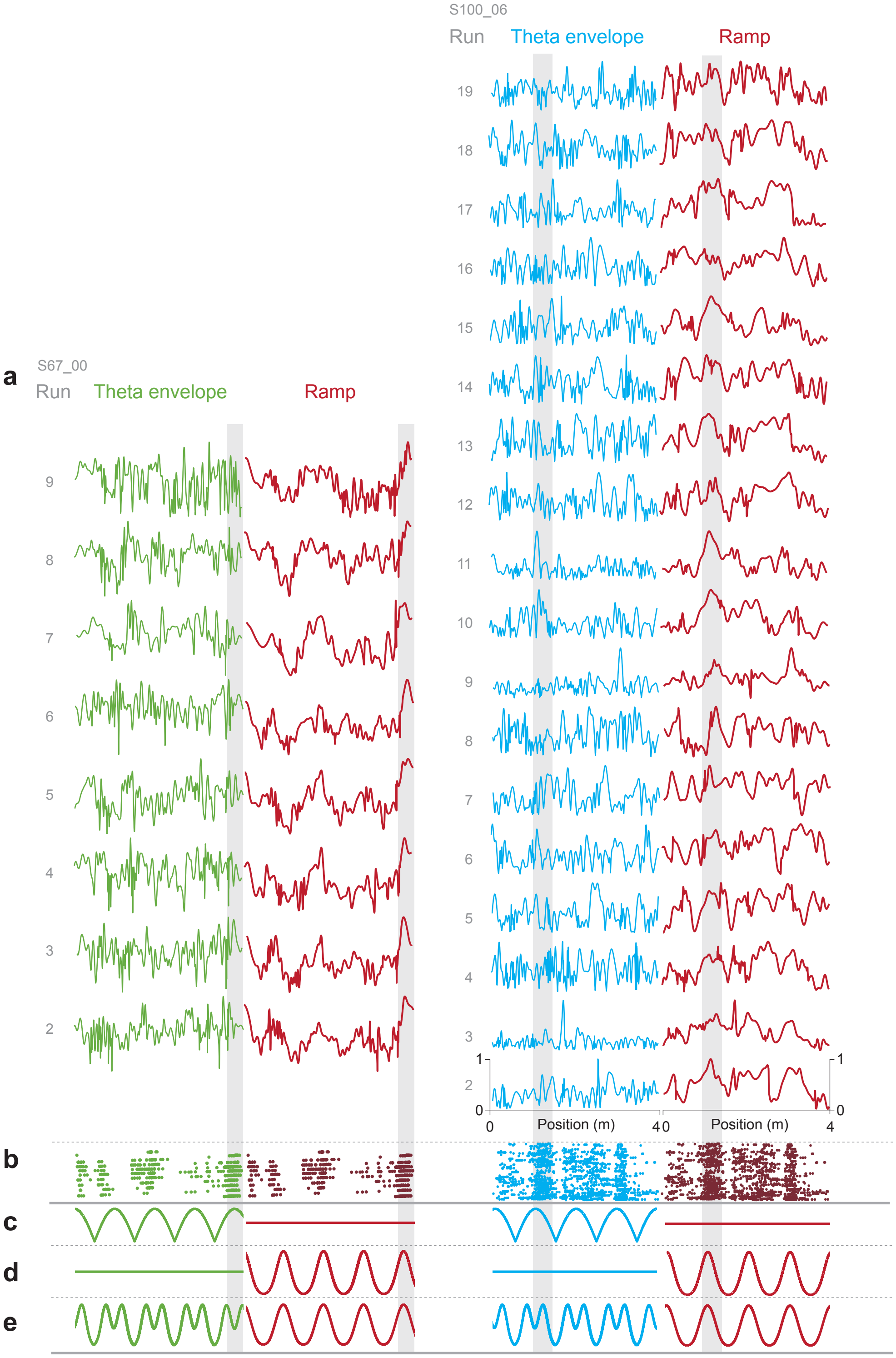

**Supplementary Figure 19 | Part 2 - layer 3 and large theta cells. Ramps increase in-field reliably on nearly every run, while theta is much more variable**. All plots are the same as in part 1. a, Left (light green), large theta cell. Right (blue) layer 3 cell.

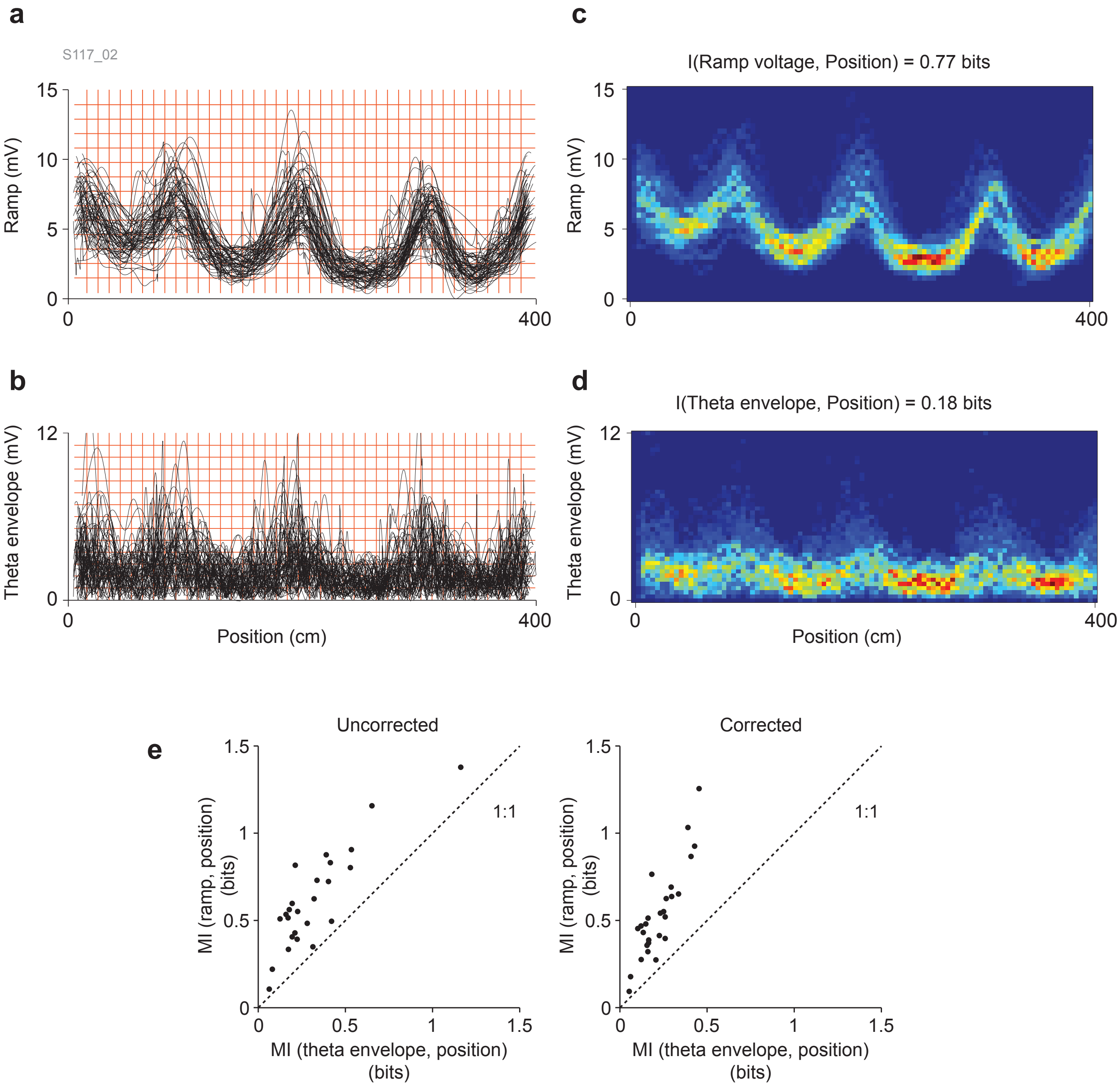

**Supplementary Figure 20 | Procedure used for mutual information analysis. a,** Superimposed ramp versus position waveforms for the complete set of 66 full runs along the track for a grid cell recording. **b,** Corresponding theta envelope vs. position waveforms on the same set of runs. Orange grids indicate schematically how bins were employed in order to calculate probability distributions. The same number of vertical (ramp or theta envelope) and horizontal (position) bins were used for both ramp and theta envelope (the number of bins shown here is reduced for visibility. 100 position bins and 40 ramp or theta envelope bins were used). **c,** Probability distribution of ramp vs. position using the binned data. **d,** Probability distribution of theta envelope vs. position using the binned data. **e,** Mutual information bewteen ramp and position plotted vs mutual information between the theta envelope and position; each dot represents a single cell (n = 27). Left: mutual information calculated without corrections for sampling bias. Right: mutual information after correcting for sampling bias (ratio of samples to bins (i.e. N/m) was >30:1). Mutual information and bias corrections were performed using the ‘entropy’ package in R (Methods). To understand the expected values of MI, note that if the sum of the lenths of in-field regions was ½ of the total track length, and the membrane voltage being analyzed was a constant value V(in-field) within firing fields of all runs and a constant value V(out-of-field) in the out-of-field periods, then the MI(V,position) would be 1 bit. If the voltage was constant across the whole track on every run, then MI(V, position) = 0 bits. Thus, qualitatively, we expect MI values in the range (0,1).

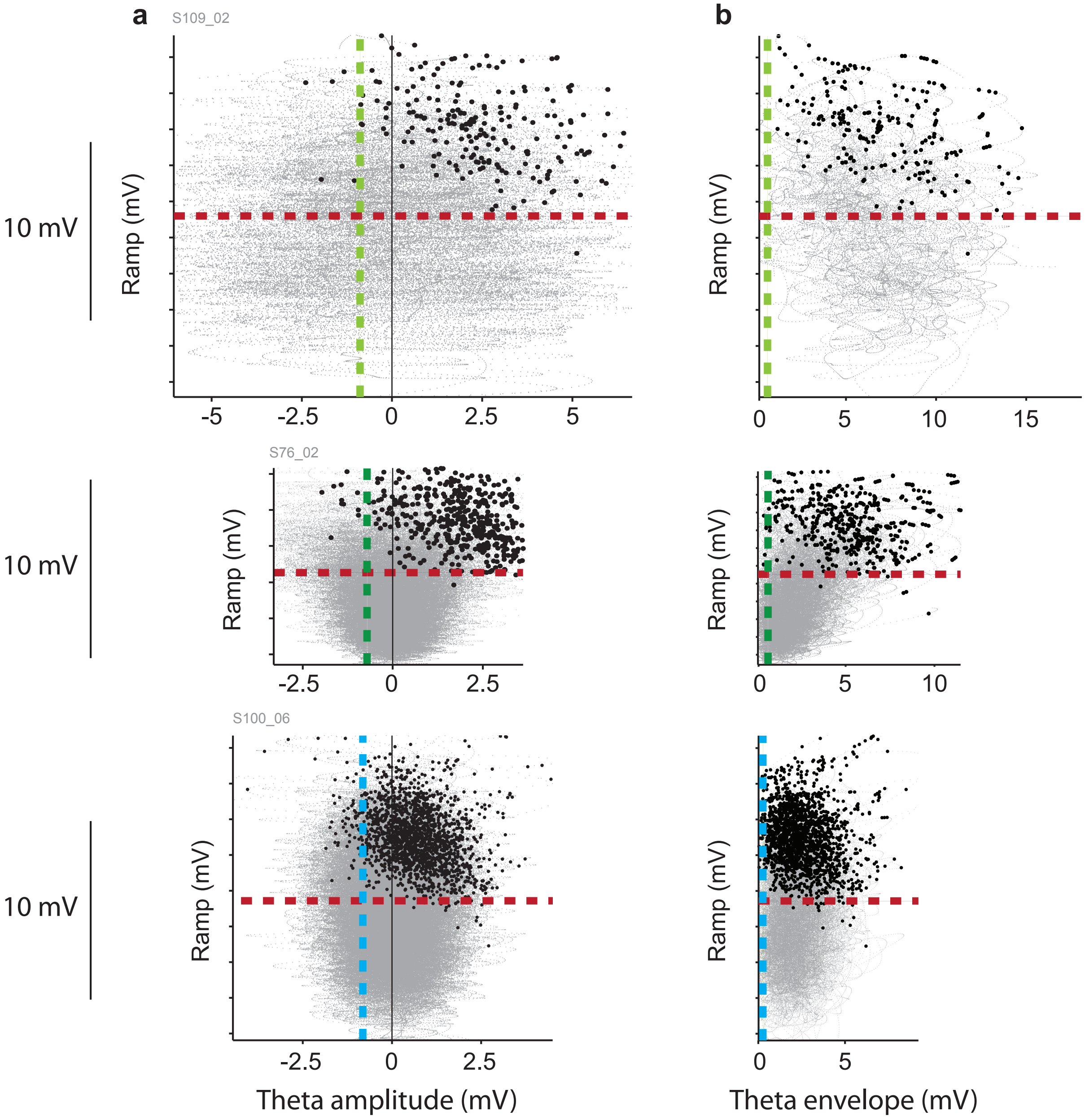

**Supplementary Figure 21 | Spiking in relation to the ramp, theta amplitude and theta envelope**. **a,** Distribution of ramp and theta *amplitude* for the whole duration of a recording (grey dots) and when the cell spikes (overlaid black dots) for 3 example grid cells (top: large theta, middle: layer 2 small theta, bottom: layer 3). These are the same cells shown in Figure 5c. Theta amplitude can be both positive and negative, corresponding to the upward and downward portion of theta cycles. These plots demonstrate that spiking occurs above a ramp threshold (above the dashed red lines). When the cell is above this ramp threshold, spiking is most likely on the positive portion of theta cycles (to the right of the blue or green dashed lines). **b,** Distribution of ramp and theta *envelope* for the whole duration of a recording (grey dots) and when the cell spikes (overlaid black dots) for the same cells as in (a). These plots are the same as those in Figure 5c, except that the axes are not normalized. For all plots, 99% of spikes occurred at a higher ramp than the dashed red lines and at a higher theta envelope than the dashed green or blue lines.

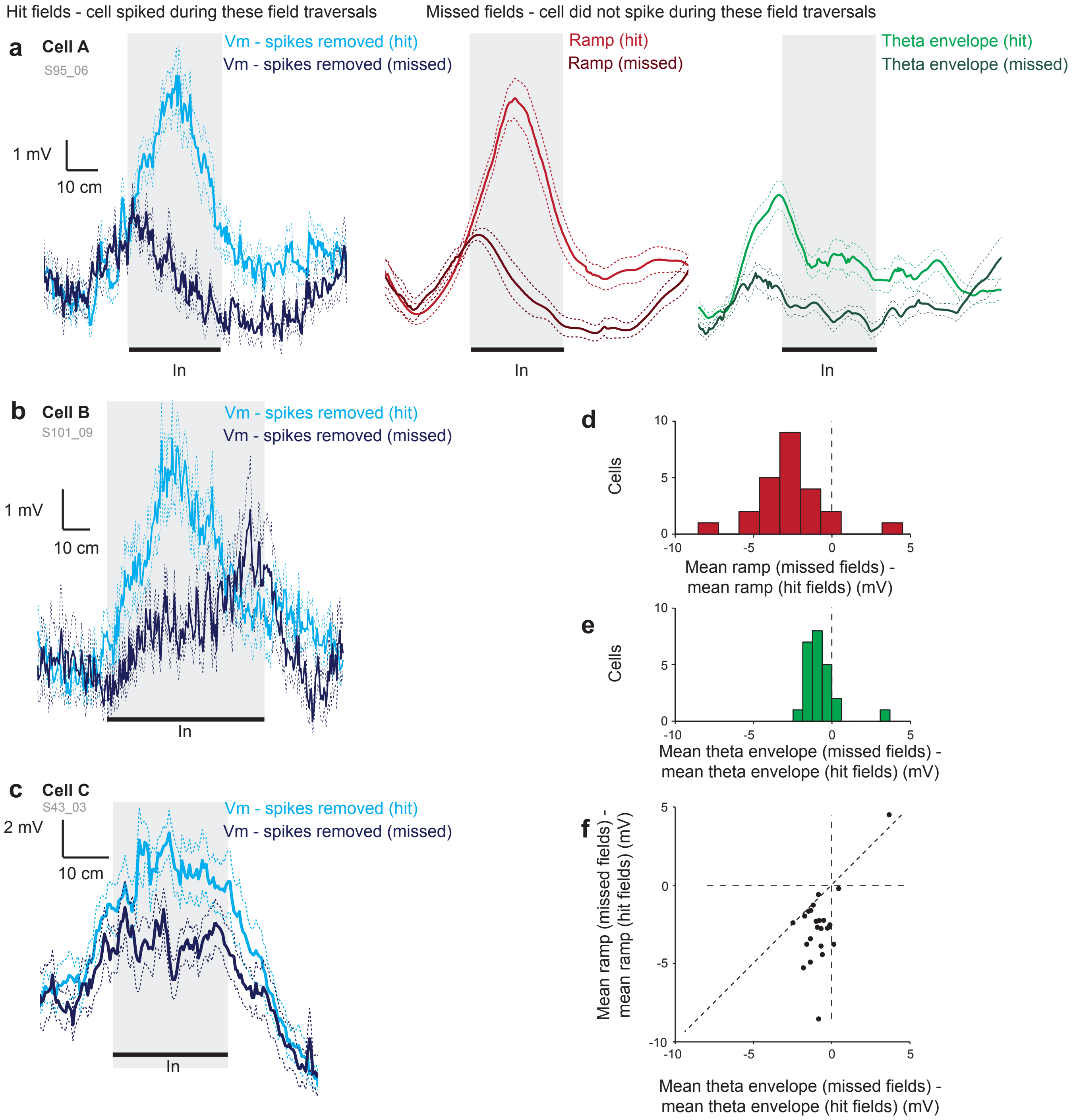

**Supplementary Figure 22 | Missed fields have greatly reduced ramps and more weakly reduced theta amplitudes.** When grid cells do not fire during a field traversal (a 'missed' field), ramps and theta are still present but their amplitude is reduced compared to traversals of the same field when spikes are fired (a 'hit' field). Ramp amplitude is more greatly reduced than theta amplitude. **a,** Left: average membrane potential of a grid cell during traversals of one of its fields (labeled 'In') when the cell hit (light blue) or missed (dark blue) the field (dashed lines indicate ± s.e.m). During both hit and missed fields, the average ramp increased as the mouse approached the field, but during missed fields the membrane potential did not reach the same level of depolarization. Middle, red: average ramp when the same field was hit and missed. Right, green:, average theta envelope when the field was hit and missed. **b,c**, Two additional examples of hit and missed fields from two different grid cells. Note again that a subthreshold depolarization is present during missed fields. **d,e,** Average drop in ramp (red) and theta envelope (green) during missed vs. hit fields for all grid cells recorded (n = 27). Both ramps and theta envelope are reduced during missed fields, with ramps being more greatly reduced. **f,** Average drop in ramp vs. average drop in theta when comparing missed to hit fields.

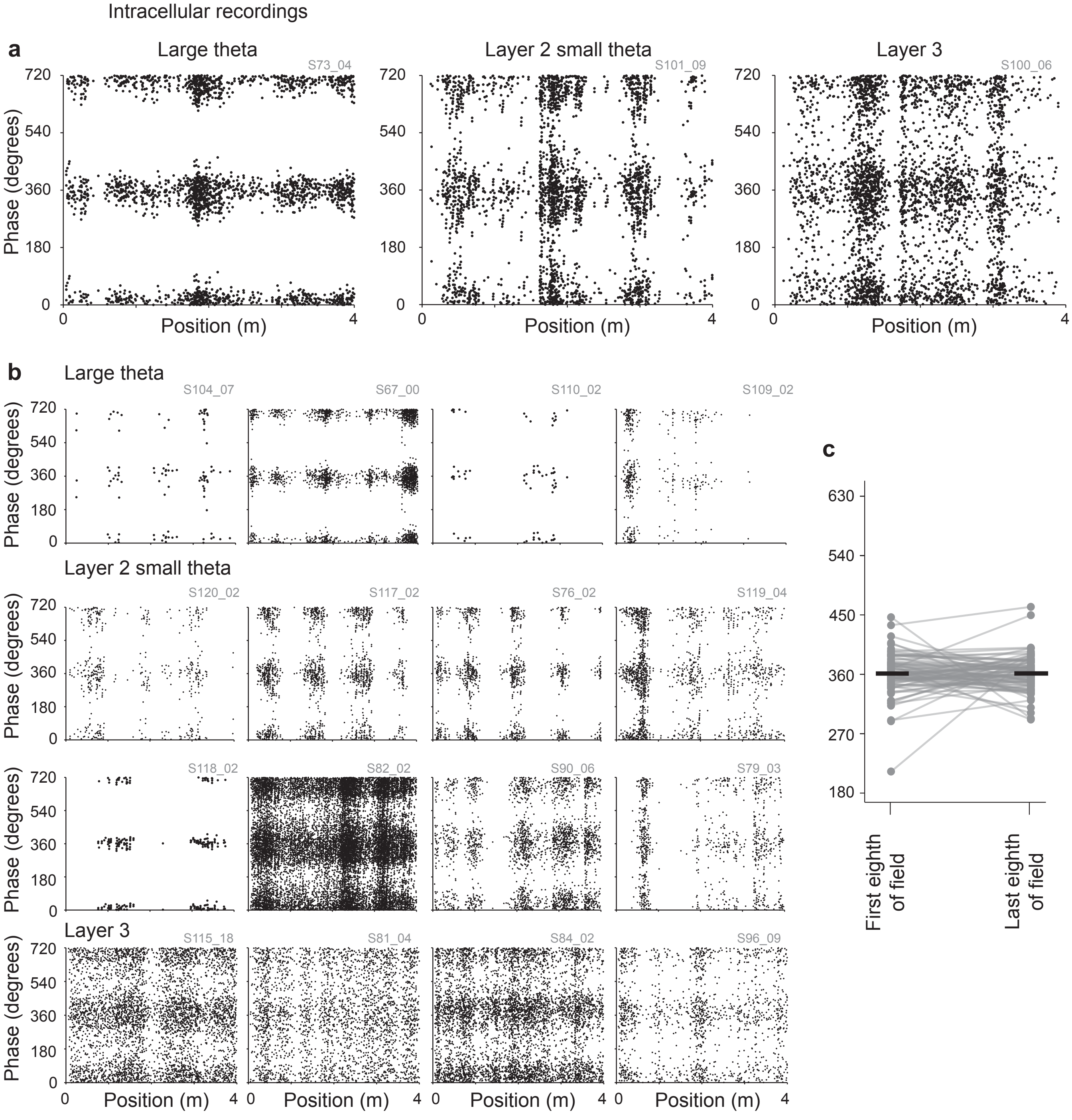

**Supplementary Figure 23 - part 1 | Phase of spiking in grid cells does not precess with respect to intracellular theta oscillations. a,** Three examples of spike phase (two cycles) vs. position for a large theta cell (left), a layer 2 small theta cell (middle) and a layer 3 grid cell. **b,** Additional examples of spike phase vs. position. **c,** Mean phase of spikes fired in the first eighth of each field and mean phase of spikes fired in the last eighth (Methods; each pair of points represents one field; n = 77 fields from 27 grid cells in 24 mice). Horizontal (black) lines are the means. The phase did not decrease significantly between the first and last eighth of each field (mean ∆phase = phase(first eighth) - phase(last eighth) = -1.1 ± 43.2°, t(76) = 0.22, p > 0.8, one-tailed *t*-test). In addition, spike phase and position were not negatively correlated (mean r = -0.008 ± 0.07, t(76) = 1.0, p > 0.1, one-tailed *t*-test) and the slope of phase vs. position was not negative (mean slope = 0.0003 ± 0.5 °/cm, t(76) = 0.08, p > 0.4, one-tailed *t*-test).

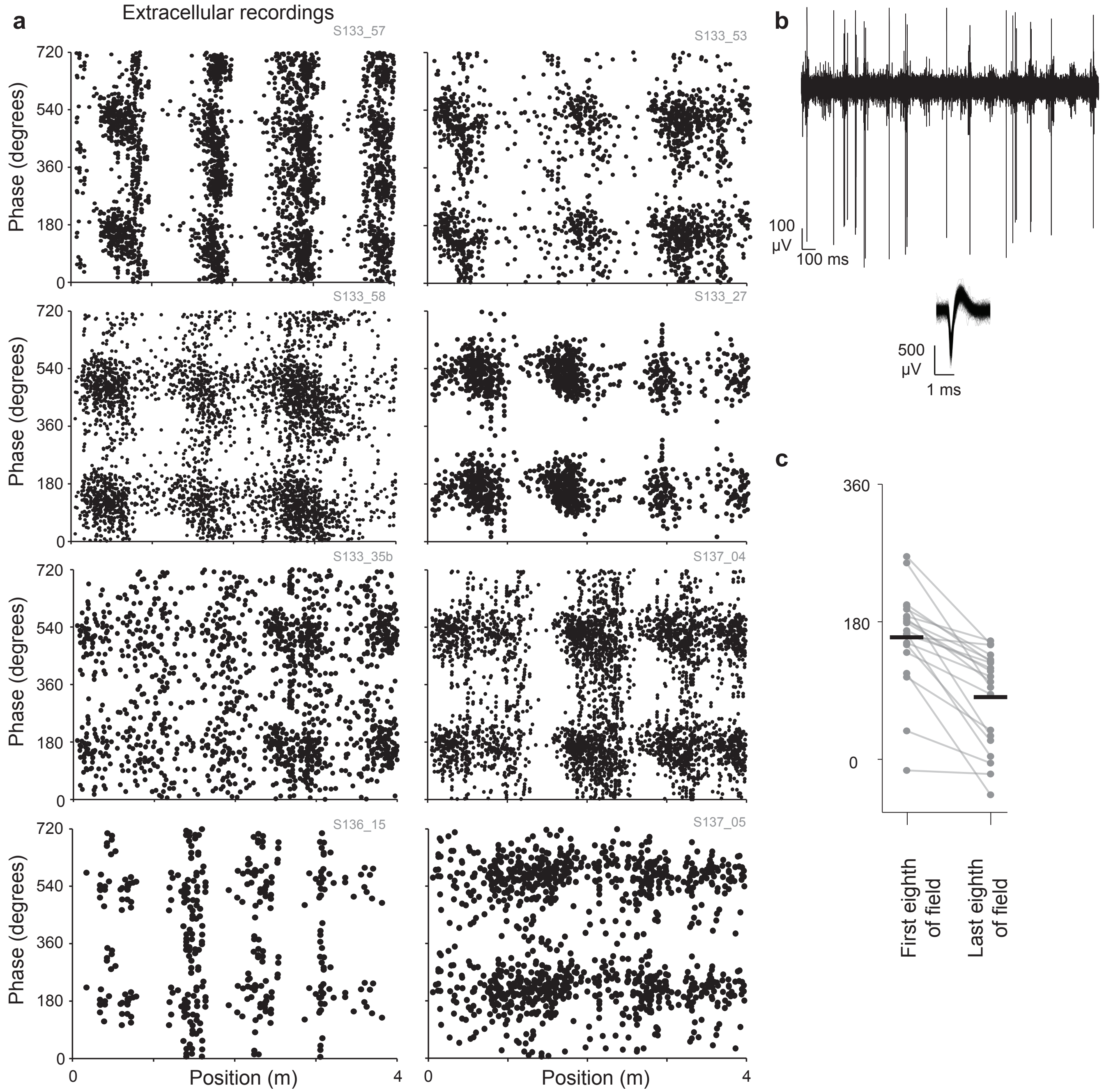

**Supplementary Figure 23 - part 2 | Phase of spiking precessed with respect to LFP theta oscillations in the majority of layer 2 grid cells recorded extracellularly. a,** Spike phase vs. position for eight grid cells recorded extracellularly in layer 2 of MEC. 7/8 grid cells showed phase precession (at least one field had a negative slope between phase and position). One grid cell (bottom right) did not exhibit phase precession. **b,** An example extracellular recording filtered between 500 Hz and 10 kHz (top) and overlaid waveforms (inset). **c,** Mean phase of spikes fired in the first eighth of each field and mean phase of spikes fired in the last eighth (each pair of points represents one field; n = 20 fields from the 7 grid cells showing phase precession from 3 mice). Horizontal (black) lines are the means. In the 7 cells showing phase precession, the phase decreased significantly between the first and last eighth of each field (mean Δphase = 76.2 ± 50.5°, t(19) = 6.7, $p < 10^{-5}$, one-tailed *t*-test). In addition, spike phase and position were negatively correlated (r = - 0.21 ± 0.09, t(19) = 10.5, $p < 10^{-9}$, one-tailed *t*-test), and the mean slope of the line of best fit was negative (slope = -1.11 ± 0.8°/cm, t(19) = 6.4, $p < 10^{-5}$, one-tailed *t*-test). If the 8th cell is included in these analyses, the results do not change qualitatively (mean Δ phase = 64.2 ± 61.5°, t(21) = 4.9, $p < 10^{-4}$; mean Pearson's correlation coefficient r = - 0.17 ± 0.14, t(21) = 5.9, $p < 10^{-5}$; mean slope = - 0.97 ± 0.87, t(21) = 5.6, $p < 10^{-4}$; all one-tailed *t*-tests).

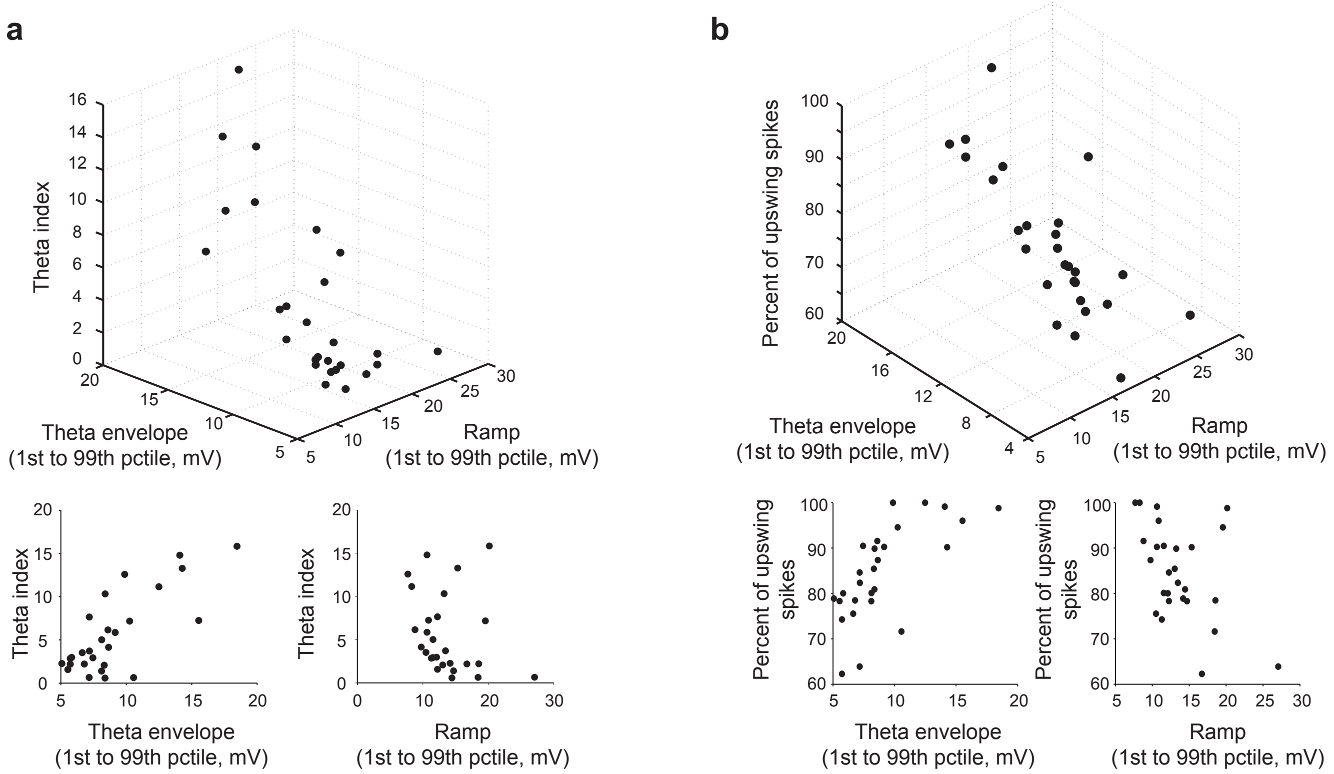

**c**

**Both:** $M = \beta_0 + \beta_R R + \beta_T T + \varepsilon$ **T alone:** $M = \beta_0 + \beta_T T + \varepsilon$ **R alone:** $M = \beta_0 + \beta_R R + \varepsilon$

M: theta modulation of spiking; R: ramp amplitude; T: theta envelope; $\beta_0$ ,$\beta_R$, $\beta_T$: fitted coefficients; ε: error term

**d**

| Regression variables | | | Regression results | | | | | | |
|---|---|---|---|---|---|---|---|---|---|
| **Ramp amplitude (R)** | **Theta envelope (T)** | **Theta modulation (M)** | **T alone** | **R alone** | **Both** | | | | |
| | | | **$R^2$** | **$R^2$** | **$R^2$** | **$\beta_T$** | | **$\beta_R$** | |
| 1st-99th pctile | 1st-99th pctile | theta index | 0.58 | 0.05 | 0.65 | 1.07 | $p < 10^{-5}$ | -0.3 | $p < 0.05$ |
| 10th-90th pctile | 10th-90th pctile | theta index | 0.57 | 0.01 | 0.61 | 1.70 | $p < 10^{-5}$ | -0.4 | $p = 0.11$ |
| 25th-75th pctile | 25th-75th pctile | theta index | 0.55 | 0.00 | 0.57 | 3.05 | $p < 10^{-5}$ | -0.4 | $p = 0.33$ |
| 1st-99th pctile | 1st-99th pctile | % upswing spikes | 0.46 | 0.22 | 0.71 | 4.37 | $p < 10^{-5}$ | -1.2 | $p < 10^{-3}$ |
| 10th-90th pctile | 10th-90th pctile | % upswing spikes | 0.45 | 0.08 | 0.59 | 7.1 | $p < 10^{-4}$ | -1.6 | $p < 0.01$ |
| 25th-75th pctile | 25th-75th pctile | % upswing spikes | 0.44 | 0.06 | 0.54 | 12.8 | $p < 10^{-4}$ | -2.35 | $p < 0.05$ |

**Supplementary Figure 24 | Relationship between ramp and theta amplitude and theta modulation of spike timing. a,** Top: theta index of 27 grid cells as a function of the range of theta envelope and ramp amplitudes in each cell (defined as the difference between the 99th and 1st percentile of theta envelope and ramp respectively). Bottom: two - dimensional projections along theta envelope and ramp axes. **b,** Percent of 'upswing' spikes (defined as the percent of spikes occurring in the 180° around a theta peak), plotted as in (a). Note that in both (a) and (b), the theta index or percent of upswing spikes increases as theta envelope increases; in contrast, these measures of theta modulation of spiking decrease as ramps increase. **c,** Linear regression equations used to estimate 'M', a variable indicating the degree of theta modulation, as a linear combination of 'R' and 'T', variables indicating the amplitude of ramps and theta envelope respectively ('Both'), or to estimate 'M' in terms of 'R' or 'T' alone. **d,** Results of linear regression analyses for three methods of defining 'R' and 'T', as the distance between the 1st and 99th, 10th and 90th, and 25th and 75th percentiles of each distribution, respectively, and for two methods of defining the theta modulation 'M', using the theta index and the percent of upswing spikes. When both 'R' and 'T' were used, the value of $\beta_T$ was always positive and significantly different from zero (partial F statistic), indicating that a higher theta envelope corresponded to greater theta modulation; the value of $\beta_R$ was always negative (but not always significantly different from zero, partial F statistic), indicating that a higher ramp tended to correspond to a smaller degree of theta modulation. Whether the coefficient for the ramp was significant depended on the definitions used, as shown by the different p values for the fit of $\beta_R$ .

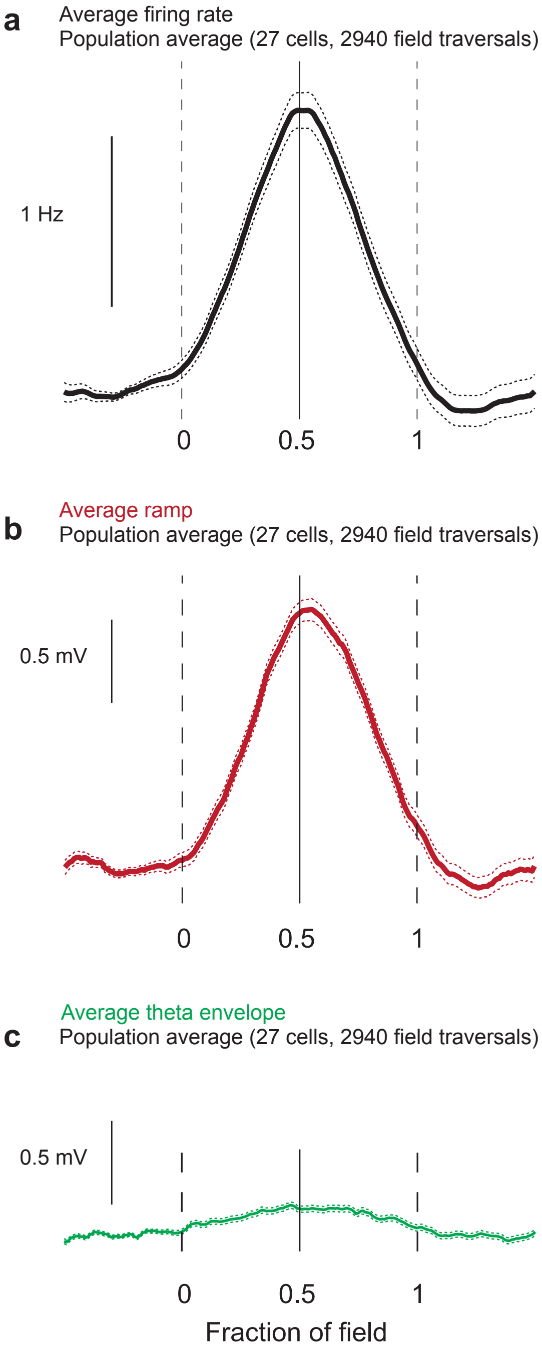

**Supplementary Figure 25 | The firing rate, ramp, and theta envelope reach a peak near the center of grid fields. a,** Average firing rate for all field traversals of all grid cells (dashed lines indicate +/- s.e.m). The solid black line at 0.5 indicates the center of the field. All field widths are normalized to the 0 - 1 range (beginning and end of the field are indicated with dashed black lines). The firing rate peaks at 51.8 ± 22.1 % of the field. **b,** Average ramp for all field traversals of all grid cells (n = 27 cells, 2940 field traversals). The ramp peaks at 53.8 ± 22.3 % of the field. The average ramp is smaller than typical individual ramps, which is likely due to variability in the position of the ramp peaks during individual field traversals. The same is true for the firing rate and theta envelope. **c,** Average theta envelope for all field traversals of all grid cells (b and c have the same vertical scale for comparison of the ramp and theta envelope). The theta envelope peaks at 50.7 ± 25.0 % of the field. The firing rate and ramp peaks are slightly after the center of the field (one-tailed t-tests vs. 50 %, $p<10^{-3}$). The position of the theta envelope peak is not statistically different from 50 % (two-tailed t-test vs. 50 %, $p > 0.05$). The same results were obtained when large theta, layer 2 small theta, or layer 3 cells were considered separately.

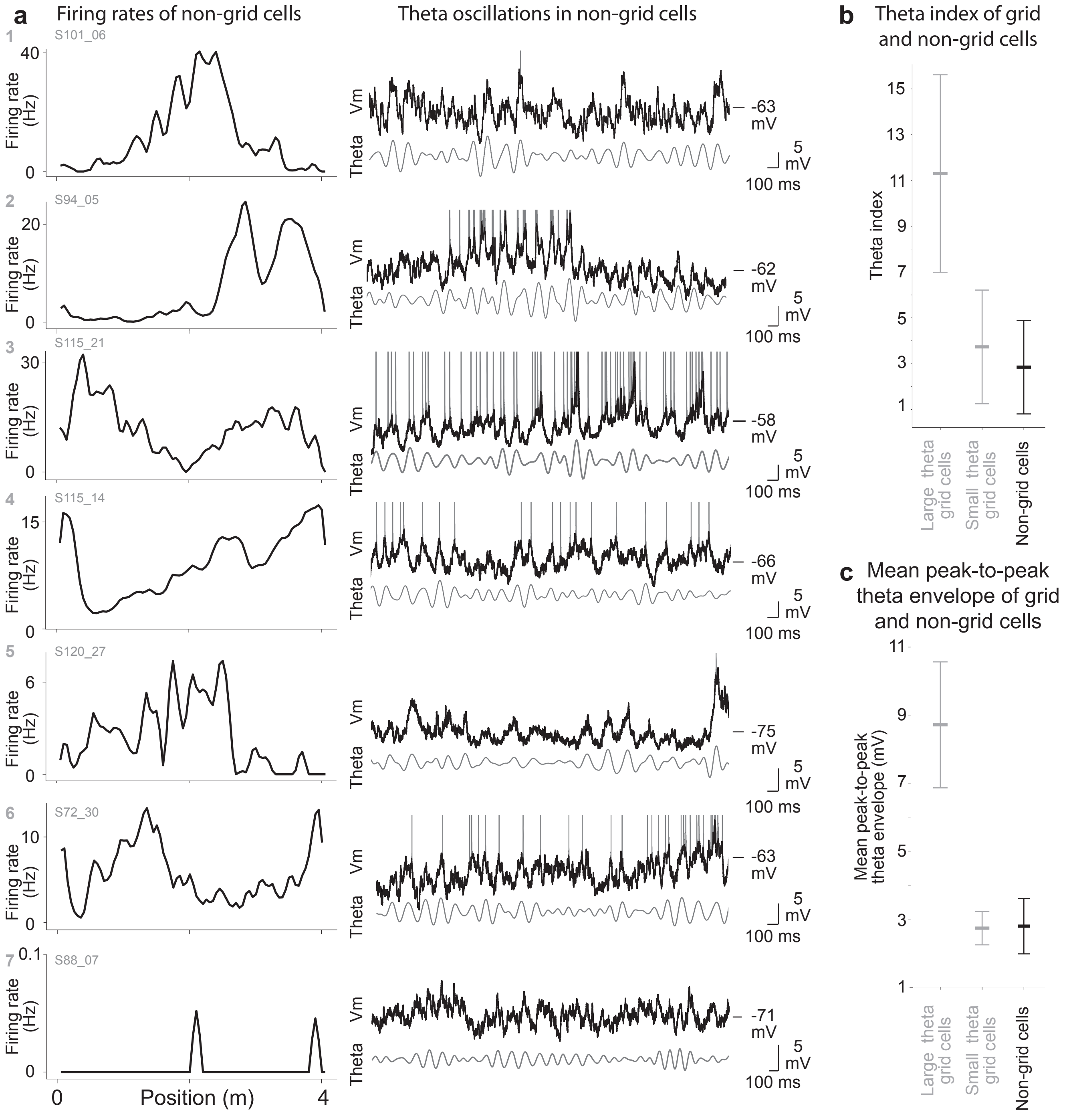

**Supplementary Figure 26 part 1| Intracellular theta oscillations are present in non-grid cells**. **a,** Left, firing rates of the seven cells identified as non-grid cells (Methods). Right, portions of each recording exhibiting membrane potential theta oscillations. Each trace includes the membrane potential (black), truncated spikes (grey) and the corresponding theta oscillation underneath (grey). **b,** The average theta index was not significantly different between small theta grid cells and non-grid cells, but it was significantly different between large theta grid cells and non-grid cells (large theta grid cells: 11.3 ± 4.3 (n = 5); small theta grid cells: 3.7 ± 2.5 (n = 22); non-grid cells = 2.8 ± 2.0 (n = 7); One-way ANOVA, F(2,32) = 103, $p < 10^{-14}$; post-hoc Tukey HSD tests: large theta vs. non grid, $p < 10^{-4}$; small theta vs. non grid, p > 0.7). Large and small theta grid cells were analyzed separately because this set of non-grid cells did not contain any large theta cells; however, the sample sizes were small, and it is possible that large theta non-grid cells exist. In this dataset of 6 large theta cells, 5 were grid cells; the 6th was not, but it also did not fulfill the criteria for being a clear non-grid cell (Methods). **c,** The mean peak-to-peak theta envelope during running was not significantly different between small theta grid cells and non-grid cells but it was significantly different between large theta grid cells and non-grid cells (large theta grid cells: 8.7 ± 1.9 mV (n = 5); small theta grid cells: 2.7 ± 0.5 mV (n = 22); non-grid cells: 2.8 ± 0.8 mV (n = 7); One-way ANOVA, F(2,31) = 17.8, $p < 10^{-5}$; post-hoc Tukey HSD tests: large theta vs. non grid, $p < 10^{-11}$; small theta vs. non grid, p > 0.9). These results indicate that non-grid cells were as theta modulated as small theta grid cells and they had membrane potential oscillations of similar amplitude.

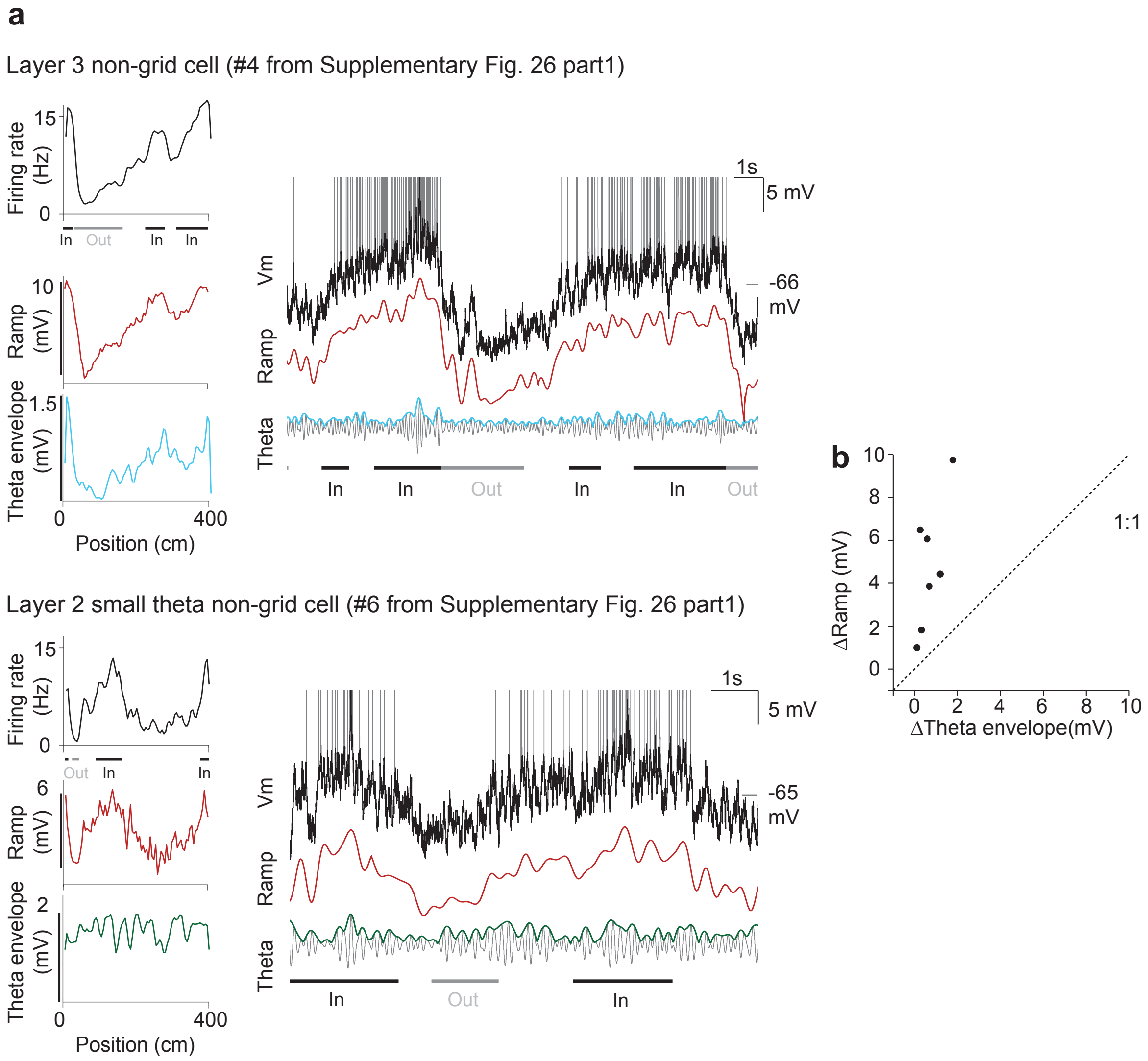
Layer 3 non-grid cell (#4 from Supplementary Fig. 26 part1)

Layer 2 small theta non-grid cell (#6 from Supplementary Fig. 26 part1)

**Supplementary Figure 26 part 2 | Spatial firing fields of non-grid cells are accompanied by increased ramp and theta oscillation amplitudes**. Six of the seven non-grid cells from part 1 had both field and out-of-field periods, defined as they were for grid cells (cell #7 did not spike on a sufficient fraction of runs and therefore had no firing fields). We analyzed whether non-grid cells exhibited increases in ramps and theta oscillations in their firing fields. **a,** Two example non-grid cells. Top: layer 3; Bottom: layer 2. Left: firing rate (in- and out-of-field periods indicated underneath), ramp (red), and theta envelope with respect to position along the track (blue or green). Right: membrane potential during firing field traversals, and its decomposition into the ramp (red) and theta component (grey, envelope in blue or green). Note the presence of slow ramps of depolarization underlying firing fields in non-grid cells. **b,** ΔRamp vs ΔTheta envelope in the seven non-grid cells (Methods). As in grid cells, both ramps and theta envelope increased in firing fields of non-grid cells (the mean ΔRamp and ΔTheta envelope were both significantly higher than 0; ΔRamp, $t(6) = 4.2$, $p < 0.01$; ΔTheta envelope, $t(6) = 3.1$, $p < 0.05$, one-tailed t-tests). As in grid cells, the increase in ramp in a cell was significantly higher than the increase in theta envelope ($t(6) = 4.2$, $p < 0.01$, paired t-test, ). For non-grid cells ($n = 7$), the mean ± s.e.m ΔRamp = 4.7 ± 1.1 mV whereas for grid cells the ΔRamp = 2.9 ± 0.3 mV (the means were significantly different, $t(32) = 2.42$, $p < 0.05$, t-test). However, the increase in theta envelope was not significantly different between grid and non grid cells (mean ± s.e.m. ΔTheta envelope: non grid cells, 0.70 ± 0.23 mV; grid cells, 0.72 ± 0.12 mV, $t(32) = 0.05$, $p > 0.9$, t-test).

**a** Layer 3

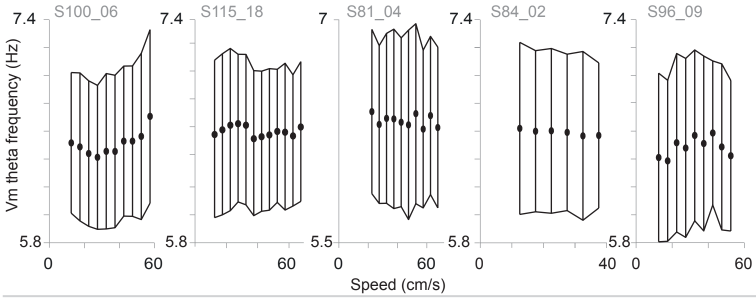

**b** Large theta

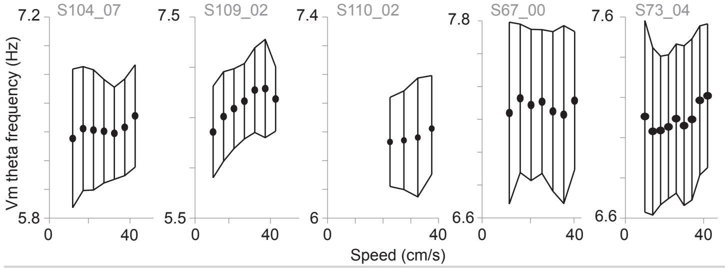

**c** Layer 2 small theta

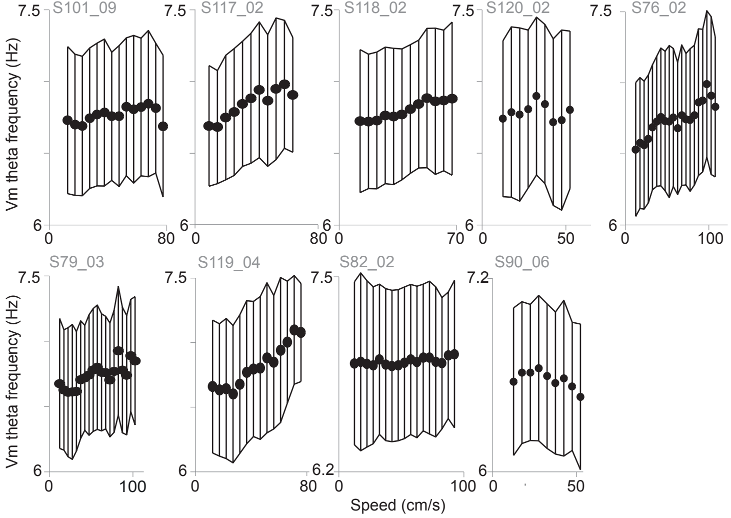

**d** LFP theta frequency vs. speed - Jeewajee et al. 2008

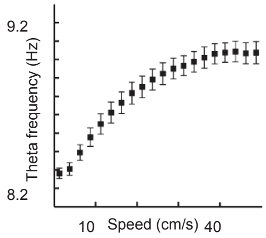

**Supplementary Figure 27 | Relationship between theta frequency and running speed. a-c,** Left: Vm theta frequency vs. speed relationship for layer 3, large theta, and layer 2 small theta grid cells (black, dots indicate mean, lines indicate ± std). Note that the membrane potential theta frequency increases with speed in a subset of cells; the standard deviation is large in all cells. **d,** LFP theta frequency vs. speed (reproduced from Jeewajee et. al 2008).

## Methods

All procedures were approved by the Princeton University Institutional Animal Care and Use Committee and were in compliance with the Guide for the Care and Use of Laboratory Animals (http://www.nap.edu/readingroom/books/labrats/). Male C57BL/6J mice (Jackson Labs) were used for all experiments because of their good vision[39] and because they have been trained successfully to navigate in virtual linear tracks[29,30] and T-mazes[40]. For whole-cell recordings, mice were aged 8-12 weeks; for tetrode experiments they were aged 6-12 months. All surgeries described were performed under isoflurane anesthesia. All analysis was performed using custom-written software in Matlab (Mathworks) unless otherwise noted. Correlation coefficients are from Pearson's correlation, p values reflect unpaired two-tailed Student's t-tests, and data are presented as the mean ± standard deviation unless otherwise noted.

## Cell names

Whole-cell, extracellular recordings: Mice are labeled as 'S(mouse#)_(cell#)'. The only two grid cells recorded in the same mouse and session are S115_24 and S115_30. Tetrode recordings: Cells are labeled at 'T(mouse#)_(year, month, day)_t(tetrode#)_c(cluster#)'.

## Virtual-reality set-up

The virtual reality system was adapted from that described previously (Supplementary Fig. 2)[29]. Grid cells are normally recorded in real 2D arenas; however, the amount of time required to explore 2D arenas is longer (~20 minutes) than many currently obtainable whole-cell recordings from grid cells (e.g., ~10 minutes). We therefore recorded grid cells on linear tracks, which offer a large advantage in terms of the number of field traversals that can be obtained in a short recording. Briefly, head restrained mice ran on the upper surface of a custom Styrofoam cylindrical treadmill, rotating with an axle supported by 1/4' pillow block air linear bearings (New Way S300601)[38]. Treadmills were ~7.5-10 cm wide and ~10-12 cm in radius. A digital light processing projector (Mitsubishi HD 4000 or HC 3000) was used to project a visual virtual environment onto a toroidal screen via an angular amplification mirror[28,29,41]. Rotations of the cylindrical treadmill were measured by a precision angular encoder (US digital) and linearly mapped onto forward movement in the virtual environment. For a small subset of whole-cell recordings, mice ran on a spherical treadmill (8-inch diameter Styrofoam ball; Floracraft)[42]. In these experiments, treadmill rotation was measured by a Logitech MX518 optical computer mouse positioned on the ball's equator, and the rotational speed along the mouse's body axis was used to control forward movement in the virtual environment. For both cylindrical and spherical treadmill configurations, forward movement of the mouse on the treadmill was translated into an equal distance travelled in the virtual environment. The length of the linear track was calculated as the circumference of the treadmill times the number of turns required to traverse a linear track. Liquid rewards used for operant conditioning were delivered through a lick tube (Popper and Sons) positioned in front of the mouse's mouth. Reward amounts were controlled by the opening duration of a solenoid valve (NResearch). Mice used for whole-cell recordings received water rewards; mice used for tetrode recordings in VR received chocolate milk rewards. The VR software was based on modifications to the Quake2 game engine (id software). Virtual environments were designed in Quark (http://quark.planetquake.gamespy.com). Grid cell activity is directionally selective on linear tracks, such that the locations where the cell fires differ between the forward running direction (from beginning towards end) and backward running direction (from end towards beginning); as a result, on linear tracks grid cell firing is normally considered separately in each direction such that each cell yields two separate data sets, each comprising one half of the recording time[20,31]. To maximize the number of runs through a cell's firing fields given the time constraints imposed by whole-cell recordings, we took advantage of the flexibility of virtual reality and used a unidirectional linear track: the mouse was transported ('teleported') back to the beginning of the track once it reached the end, such that all runs were in the forward direction only[38]. The beginning portion of the track had dark walls to provide visual continuity with the end of the track. Using this virtual environment, each run through the track resulted in firing at the same set of locations in space. These locations differed between cells.

### Tetrode recordings

To determine whether grid cells had properties in VR similar to those in real environments, we developed a custom tetrode assembly and headplate for mice that was compatible with behavior in both real and virtual environments. We used this system to sequentially record from the same grid cells in both a real arena and a virtual linear track.

### Tetrode - microdrives

Microdrive assemblies were based on a previous design for use with rats[43,44], but modified to accommodate bilaterally positioned tetrodes. The microdrive was also scaled down in size and weight for use with mice. The drive consisted of 4 independently movable tetrodes arranged as two pairs of tetrodes lowered through two cannulas positioned bilaterally 6.2 mm apart. Components of the drive were designed using Autodesk Inventor and printed with stereolithography (American Precision Prototyping) using the Acura Xtreme material. Individual screw-driven micro-drives for each tetrode were made as described previously[43]. Tetrodes were connected with gold pins to an electrode interface board (EIB18, Neuralynx). Drives were electrically shielded with a grounded foil covering the outer surface of a protective cone that surrounded the drive assembly. A stainless steel screw above the cerebellum was used as reference ground.

### Tetrode - surgery

To allow head-fixation in virtual reality, a headplate similar in size to those used previously[29] was affixed to the skull using dental cement (Metabond, Parkell Inc.); bilateral craniotomies were performed using stereotaxic coordinates (3.1 mm lateral of the midline and on the lambdoid suture). A microdrive assembly was then positioned above the skull with the upper end of the assembly tilted 18 degrees rostral from vertical. The drive assembly was then lowered until the lower ends of the bilateral cannula were positioned just above the dura (~100-300 μm above the dura). The area between each craniotomy and cannula was sealed with Dentin (Parkell Inc.). The microdrive assembly was then attached to both the skull and the headplate with Metabond (Parkell Inc.). When the Metabond solidified, all 4 tetrodes were slowly lowered down to 1 mm past the bottom of the cannula.

### Tetrode – behavioral training:

At least one week after they recovered from surgery, mice were trained to forage for chocolate crumbs in a real 0.5 x 0.5 m wide box, with 0.28 m tall black walls, in 10 – 20 minute sessions (2D arena). After each session, mice were immediately transferred to an adjacent virtual reality setup and trained for 45 minutes to run for chocolate milk rewards on a 1D treadmill along a virtual linear track.

### Tetrode - recordings

Grid cell recordings were performed after the animal had been trained for at least one week in both the 2D arena and the virtual 1D track. Tetrodes were slowly lowered until theta frequency oscillations appeared in the LFP during running and units became theta-modulated. Recordings were performed using a Digital Lynx SX acquisition system (Neuralynx). Two LEDs (red and blue) on the headstage (HS-18, Neuralynx) were used to detect the position of the mouse using the Neuralynx digital tracking system during navigation in the 2D arena. Cheetah acquisition software was used for recording tetrode signals, sampled at 32 kHz and bandpass filtered from 500 – 7500 Hz. To synchronize virtual reality parameters with electrophysiology, virtual reality positions, reward times, and angular encoder signals were output from the Quake program as a series of digital words at each frame update, which were recorded as timestamped hexadecimal events on the acquisition computer running Cheetah.

### Tetrode - data analysis

Data analysis was performed offline using a custom Matlab cluster cutting program. Positive and negative thresholds were first used to detect spike events. Clusters were cut manually using the first two principal components of the waveform for each electrode separately[45] as well as the amplitude of the peak, aligned to occur at the 8th sample of 32 samples comprising the waveform. Units were rejected if more than ½ % of the interspike intervals were considered to be in violation of the refractory period (less than 1 ms). A spike timing cross-correlation-based-method was used to identify whether two simultaneously recorded units were from the same cell (which could be caused either by the redundancy of positive and negative thresholds or by the acquisition of a single cell's activity from different locations of the cell). When two units were from the same cell, only the unit with the largest number of spikes was retained to avoid losing spikes belonging to a unit. We calculated a grid score for all recorded units (see below). After the first cell with a gridness score of 0.33 or greater was recorded on a tetrode, all units recorded on that tetrode on the same and subsequent days were included for analysis (the threshold 0.33 was chosen because it is approximately equal to the threshold for being considered a grid cell, see below). The resulting dataset contained 46 single units recorded in both 2D and 1D environments from one mouse, 31 of which were grid cells.

### 1D Mouse running speed

The speed of the mouse in 1D was measured from its position in the virtual environment, smoothed with a 1 second uniform sliding window for tetrode recordings and a 100 ms uniform sliding window for whole-cell and extracellular recordings. Unless otherwise indicated, time points during which the mouse ran slower than 1 cm/s were considered stationary and removed from analysis. This speed threshold (1 cm/s) was chosen based on a histogram of the running speeds of all mice used for whole-cell recordings.

### 1D Firing rate maps

To calculate the firing rate as a function of position along the virtual linear track, we divided tracks into non-overlapping 5-cm bins. The firing rate was defined as the number of spikes fired within a bin divided by the number of seconds spent in that bin. Firing rates are for running periods only (speed > 1cm/s). Firing rates were smoothed using a 3-point Gaussian window with a standard deviation of one.

### Relation between running speed and firing rate

To determine whether there was a relationship between running speed and firing rate, we used the method from Sargolini et al. 2006. For each cell, we divided the entire recording duration into non-overlapping one second intervals and computed the firing rate and the average running speed during that second. Each such second-long epoch forms one data point (an example is shown in Supplementary Fig. 7, plotted in a similar way to Sargolini et al. 2006, their Fig. 4A). We then calculated the slope of a linear regression between speed and firing rate, as well as the Pearson's correlation coefficient between speed and firing rate. Datasets: four separate datasets were included in this analysis. Two datasets were from tetrode recordings in rats running in real 1D tracks (data from Brun et al. 2008 and Hafting et al. 2008); two datasets were from tetrode and whole-cell recordings we obtained in mice running in virtual 1D tracks. Exclusion criteria: in Supplementary Fig. 7 we show that the fraction of whole-cell recorded grid cells with a positive speed-firing rate relation increases as the number of environment traversals increases (Supplementary Fig. 7b, left); similarly, the fraction of grid cells with a positive speed-firing rate relation increases as the number of spikes contained in the recording increases (Supplementary Fig. 7b, right). Because this method of measuring the relation between speed and firing rate is sensitive to having a sufficient number of spikes in the recording, and because whole-cell recordings contained fewer spikes than the other three datasets, from each data set we considered only those recordings with more spikes than the median number of spikes in whole-cell recordings (1267 spikes). The peak firing rates of whole-cell recorded grid cells with above-median and below-median numbers of spikes were not statistically different ($p > 0.3$, *t*-test).

### Estimating the firing rate versus position on individual runs

To calculate the Pearson's correlation coefficient between the ramp and firing rate on a run-by-run basis, we estimated the time-varying firing rate rather than counting spikes in spatial bins as described above to avoid noise caused by small numbers of spikes. The time-varying firing rate was estimated by convolving the spike train with a Gaussian kernel with a standard deviation of 0.5 seconds. The mean firing rate as a function of position was produced by averaging this estimated firing rate across all time bins corresponding to positions within a spatial bin.

### 1D - Detecting fields and out-of-field periods (illustrated in Supplementary Fig. 5)

Grid cells on linear tracks exhibit multiple firing fields separated by out-of-field periods of lower firing rate (e.g. Fig. 2, Supplementary Fig. 6a-b)[1,20,31]. To identify the position of in-field and out-of-field periods, we looked for bins where the cell fired at a much higher (in-field) or much lower (out-of-field) rate than would be expected by chance for that cell and that bin (Supplementary Fig. 5). Only recordings that included 3 or more complete runs through the virtual environment were considered. For each 5 cm bin, we calculated a bootstrapped shuffle distribution of the firing rate by rotating the spikes of the entire recording and, for every rotation, calculating a new firing rate based on the new spike positions and the original dwell times for that bin. Spike indices were rotated 1000 times by an integer number of samples drawn randomly from the interval $0.05 \times N_{samples}$ to $0.95 \times N_{samples}$, where $N_{samples}$ is the number of samples in the recording (Supplementary Fig. 5a-d). For each position (each 5 cm bin), we defined a $P_{value}$ equal to the percent of shuffled firing rates that were higher than the cell's real firing rate for that bin. Equivalently, $1 - P_{value}$ was equal to the percent of shuffled firing rates lower than the cell's real firing rate.

Out-of-field periods were defined as two or more adjacent bins for which the real firing rate was lower than the 5th percentile of the bootstrapped shuffle distribution for that bin ($1 - P_{value} \leq 0.05$); an example is shown in Supplementary Fig. 5c-f (Position 2). To define firing fields, we first defined candidate firing fields as groups of three or more bins (except at the beginning and end of the track where two adjacent bins were sufficient) whose firing rate was higher than the 85th percentile of the bootstrapped shuffle distribution for that bin ($1 - P_{value} \geq 0.85$). Candidate firing fields were extended, by no more than one bin to the left and right, if those adjacent bins had firing rates that exceeded the 70th percentile of the bootstrapped shuffle distribution ($1 - P_{value} \geq 0.70$). Firing fields were defined as candidate fields with spikes on at least 20% of all runs. This procedure identified both firing fields and out-of-field periods, but bins with intermediate firing rates remained unassigned (Supplementary Fig. 5f,g).

### 1D - Field width and spacing

To calculate the field width (Supplementary Fig. 6), we multiplied the number of bins in each detected field by the bin width (5 cm). To calculate field spacing, the 1D firing rate was smoothed with a uniform 5-bin window and the minimum firing rate was subtracted. We calculated the autocorrelation function of this smoothed, baseline-subtracted firing rate (using xcorr in Matlab), and measured the distance between the peak at 0 and the first local maximum in the autocorrelation function. This autocorrelation-based method for measuring field spacing therefore took into account the entire firing rate and did not depend on the exact boundaries of field and out-of-field periods.

### 2D - firing rate maps

The two dimensional firing rate was evaluated for all cells that fired at least 100 spikes in the real environment. To estimate the firing rate as a function of position in the real, 2D arena, the position of the mouse was measured every ~30 ms with LEDs. The x and y position signals were each smoothed with a 450 ms uniform window; the instantaneous speed was then calculated and portions where the mouse ran slower than 1 cm/s were removed from analysis; this speed threshold was chosen to match that used for 1D virtual tracks. Mouse position was binned in 1.5 x 1.5 cm bins; data from one recording session were used if the mouse visited 80% or more of the bins, where unvisited bins are those where the mouse spends zero time points. The spike count per bin and the number of seconds spent in every bin were calculated, then each smoothed using a 2x2-bin kernel Gk = [0.5 0.5; 0.5 0.5]. The firing rate $f(x,y)$ was calculated as the ratio between the smoothed spike count and the smoothed number of seconds spent in every bin (here x and y are measured in bins). No additional smoothing was applied. From the 2D firing rate, the spatial autocorrelation $Autoc(\Delta x,\Delta y)$ of the firing rate was calculated as:

$$Autoc(\Delta x,\Delta y)=\frac{n\cdot\sum f(x,y)\cdot f(x-\Delta x,y-\Delta y)-\sum f(x,y)\sum f(x-\Delta x,y-\Delta y)}{\sqrt{n\cdot\sum\left(f(x,y)\right)^2-\left(\sum f(x,y)\right)^2}\cdot\sqrt{n\cdot\sum\left(f(x-\Delta x,y-\Delta y)\right)^2-\left(\sum f(x-\Delta x,y-\Delta y)\right)^2}}$$

where, for every pair of displacements $\Delta x$ and $\Delta y$, $n$ is the number of pairs of bins separated by those displacements such that both $f(x,y)$ and $f(x-\Delta x,y-\Delta y)$ were defined. Here $f(x-\Delta x,y-\Delta y)$ is the firing rate translated by $\Delta x$ and $\Delta y$. For values of $\Delta x$ and $\Delta y$ for which $n < 20$, the autocorrelation function was not calculated[1]. The autocorrelation function ranges between -1 and 1 for all displacements; the value is always 1 at the center of the autocorrelation map because the displacement is 0.

## 2D grid score

To identify grid cells based on recordings in 2D, we defined a standard grid score designed to measure the presence of 60º rotational symmetry expected of an equilateral triangle lattice. The two-dimensional autocorrelation of the firing rate map was calculated for each cell. An annular portion was selected from the autocorrelation map that excluded the central field and included a ring with six fields around the center. The inner and outer radii of the annulus were defined as follows: the inner radius was defined as either the first local minimum of the average autocorrelation vs. distance-from-the-center function, or as the first radius where the correlation was negative, whichever occurred first[46]. If no local minima or negative correlation values were found within 30 cm of the center, the inner radius was set to 10 cm. The outer radius of the annulus was moved in 2.5 cm increments starting from the inner radius plus 10 cm and ending at the outer dimension of the recording box minus 10 cm. Each annulus map was rotated in steps of 30º, and the Pearson's correlation coefficient between the rotated and original annuli was computed for each rotation angle. The grid score for each annulus was defined as:

$$\text{Annulus grid score} = \max(r(0°, 60°), r(0°, 120°)) - \min(r(0°, 30°), r(0°, 90°), r(0°, 150°))$$

Here, $r(x°, y°)$ indicates the Pearson's correlation coefficient between the annulus rotated by x and y degrees respectively. The grid score for the cell was defined as the highest annulus grid score obtained from all annuli (equivalent to 'Method 2' or 'Moving radius' method from Boccara et al. 2010 (their Fig. S6)[47]). The moving radius method produces comparable (although slightly higher) grid scores to the alternative method involving identifying the six peaks around the center, and has the additional advantage that it does not require finding the six peaks in the autocorrelogram which can be difficult for cells lacking clear fields[46,47].

## Grid cell classification based on 2D grid score

Similar to rats, the units recorded with tetrodes had grid scores ranging from ~ - 0.5 to 1.5. A histogram of all grid scores is shown in Supplementary Fig. 4. To determine whether a cell was a grid cell based on its 2D grid score, we rotated the spike times with respect to the position vector by a random time drawn uniformly from the interval between 20 seconds and the recoding duration minus 20 seconds (400 rotations per cell for a total of 46×400 rotations)[46]. For each rotation, the grid score was calculated as described above. This procedure created a baseline distribution of grid scores that would be expected by chance (Supplementary Fig. 4b). The 95th percentile of the baseline distribution defined a threshold ('Gth'); cells whose grid score was greater than or equal to Gth were called grid cells. In this dataset Gth was 0.34 (red line in Supplementary Fig. 4b). This value of Gth is similar to those reported in both rats[46,47] and bats[24]; note that the grid score histogram reflects a bimodal distribution, and Gth separates the two modes (Supplementary Fig. 4a). From the 46 units, the 2D grid score assigned 31 cells (~67%) as grid cells, consistent with previous estimates of grid cell frequency as measured with tetrodes[48]. All cells that were classified as grid cells by this method (grid score >= Gth) had clear hexagonal firing fields when inspected visually; in addition, many other cells which did not pass this criterion also had hexagonal-like firing fields, suggesting that this method of identifying grid cells is conservative.

### Tetrode recordings from the Moser group

To establish that grid-cell firing in virtual linear tracks is comparable to grid-cell firing in real linear tracks, we compared our recordings with data from Brun et al. 2008 (~18m linear track) and Hafting et al. 2008 (~3m linear track). Rat tetrode recordings were shared by the Moser group and downloaded from http://www.ntnu.no/cbm/gridcell. Recordings from VR involved teleportation at the end of the track and were therefore unidirectional, whereas recordings on real linear tracks were bidirectional. To compare the datasets, we split each real linear track recording into a forward and backward running direction. Each direction was treated independently as if it were a separate unit. We measured the running speed of the rat from the provided position signals and removed portions where the running speed was ≤ 1 cm/s. From real linear track recordings, we estimated in-field and out-of-field periods for each cell, as described above. We then measured the mean field width, mean field spacing, and peak in-field firing rate for all grid cells recorded in rats and compared the measurements with those made in mice in virtual linear tracks (Supplementary Fig. 6).

### 2D-1D classifier testing

The 1D classifier was designed to label grid cells and non-grid cells based on 1D data alone. From tetrode recordings, we noted that grid cells exhibit multiple localized firing fields on linear tracks, separated by out-of-field periods. Based on the criteria described above, in-field and out-of-field periods were defined for linear track recordings for each cell. The 1D classifier identified a cell as a grid cell if it had a) at least 3 transitions between a field and an out-of-field period per 4 m of linear track, b) the widest field was < 90 cm, c) 30% or more of the bins were assigned to either in-field or out-of-field periods and d) the mean in-field to mean out-of-field firing rate ratio was greater than 2.

The 1D classifier assigned 30 out of 46 units recorded with tetrodes as grid cells. Their grid scores are shown as tick marks in Supplementary Fig. 8, and as a distribution estimated using a kernel density estimator (Matlab function ksdensity) underneath. Cells identified as grid cells by the 1D classifier can be divided into true positives and false positives: 26/30 (87%) were 'true positives' – real grid cells according to 2D and correctly identified by the 1D classifier; 4/30 (13%) were 'false positives' – cells identified by the 1D classifier as grid cells but whose 2D-derived grid scores were below Gth – and which were therefore not grid cells. This data suggests that the 1D classifier is generally successful at identifying grid cells with a low false positive rate.

## Whole-cell recordings

Mice used for whole-cell recordings were housed individually and were given access to an in-cage running wheel (Fast-Trac and Mouse Igloo, Bio-Serv). To allow mice to be head-fixed in virtual reality, a titanium headplate was attached to their skull. During the headplate surgery, the locations of future craniotomies were marked stereotaxically at 3.1 mm lateral to bregma and bilaterally on the lambdoid suture (~4.3-4.7 mm caudal to bregma). In addition, a small (~100 μm diameter) fiducial mark was placed 1 mm anterior to each craniotomy marking to serve as the center of a reference frame for positioning electrodes precisely during recordings.

In preliminary experiments we determined that obtaining whole-cell recordings from the MEC was more difficult during periods when mice ran versus when they remained stationary but awake. We therefore reasoned that running introduces additional tissue movement beyond that caused by breathing and heart rate. Because the electrode is rigidly positioned with respect to the headplate, any tissue movements must arise from a displacement of the skull and/or brain with respect to the headplate. The skull of 8-12-week male C57Bl6 mice is not rigid; rather, skull plates are flexible and can move with respect to each other: if slight pressure is applied to the intraparietal plate, it deflects with respect to the parietal plate. During running, muscle movements could cause asymmetric movements of skull plates, which could in turn translate to brain motion. To reduce running-induced movement of the underlying brain tissue, we therefore sought to strengthen and stabilize the overlying skull plates. We first found the surface of the skull ~1 mm anterior to lambda with a rounded miniature rod; the rounded tip was then lowered slightly until the skull plates no longer moved with respect to each other in response to slight pressure. The skull plates were then covered with thin, overlapping layers of 3M Vetbond tissue adhesive. This procedure greatly facilitated whole-cell recordings from the MEC, improving both recording frequency and duration. The titanium headplate was attached with dental cement (Metabond, Parkell). Running wheels were not available to the mice while they recovered from surgery. We observed no behavioral or adverse health effects resulting from skull stabilization.

After they recovered completely from surgery, mice were placed on a water schedule in which they were given 1 mL of water per day (including rewards). Mouse weight was monitored daily to ensure it remained above ~ 75-80% of the starting weight. In-cage running wheels were returned. After they recovered from surgery, mice were placed daily in a large communal playpen environment containing enrichment items, including treadmills and hammocks. Mouse interactions were monitored and aggressive mice were removed from the playpen. Mice were housed independently to facilitate precise water delivery.

### Behavioral training

After 5 days of water restriction, mice began daily behavioral training that occurred at approximately the same time each day. During all training sessions, which lasted 45 min-1h, mice were head restrained on the cylindrical treadmill and immersed in the virtual reality environment. Over the course of 5-10 training sessions, mice learned to run on the cylindrical treadmill; they received a 4 μL water reward at a fixed location at the end of the virtual linear track.

### Whole-cell: electrophysiology

After mice ran at least 300 laps in the virtual environment, which required ~5 training sessions, they were selected for whole-cell recordings. Under isoflurane anesthesia, a small craniotomy (~250-400 μm diameter) was made over the lambdoid suture as previously marked. The fiducial mark 1 mm anterior to the craniotomy was clearly visible. Whole-cell recordings began the following day. After the craniotomy surgery and between recording sessions, the craniotomy was covered with silicone elastomer (Kwik-sil, WPI).

Patch electrodes with long tapers were pulled from 1.5 mm OD x 0.89 mm ID borosilicate glass (Warner Instruments), to a ~1 μm tip diameter. For whole-cell recordings, electrodes were filled with internal saline containing (in mM) 135 K-gluconate, 10 HEPES, 10 $Na_2$-phosphocreatine, 4 KCl, 4 MgATP, 0.3 $Na_3$GTP, 0.5% biocytin and 0.5 mM Alexa 594 hydrazide (pH 7.25 with KOH, 285 mOsm, giving a 4 - 4.8 MΩ resistance). A silver reference electrode was placed outside the craniotomy, submerged in extracellular saline containing, (in mM) 150 NaCl, 2.5 KCl, 10 HEPES, pH 7.4. The liquid-liquid junction potential was corrected for throughout.

To target the dorsal ~1/3 of MEC, electrodes were angled at 12-20° from vertical (typically 18° was used), with the tip pointing towards the cerebellum. To minimize vibrations, electrodes were clamped to a rigid rod and metal holder on a Sutter MP285 manipulator, and the pre-amplification headstage was separately mounted and connected to the electrode lumen with a flexible wire. Because the MEC extends dorsoventrally, small anterior-posterior displacements of the craniotomy could result in large differences in the depth at which MEC layers 2 and 3 would be encountered; prior to whole-cell recording, we therefore targeted MEC separately in each mouse using an extracellular electrode filled with 0.5 mM NaCl (~1.8 MΩ). To provide a reference frame that could be used to position subsequent electrodes, the targeting electrode was first centered on the small fiducial mark anterior to the craniotomy. Because of the relatively small size of the fiducial, sequential estimates of its center remained within a ~20 μm radius. We used the seal-test configuration in PClamp (Molecular Devices) to monitor electrode resistance, which was first noted in saline outside the brain. The targeting electrode was lowered through the dura with positive pressure (~3.5 PSI). Contact with and penetration of the dura was noted as a resistance increase followed by a return to baseline. At 400 μm below the dura, the pressure was removed and the targeting electrode was allowed to clog. The electrode was then advanced slowly through tissue under continuous audio monitoring (~2-4 μm/sec). The mouse ran for rewards in virtual reality during the entire targeting process. As the electrode entered MEC, multi-unit activity became theta modulated[49]. Because of the recording geometry, electrodes first entered MEC through layer 3, traversed layer 3, then entered layer 2, and, depending on the depth at which layer 3 was encountered, the expected distance to be travelled to layer 2 could be calculated[50]. The transition to layer 2 was marked by a pronounced increase in synchrony in the multi-unit activity during running: cells fired tightly phase-locked to the underlying theta rhythm, consistent with observations that cells in layer 2 of MEC are more strongly theta-modulated than those in layer 3 in rodents[51]. To confirm positioning in layer 2, the targeting electrode could be advanced an additional ~200 μm, when unit activity stopped abruptly in layer 1. The probe electrode was then slowly retracted, and the depths at which the layers were encountered were confirmed on the return path. When craniotomies were used for multiple days, this procedure was repeated at the beginning of each recording session.

Patch electrodes were lowered to the depth determined by the probe electrode and targeted specifically to either layer 2 or layer 3 of MEC. The tip of each patch electrode was referenced to the center of the skull fiducial only. It was then guided to the same region of the craniotomy (± ~ 50 μm exploration radius used to target adjacent groups of cells) and lowered through the dura with positive, ~3.5 PSI pressure; 400 μm below the dura, the positive pressure was reduced to ~1 PSI; 100 μm before entering MEC, the pressure was lowered to 0.3 PSI. At the beginning of the desired layer, the pressure was set to 0.16-0.18 PSI to search for cells. Whole-cell recordings were initiated using standard procedures[29]. Proximity to a cell was noted as a reproducible resistance increase. Seals were initiated on the third approach. All recordings were performed in current clamp mode. Holding current was only used for two recordings. To improve the probability of filling cells with biocytin, we did not deliberately interrupt recordings.

The membrane potential (Vm) was recorded by a BVC700 amplifier. Vm was filtered with a 500Hz-10kHz bandpass filter by a Brownlee 440 to produce a ‘spike’ signal, which was used for audio monitoring and spike detection. Signals were sampled at 20 kHz and digitized by a Digidata 1440A; they were visualized and stored using PClamp. Electrophysiological signals were sampled and recorded simultaneously with analog signals for the position of the mouse in the virtual environment, rewards, and the angular position of the treadmill. The Styrofoam treadmill was coated daily with benzalkonium chloride (Benz-all) to reduce low frequency noise observed during treadmill rotation[30].

## Histology

To demonstrate that cells were located in MEC and obtain their layer (2 or 3) and cell type, cells were filled with 0.5% biocytin and 0.5 mM Alexa 594; histological sections were made from all mice. Briefly, Alexa 594 allowed the localization of electrode tracts to MEC; biocytin revealed precise soma location and morphology, allowing cell type identification; layers 2 and 3 were revealed by a Nissl stain; the dorsal border of MEC was visualized with antibodies against calbindin or parvalbumin. In the majority of mice, at most one cell was recorded per hemisphere to allow for unambiguous cell identification. In a subset of mice, multiple recordings were obtained from the same hemisphere to demonstrate that large and small theta cells co-occurred in the same mouse. Histological procedures are described in detail below.

Within ~1 hour of the last whole-cell recording, mice were deeply anesthetized with ketamine-xylazine and perfused transcardially, first with ice-cold PBS, then with 4% paraformaldehyde in PBS. The brain was postfixed for 24 hours in 4% paraformaldehyde at 4ºC, then sliced tangentially at 80 μm on a vibrating slicer (Vibratome Model 1500).

To confirm that recordings were from MEC, electrode tracts were first localized based on the Alexa 594 dye expelled from the electrode under slight positive pressure. Electrode tracts were always visible, and were typically present in only one to three 80-μm slices, reflecting the small craniotomies used. All brain slices containing electrode tracts, as well as 3 slices medial and lateral from the recording site, were selected for subsequent histological processing.

To determine whether cells were in layer 2 or 3 of MEC, the layers were distinguished based on a blue fluorescent Nissl stain (Neurotrace, 1:50 vol/vol in 0.4% triton X 100 for 30 minutes). Caudally, layer 2 is bordered by the cell-body-sparse layer I; medially, layer 3 is bordered by the cell-body-sparse lamina diseccans (layer IV). Layers 2 and 3 are clearly distinguishable throughout the dorsoventral axis of MEC: layer 2 is narrower and has a higher cell body density than layer 3[47]. Both layers end caudally at the border between MEC and the parasubiculum in a structure which has been referred to as a 'large dorsal patch'[33]. This portion of the parasubiculum wraps around the dorsal edge of MEC along both layers 2 and 3, forming an elongated, club-like structure. In Nissl-stained sections, the dorsal border can be identified as a change in cell body size, density and orientation.

To precisely locate the border, slices were also processed with parvalbumin or calbindin antibodies. Both antibodies clearly show the dorsal border of MEC: calbindin staining is intense in MEC layer 2 and absent in the parasubiculum, and parvalbumin staining is intense in the parasubiculum and MEC layer 2 but weaker in layer 3[47]. Washes between antibody incubations were in PBS-TX (2% w/vol milk powder and 0.4 % triton X 100 in 1xPBS). For Parvalbumin, sections were incubated in a monoclonal mouse-anti-parvalbumin 1ary antibody (Sigma P3088, 1:2000 vol/vol in PBS-TX) for

12 hours, then in Alexa Fluor 647 goat anti-mouse IgG 2ary antibody (Invitrogen A-21235, 1:750 vol/vol in PBS-TX) for 3 hours. For calbindin, sections were incubated in polyclonal rabbit-anti-calbindin antibody (Abcam ab11426, 5 μg/mL in PBS-TX) for 12 hours, then in Alexa Fluor 647 goat anti-rabbit IgG 2ary antibody (Invitrogen A-21244, 1:500 in PBS-TX) for 3 hours. All antibody incubation steps were at 27ºC. Tissue shrinkage was not estimated.

To reveal the morphology of filled neurons, we used either DAB (ABC-Elite Vector Laboratories) or a fluorescent avidin detection system. Slices processed with DAB were photographed using a Leica stereomicroscope under brightfield illumination (Leica MZ16FA). For fluorescence processing, slices were first incubated in blocking solution (0.4% triton X 100 containing either 5% acetylated BSA (Invitrogen) or 2% milk powder), for 3 hours at 27ºC. Slices were then incubated overnight in triton X containing 2% milk power and 8 μg/mL Alexa 488-conjugated streptavidin (Invitrogen). All triton X used is 0.4 % in PBS. All PBS used is 1X.

Slices processed with fluorescent avidin were mounted in 50% glycerol in PBS and imaged on a Leica SP5 Confocal microscope with a glycerin immersion 20X objective. Confocal image stacks were visualized with Volocity software (Perkin Elmer). To create a two-dimensional image of cells, stack frames were smoothed by convolution with a 3x3 uniform filter in ImageJ (NIH), followed by a maximum intensity projection; the images were then inverted so that cells appeared black (e.g. Fig. 3e, Supplementary Fig. 13d). Two-dimensional representations of each cell were made by tracing manually over the maximum intensity projection in Adobe Illustrator (e.g. Supplementary Fig. 13e, Supplementary Fig. 14).

Cells were classified as stellate or pyramidal based on morphology. Excitatory cells in layer 3 have pyramidal morphology[52], whereas layer 2 contains both stellate and pyramidal cells[53]. Although pyramidal cells in layer 3 can be further categorized into subtypes[54], they are treated as a single group here. In layer 2, stellate cells can be distinguished from pyramidal cells by the shape of their dendritic tree: stellate cells have multiple apical dendrites of comparable diameter and these spread widely in layer I[55]. In contrast, pyramidal cells in layer 2 have smaller somas, usually only one principal apical dendrite, and more confined dendritic trees[55].

**Whole-cell: reward artifact removal**

To examine subthreshold features of the membrane potential, we first removed artifacts resulting from the opening and closing of the solenoid valve used to deliver rewards. Solenoid artifacts were stereotyped and present only at the reward location, occurring once per run. We calculated the reward-onset triggered median of Vm for portions 1 ms before to 10 ms after reward onset, and the reward-offset triggered median of Vm for 2.5 ms before to 25 ms after reward offset to produce an estimate of the noise waveform resulting from the solenoid; the median was chosen rather than the average to avoid contamination by spikes. The solenoid opening and closing artifacts were subtracted from the membrane potential; any spikes occurring during the reward were unaffected. Reward artifacts were also removed from the 500Hz-10kHz filtered version of Vm, which was used for spike detection. All artifact removals were visually inspected.

**Whole-cell: recording rejection criteria**

All cells whose resting potential was -58 mV or lower were included for analysis, for a total of 53 whole-cell recordings from 38 mice. For subsequent analysis, recordings were truncated if spike amplitude dropped below ~20 mV above baseline, or if the resting potential increased by more than ~8 mV from its value at the onset of the recording, whichever, if any, happened first.

**Whole-cell: spike detection**

Spikes were detected offline using a threshold based on a bandpass filtered version of Vm (500 Hz – 10 kHz). The spike width at ½ maximum amplitude was estimated. Spike widths formed a bimodal distribution: two cells had much narrower spikes then the next widest spike; these two cells were classified as interneurons; the cutoff width used for interneuron classification was 0.45 ms.

**Whole-cell: Cell classification**

The remaining 51 neurons from 36 mice were classified as putative excitatory cells. Of these, 27 cells from 24 mice were classified as grid cells based on the grid definition described above. Based on a combination of cell morphology, electrode position, and electrophysiological signatures assessed during the recording session, we assigned 35/51 principal cells to layer 2 (25 cells) or layer 3 (10 cells). We assigned 19/27 grid cells (from 19 mice) to layer 2 (14 cells) or layer 3 (5 cells). The layer for the remaining 8/27 grid cells could not be unambiguously identified.

Of the 35 cells for which the layer could be assigned, 11 cells (from 8 mice) were classified as large-theta cells and 24 cells (from 23 mice) were classified as small-theta cells. Of the 11 large-theta cells, 10 were in layer 2 of MEC and one was in layer 2 of the Presubiculum, in a structure referred to as a large dorsal patch[33]. 5 of the 6 large-theta cells for which gridness could be assessed were classified as grid cells. We recovered the morphology of 2 of the 5 large-theta grid cells: one pyramidal, one stellate. Of the 24 small-theta cells, 14 were in layer 2; 9 of these 14 were grid cells; the morphology of 7/9 was found: 5 stellate, 2 pyramidal (Fig. 4e). The other 10/24 cells were in layer 3, and 5/10 were grid cells. The morphology of 3/5 was recovered: all pyramidal (Fig. 4e). In layer 3, excitatory cells are expected to have pyramidal morphology[52].

### Whole-cell: extracting ramps and theta

To analyze subthreshold features of the membrane potential, spikes were removed and replaced by linear interpolation using a 3 ms before and 6 ms after window. The resulting Vm, after reward artifact and spike removal, is referred to as the ‘spike-free Vm’. Because models of grid formation make differing predictions about theta-frequency and slow-changing components of the membrane potential (theta and ramps), the spike-free Vm was decomposed into a ramp component and a theta component (Supplementary Fig. 15).

To calculate ramps, the spike-free membrane potential was filtered with a 0-3 Hz lowpass FIR filter. When the ramp filter was applied to a simple interference pattern (e.g. the sum of an 8Hz and 9Hz sinusoid as in Fig. 1a), the output was constant during the entire period. The average value of this filtered quantity during all out-of-field periods of a cell was calculated and subtracted to produce the ramp signal (Supplementary Fig. 15d).

To calculate theta, the spike-free membrane potential was filtered using a 5-11 Hz bandpass FIR filter. To ensure that the ramp and theta components captured distinct aspects of the spike-free Vm, the theta and ramp filters were chosen to have nearly 60 dB attenuation at their intersection point (Supplementary Fig. 15b). We used a Hilbert transform to calculate the time-varying peak-to-peak envelope of theta oscillations, which provided an ongoing estimate of the theta amplitude (Figs. 3,4,5,Supplementary Fig. 15).

## Defining large theta cells (illustrated in Supplementary Fig. 16)

Based on our recordings, we observed that a subset of cells had very large theta oscillations. When we calculated the power spectrum of the spike-free membrane potential, we found that these recordings had narrow power spectra centered on theta, and much less relative power at adjacent frequencies (e.g. 14-22 Hz). In contrast, small-theta cells had lower amplitude oscillations and a wider distribution of power at frequencies around the theta range. Power spectral estimates were from the entire recording for each cell, including moving and stationary periods.

We calculated the mean theta envelope for moving-only portions of the recording, as well as the ratio between peak theta power and the peak power in the 14-22 Hz band for the entire recording. When we plotted the theta/14-22 Hz ratio vs. mean theta amplitude for all cells, we observed two well separated cell clusters (Supplementary Fig. 16a); we used k-means on the z-scores of the theta/14-22 Hz ratio and mean theta envelope with two clusters to confirm the presence of two distinct populations of cells (Supplementary Fig. 16b). The clusters chosen by k-means corresponded with manual classification of large and small-theta cells. In this dataset, all large-theta cells had a mean peak-to-peak theta of 5 mV or higher, and all small-theta cells had a mean peak-to-peak theta of 5 mV or lower; in addition to being discriminable by mean peak-to-peak theta alone, in this dataset, all large-theta cells had a peak theta power / peak 14-22 Hz power ratio of 8 or higher, whereas all small-theta cells had a ratio of < 8. Nevertheless, the combination of a narrow peak at theta with respect to adjacent frequencies and large amplitude oscillations together best define the difference between large and small-theta cells.

## Electrophysiological properties

For grid cells, the mean out-of-field membrane potential (after spike removal) was -71 ± 3 mV for large theta cells, -73 ± 6 mV for layer 2 small theta cells and -68 ± 2 mV for layer 3 cells (means not significantly different, one-way ANOVA, $F(2,16) = 1.66$, $p > 0.2$). When considered across all cells (grid, non-grid and unassigned), the median input resistance was 77 MΩ for large theta cells and 32 MΩ for layer 2 small theta cells. The distributions of input resistances for large and small theta cells had significantly different medians (large theta, $n = 8$; layer 2 small theta, $n = 10$; Mann-Whitney U test, $p < 0.05$). The median input resistance for layer 3 cells was 112 MΩ. A higher input resistance in layer 3 vs. layer 2 has been observed in slices[52,53].

## Relationship between ramp, theta envelope, and firing rate peaks

To determine whether ramp and firing rate peaks coincided or whether the ramp peaked before the firing rate with respect to position, for every firing field, we found the peak of the ramp within the field's spatial extent and the peak of the firing rate and calculated the spatial lag between the two. The mean spatial lag was significantly different from zero (mean lag = -1.4 ± 6.7 cm, n = 27 grid cells, $t(94) = 2.0$, $p < 0.05$, *t*-test; the small but negative value again indicates that the firing rate peak occurred slightly before the ramp peak with respect to space). To confirm that the firing rate peaked slightly earlier than the ramp peak with respect to time as well as position, the time-varying firing rate was estimated by convolving the spike train with a Gaussian kernel with a standard deviation of 0.5 seconds. Considering moving periods only, we calculated the temporal cross correlation between the ramp and the time-varying firing rate (both downsampled to 1kHz), using a maximum lag of 150 ms. Longer lags (verified up to 2s) do not change the results. The mean temporal lag was significantly different from zero (mean lag = -32.3 ± 33.3 ms, $t(26) = 5.0$, $p < 10^{-4}$, *t*-test; the negative value indicates that the firing rate peaked slightly earlier in time than the ramp).

The analysis for theta envelope was performed as for ramp peaks. The mean spatial lag of the peak of the cross correlation between the firing rate and theta envelope vs. position functions did not differ significantly from zero (mean lag = 0.53 ± 8.77 cm, $t(94) = 0.6$, $p > 0.5$, *t*-test). The mean temporal lag for the peak of the cross correlation between the time-varying firing rate and theta envelope also did not differ significantly from zero (mean lag = 7.0 ± 72.5 ms, $t(26) = 0.50$, $p > 0.6$, *t*-test).

To calculate an overall average ramp, firing rate and theta envelope across cells, each field was rescaled spatially to begin at 0 and end at 1. The average ramp, firing rate and theta envelope were then calculated with respect to position along a field traversal. The peak of each was identified with respect to progression within each field (Supplementary Fig. 25).

### Highly stable firing fields

A firing field was defined as highly stable if the median Pearson's correlation between the firing rate on all pairs of individual runs through the field was above the 50th percentile of this value across all firing fields from all cells and if it had spikes on 1/3 or more of the runs.

### Grid cells with a high degree of periodicity in 1D

The firing rate along the linear track was calculated as described previously, then smoothed using a 5-bin (25 cm) moving average; we then subtracted the mean of the firing rate and calculated the firing rate autocorrelation, smoothed the autocorrelation with a 5-bin (25 cm) moving average, normalized it so the largest value was 1, and found the peaks of the autocorrelation. We then calculated the discrete time Fourier transform (Matlab function fft) of the autocorrelation and found the spatial frequency with the largest power in the resulting one-sided power spectrum; the length of the autocorrelation was 161 5-cm spatial bins; the length of the FFT was set to 256. The one-sided power spectrum was defined as two times the squared magnitude of the FFT at each frequency.

Qualitatively, a cell was considered to have highly regular (or highly periodic) firing patterns in 1D if the fields were approximately equally spaced, the firing rate had a dominant spatial frequency and the peak firing rates in each field were similar. Quantitatively, a cell was considered to have highly regular firing patterns if: a) the autocorrelation had at least three peaks at positive lags in addition to the peak at zero and the largest distance between subsequent peaks was less than 25% different from the mean distance between peaks. b) The ratio between the mean power within 0.12 fields/m spatial frequencies around the peak (defined as the spatial frequency with the highest power) in the power spectrum was at least 50 times larger than the mean power in the 0 to 10 fields/m spatial frequency range excluding the peak. c) The largest difference in peak firing rate between any two fields of the cell was <= 8Hz. Using these criteria, 7/27 grid cells had highly regular firing patterns in 1D.

### Non-grid cells

To determine whether non-grid cells exhibited ramps and theta oscillations, we first defined non-grid cells as those with properties opposite to highly regular firing fields (defined above). The autocorrelation of the firing rate was defined as for highly regular grid cells. Non-grid cells were defined as those neurons that a) did not meet the criteria for being a grid cell and b) their firing rate autocorrelation had either only one peak at positive lags, or two peaks such that the smallest distance between subsequent peaks was larger than 25% of the mean distance between peaks. Using these criteria, 7/13 cells that did not fulfill the criteria for grid cells were classified as non-grid cells (all their firing rates are shown in Supplementary Fig. 26). The remaining 6 cells were unclassified.

### Average in-field and out-of-field ramp and theta amplitude

To compare ramps and theta amplitude during in-field and out-of-field periods for each cell (e.g. Fig. 4e,f), we calculated the average ramp and theta envelope during all time points when the mouse position was inside a field or an out-of-field period respectively. All time points were considered to be equivalent such that, for example, a wider field would contribute more data points to the average if the mouse ran at a constant speed. Only running periods were included.

### Spatial information

To determine whether ramps or theta oscillations contained more information about position along the virtual linear track, we calculated the mutual information between ramps and position [MI (ramp, position)] or theta envelope and position [MI (theta envelope, position)] respectively. As shown schematically in Supplementary Fig. 20, two-dimensional bins were defined by discretizing along both the voltage and position axis (40 bins span between the maximum and minimum voltages for each set of waveforms, and 100 bins span the position axis).

To calculate the mutual information between position (X) and ramp (R), the total counts in each bin were determined for every $r \in R, x \in X$, which defined the estimated probabilities p(r,x). Estimates of p(r) and p(x) were then calculated by appropriate sums along the vertical columns and horizontal rows. We then calculated the mutual information between position and ramps as :

$$I(X;R) = \sum_{\substack{all \\ r_i \subset R}} \sum_{\substack{all \\ x_j \subset X}} p(x_j, r_i) \cdot \log_2 \left( \frac{p(x_j, r_i)}{p(x_j) p(r_i)} \right)$$

where $p(x_j, r_i)$ is the probability of being in position bin j and ramp bin i, $p(x_j)$ is the probability of being in position bin j, and $p(r_i)$ is the probability of being in ramp bin i. To calculate the mutual information between theta envelope waveforms and ramps, we followed an analogous procedure. The mutual information calculations were performed using the 'entropy' package in the R programming environment.

Sampling bias is produced from the use of counts per bin as estimates of the probabilities instead of the actual probabilities. The uncorrected estimates of mutual information were calculated using the ‘mi.plugin’ routine in the entropy package (units = log2). Bias corrected estimates were calculated using the ‘mi.shrink’ routine. Calculations were performed with two other statistical strategies for bias estimation using the ‘mi.Dirichlet’ routines, with no qualitative change in the results. In all cases, the mean ratios, for the 27 cells analyzed, of MI (ramp, position) / MI (theta envelope, position) were always greater than 2.0.

**Spike phase with respect to intracellular or extracellular theta**

To assign a phase (0-360º) to each spike, we found, for a spike occurring at time t, the peaks of theta immediately before and after the spike ($t_1$ and $t_2$). The spike phase was then defined as 360*(t- $t_1$)/($t_2$ – $t_1$). 0º and 360º both correspond to the peak of the oscillation (Fig. 6f). The distance $d$ between any two phases $\varphi_1, \varphi_2$ (measured in degrees) was defined on the unit circle:

$$d = \min\left(mod(\varphi_1 - \varphi_2, 360^{o}), mod(\varphi_2 - \varphi_1, 360^{o})\right).$$

The distance between two phases is therefore always between 0º and 360º. The mean of a group of phases was defined as the phase (in degrees) that minimized the sum of the squared distances to all the phases in the group.

**Extracellular recordings**

To determine whether the phase of spiking precesses with respect to extracellular (LFP) theta oscillations, we performed single-unit extracellular recordings targeted to Layer 2 of MEC. Targeting was performed as described for whole-cell recordings. Electrodes were similar to those used for whole-cell recordings, pulled to a narrower tip size and filled with 0.2 – 1M NaCl. Single units were isolated using standard procedures. Training, craniotomies, and the virtual environment were identical for mice used for extracellular and intracellular recordings. Spikes were sorted using a threshold-based analysis. Spike waveforms were visually inspected to ensure good isolation. All recordings were checked to ensure the absence of ISI violations (any two spikes occurring closer than 1 ms).

We recorded 17 single-units from 3 mice in layer 2. The same classifier applied to whole-cell recordings identified 8/17 recordings as grid cells.

### Phase precession analysis

Dataset: for phase precession analyses, we used 27 whole-cell recordings from grid cells and 8 extracellular recordings from grid cells (from 3 mice). Field definition: for phase precession analyses, we used a modified method of identifying field boundaries because the in-field out-of-field definition used in all other analyses leaves spikes at the boundaries of the fields (where the firing rates are low) unassigned to either in-field or out-of-field periods. For phase precession we therefore calculated the $P_{value}$ as described previously, smoothed it with a 3-point Gaussian kernel with a standard deviation of one, then identified candidate fields as described previously. Candidate fields were extended in both directions until a bin was reached for which the $1-P_{value}$ was less then 0.05 or for which the $1-P_{value}$ was greater than the preceding bin (corresponding to an increase in firing rate). As before, firing fields were defined as candidate fields with spikes on at least 20% of all runs. Out-of-field periods were not defined for phase precession analyses. Only spikes fired while the mouse ran at a speed >= 10 cm/s were included. The same procedures were applied for intracellular and extracellular recordings. Only fields with 50 or more spikes were included in the analysis.

To examine whether the phase of spikes precessed with respect to intracellular theta oscillations, we circularly shifted the phase of spikes in 1° steps from 0° to 360°, continuing across the 360° border, and fit a linear regression line to the phase versus position plot at each rotation. We found the rotation with the best fit, such that the sum of squared errors between the fit line and data was minimized, and used the Pearson's correlation coefficient between phase and position and the slope of the line of best fit at this rotation as measures of phase precession. As a separate measure of phase precession, for each field we found the mean phase in the first eighth and in the last eighth of the field (defined in terms of the position of the first and last spike in the field rather than by bin boundaries). Mean phases were calculated using the same optimal rotation found for the line of best fit. To report mean phases, we then subtracted the value of the optimal rotation to maintain the correct numerical phase for spikes (such that if all spikes occurred on the trough of an oscillation, the mean phase would be 180°).

### Normalized theta and ramp amplitudes

Each cell had a range of ramp amplitudes (from 0 to maximum) and a range of theta envelope amplitudes (from 0 to maximum). To compare when spiking begins with respect to the range of ramp and theta envelope of each cell, we normalized both the ramp and theta envelope ranges to 0-1 separately for each cell (e.g. Fig. 6c,d). To normalize the ramp and theta envelope, we first removed data points where ramps or theta were outside the 0.1th to 99.9th percentile for that cell. Ramp or theta values lower than the 0.1th or higher than the 99.9th percentile were considered outliers. The remaining range was scaled linearly so that both ramp and theta envelope spanned 0 – 1. As a result, a theta envelope value corresponding to the 99.9th percentile would be mapped to 1 and a theta envelope value corresponding to the 0.1th percentile would be mapped to 0. For successive 1 ms time intervals during a recording, we sampled the value of the normalized ramp and theta envelope at the start of the 1 ms period. In normalized ramp and theta envelope axes, if the cell spiked during the 1 ms period, we plotted the associated normalized ramp and theta envelope as a black dot (Fig. 6c) or as a small grey dot if the cell did not spike (Fig. 6c). To calculate the firing rate at each combination of normalized ramp and theta amplitude, the 0-1 range for both axes was binned in 25 equal-size bins; the firing rate at each normalized ramp-theta envelope combination was calculated as the number of spikes in that bin divided by the number of seconds spent in that bin (#spike-associated points per bin)/(#all points per bin×.001s). Firing rates could then be averaged across cells.

### Spike onset

To determine whether spiking was present throughout the entire range of the ramp or only when the ramp was high, we defined the onset of spiking as the 1st percentile of the distribution of ramp values at the time points when the cell spiked (so that 99% of spikes occurred at a higher ramp). We then expressed this onset of spiking as a percentile of the distribution of ramp values during the whole recording. For example, if the cell spiked only when the ramp was above-average, then the smallest ramp with a spike would correspond to the ~50th percentile of the entire ramp range. We defined the onset of spiking with respect to the theta range in the same way.

### Velocity-frequency analysis

To estimate the frequency of membrane potential oscillations, the spike-free membrane potential was downsampled to 500 Hz. We then calculated a windowed Fourier transform of this function (using a short time Fourier transform tf_fsel function in Matlab with a 1 second-long Gaussian window) that estimated the power at a range of frequencies within the theta band (0.1 Hz frequency resolution). To obtain a single estimate of the frequency of theta at each point in time, we used the center of mass frequency obtained from the power vs. frequency function at that point. Using the peak frequency gave qualitatively similar results. To analyze the frequency of theta oscillations as they related to running speed, only running speeds higher than 10 cm/s were used. Periods where running speed was above 10 cm/s were binned into nonoverlapping 5 cm/s bins. Speed bins where the mouse spent less than 5 seconds were not included. We then calculated the mean and standard deviation of the frequency in each bin (Supplementary Fig. 27).

## Theta index

To calculate the theta index (e.g. as used in Supplementary Fig. 24), we first computed the spike-train autocorrelation for each cell using a 10 ms bin size. Autocorrelograms were truncated at 500 ms. The peak at zero lag was set to equal the next largest data point not including the peak; the mean was then subtracted. We next calculated the FFT of the autocorrelogram (using length $2^{16}$), obtained the one-sided power spectrum and smoothed it with a moving average 2Hz window. The theta index was defined as the ratio of the mean power within 1 Hz of the peak in the theta (5-11Hz) range to the mean power between 0 and 50 Hz (excluding the theta peak and the +/- 1Hz region around it). This theta index is very similar to ones used previously[46].

## Models of grid formation

Interference model schematic (Fig. 1a, Supplementary Fig. 1a): to produce the predicted membrane potential for runs through grid fields in the basic interference model, we used the sum of an 8Hz and a 9Hz sinusoidal oscillation, sampled at 20 kHz. This is equivalent to a 1-dimensional interference model simulated with constant running speed (e.g. Fig. 1 from Burgess et al. 2007)[7]. This predicted membrane potential was filtered with the same ramp filter used for extracting ramps – in this case the result is that there is no ramp (hence the flat red line in Fig. 1a).

Attractor network model schematic (Fig. 1b, Supplementary Fig. 1b): to estimate the predicted membrane potential during runs through grid fields, we implemented a version of the attractor network model as described by Burak and Fiete 2009[16]. We used the Poisson spiking form of the model rather than the firing-rate form because the spiking model produces a predicted value that can be interpreted as the membrane potential. Here, we do not describe the model in detail, but provide the precise parameters used in the simulation. We used a 64 x 64 neuron sheet with toroidal (periodic) connectivity. The parameters used for Fig. 1 were the default specified by Burak and Fiete 2009 (For Poisson spiking: CV = 1; for integration: $\Delta t = 0.5$ ms, $\tau = 10$ ms; for shift of connectivity by N, S, E, W - selective cells: L = 2; to couple the speed of the animal to movement along the neural sheet, $\alpha = 0.102315$; to specify the connectivity matrix as a function of distance between a cell and its neighbors, a = 1, which means all connectivity is inhibitory, $\lambda_{net} = 13$, $\beta = 3 / \lambda^2_{net}$, $\gamma = 1.05 \times \beta$). The network was initialized with a random 'synaptic activity' $s_i$ drawn independently for each cell from a uniform 0-1 distribution. The network received a constant velocity input of 0.8 meters/second in the 60º NE direction from the outset of the simulation. For this form of the model, we defined its prediction of the membrane potential of cell i at time t as $\hat{U}m_i(t) = W_{ij} \times s_j(t) + B_i(t)$, which is equivalent to the sum of the synaptic weights ($W_{ij}$) times the synaptic input at time t, $s_j(t)$, from all presynaptic partners, plus the external input $B_i(t)$ which encapsulates the velocity drive. Because in this model the synaptic input $s_j(t)$ from each cell j increases when that cell spikes, then decays with time, the synaptic input contains dynamics that mimic EPSP decay. To illustrate the predicted membrane potential from this model, we plotted the membrane potential of three cells during two field traversals (Supplementary Fig. 1b, cells A,B and C). To create a schematic of this prediction without high frequency noise, we used Gaussian kernels to illustrate the slow depolarization underlying every field (see Supplementary Fig. 1b, Fig. 1).

Attractor with injected-theta model schematic (Fig. 1c, Supplementary Fig. 1c): because this model makes explicit predictions about the membrane potential of a grid cell during runs through grid fields, which are shown in Fig. 3F of Navratilova et al. 2011[17], we created a schematic trajectory (see Supplementary Fig. 1c) that replicated the primary features of the ramp and theta oscillations illustrated in this model. This schematic trajectory could then be used to extract the ramp and theta components (Fig. 1c).

## Supplementary References

51. Quilichini, P., Sirota, A. & Buzsaki, G. Intrinsic circuit organization and theta-gamma oscillation dynamics in the entorhinal cortex of the rat. *J Neurosci* **30**, 11128-11142 (2010).
52. Dickson, C. T., Mena, A. R. & Alonso, A. Electroresponsiveness of medial entorhinal cortex layer III neurons in vitro. *Neuroscience* **81**, 937-950 (1997).
53. Alonso, A. & Klink, R. Differential electroresponsiveness of stellate and pyramidal-like cells of medial entorhinal cortex layer II. *J Neurophysiol* **70**, 128-143 (1993).
54. Gloveli, T., Schmitz, D., Empson, R. M., Dugladze, T. & Heinemann, U. Morphological and electrophysiological characterization of layer III cells of the medial entorhinal cortex of the rat. *Neuroscience* **77**, 629-648 (1997).
55. Klink, R. & Alonso, A. Morphological characteristics of layer II projection neurons in the rat medial entorhinal cortex. *Hippocampus* **7**, 571-583 (1997).